UNIVERSITÀ DEGLI STUDI DI CAMERINO

School of Advanced Studies

DOCTORAL COURSE IN

CHEMICAL AND PHARMACEUTICAL SCIENCES AND BIOTECHNOLOGY

XXXVI cycle

INVESTIGATION OF DIFFERENT MATERIALS WITH APPLICATION AS REINFORCES OF COMPOSITES, AS VOCs SENSORS, AND AS ANTITUMOR AGENTS

PhD Student
Pietracci Lorenzo

Supervisor
Marchetti Fabio

Summary

Introduction to doctoral thesis work

My doctoral work developed along three directions with different objectives relating to three different research areas:

(1) the first part of this doctoral thesis is related to the work carried out in collaboration with the HP Composites company of Ascoli Piceno, Marche, Italy, and concerns studies aimed at developing a method to customize the alkaline treatment of flax and hemp fibers for use in the production of composite epoxy resins for automotive applications.

(2) the second part of the doctoral thesis concerns the design, synthesis and characterization of new ruthenium(II) organometallic complexes with pyrazolone and acylpyrazolone ligands containing a pyridine ring and the study of their cytotoxicity against human ovarian cancer (A2780 and Cisplatin - A2780cis resistant) and non-tumor human embryonic kidney cell lines (HEK293T).

(3) finally, the third part of the thesis reports the synthesis and characterization of some silver(I) coordination polymers with ditopic bipyrazole ligands and the study of their potential use as chemosensors for the detection of volatile organic compounds (VOCs) released by fruits climacteric after harvest.

Natural Fibers in Composite Materials

Introduction

In recent years, research in the field of composite materials has been increasingly involved in the design and synthesis of new materials from renewable resources, capable of being included in a circular economy model (Figure 1). [1]

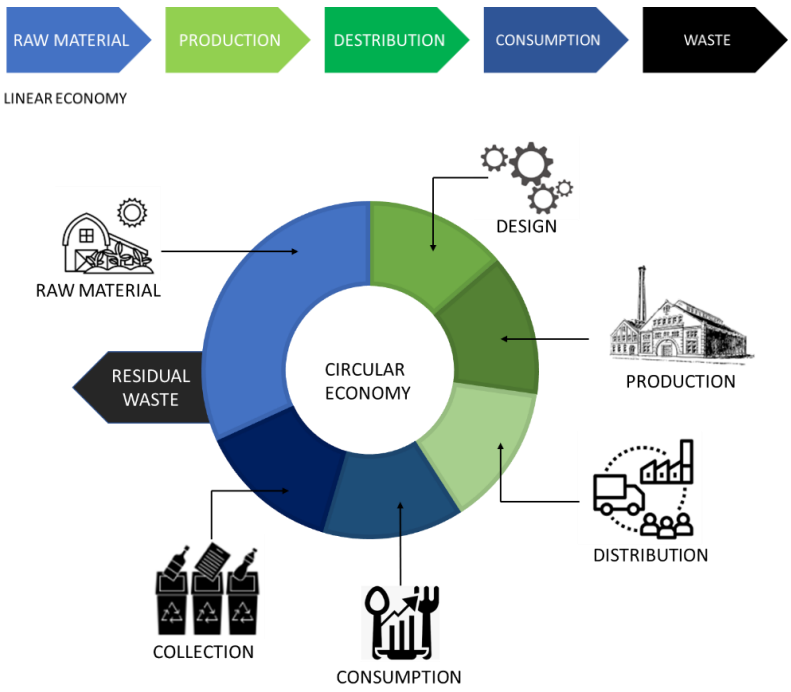

Figure 1. Circular Economy model representation.

Among the most investigated renewable resources are natural fibres of vegetable origin, which have excellent specific properties, thanks to their low density (1,2-1,6 g/cm^3), and their interesting physical, chemical and mechanical properties. Natural fibres are excellent candidates for replacing materials such as glass and carbon fibres, used in various sectors such as

construction, nautical, aeronautics, automotive and other industrial production, which have synthetic origins and they are not recyclable.[2,3]

In particular, carbon fibres are obtained from petroleum derivatives, as for example polyacrylonitrile (PAN), which is submitted to several chemical and physical processes to obtain the final fiber.[4,5]

These industrial processes are very expensive and have a huge impact on the environment and people's health. The final objective is therefore to use materials that have the lowest possible environmental impact, which are not dangerous to health and which have a low cost. Also in this regard, fibres of natural origin have proven to be the most suitable solution to satisfy these needs, thanks to their availability and abundance in nature, ease of availability, origin from renewable sources, economical production processes and so on.[6]

However, plant fibers present numerous limitations that influence the mechanical properties of the final polymer matrix composites. These problems can be identified as follows: high hygroscopicity, low compatibility with the polymeric resins used as matrices, high heterogeneity in size, chemical composition and intrinsic mechanical characteristics.[2,7]

In order to solve these problems, treatments capable of improving these aspects are necessary so as to obtain better composites capable of competing with synthetic materials.[8,9]

Even choosing the type of fibre to use is not a simple task, as each type of fibre has different characteristics at a biochemical and structural level. Even fibres that derive from the same plant can present substantial differences, since their characteristics depend on countless factors, which are difficult to keep under control. Among the main ones are the type of soil in which the plant is grown, and therefore the quality and quantity of nutrients that the plant absorbs during its growth; the geographical area, and therefore the climate, the quantity of sun and water that the plant has received; the harvest period and therefore the state of maturation of the plant; finally, the processing techniques to obtain the fibre and fabrics.[10,11]

All these factors strongly influence the biochemical composition and structural characteristics of the plant fibre, which is made up of three main

components, cellulose, hemicellulose and lignin, but also of minor components such as tannins, pectins and waxes.[12,13]

The relative quantity of all these components and their chemical and structural nature strongly influence the mechanical (e.g. elastic modulus, tensile strength, etc.), physical (e.g. thermal stability) and chemical (resistance to chemical substances and biological agents) characteristics which can degrade the material) of the fibers and influence the compatibility with the polymeric matrices listed above.[8,14,15]

Biochemical composition of vegetable fibres

Now we will deal in more detail with lignocellulosic fibers or simply cellulosic fibers. They are lighter fibers (and therefore with better specific mechanical properties that depend on the density of the material), cheaper and easier to find than materials such as glass and carbon.[6,16] As previously mentioned, the main components of ligno-cellulosic fibers are cellulose, hemicellulose and lignin. Cellulose is the component that structurally supports the cell wall of plant cells, and it is the one that gives the fibre its mechanical properties.[17,18]

The linear cellulose chains interact with each other by establishing hydrogen bonds and Van Der Waals interactions, giving a certain degree of crystallinity to the polysaccharide (Figure 2).[19]

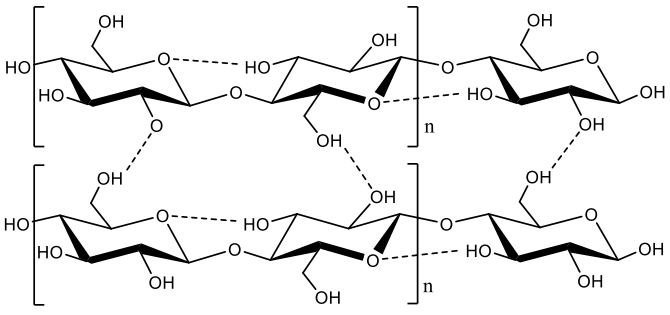

Figure 2. Cellulose structure with the representation of intra- and inter-molecular hydrogen bonds.

Hemicellulose (Figure 3) is an amorphous heteropolymer composed mainly by five monosaccharides: D-mannose, D-galactose, D-glucose, L-

arabinose and D-xylose which is the most abundant. Other sugars, such as L-Rhamnose and α-L-Fucose, can be present in minor amounts, and some of the OH groups in the monomers can be acetylated.[12,13,21]

Since it is a branched, short-chain and amorphous polymer, it has numerous free -OH groups. They are not involved in intra- and interchain interactions as much as in the case of cellulose, and therefore are available to establish hydrogen bonds with water or air moisture, making hemicellulose the most hygroscopic component. Again, thanks to its chemical and structural nature, it is the most bio-susceptible component, as it is easier for microorganisms to attack and depolymerize the ends of the polymer branches. Finally, it is also the most thermodegradable component, given that it is easier to break the acetal bonds that hold the monosaccharides together.[20]

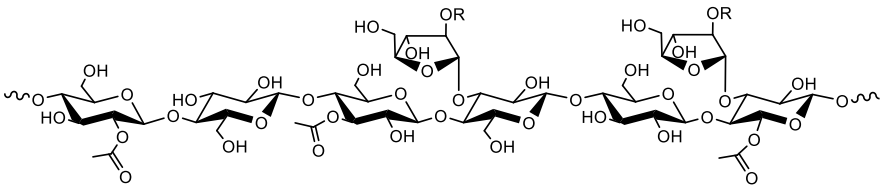

Figure 3. Hemicellulose structure.

The last component, lignin, is a branched amorphous heteropolymer composed of methoxylated phenylpropanoid units. It has a much lower oxygen content (*ca.* 30% wt) than the other two polysaccharides, cellulose and hemicellulose (*ca.* 49% wt).[13] It is more hydrophobic than carbohydrates, and with a good thermal resistance (the temperature of degradation is around 900°C) but it is sensitive to ultraviolet rays. It is an amorphous macromolecule consisting of three main monomers: p-coumaryl alcohol (a), coniferyl alcohol (b) and sinapyl alcohol (c).[21,22]

Condensed together through ether linkages they give the macromolecule lignin, which is composed of the repeating units phenylpropanoids guaiacyl (G), syringyl (S) and hydroxyphenyl (H) (Figure 4).[23]

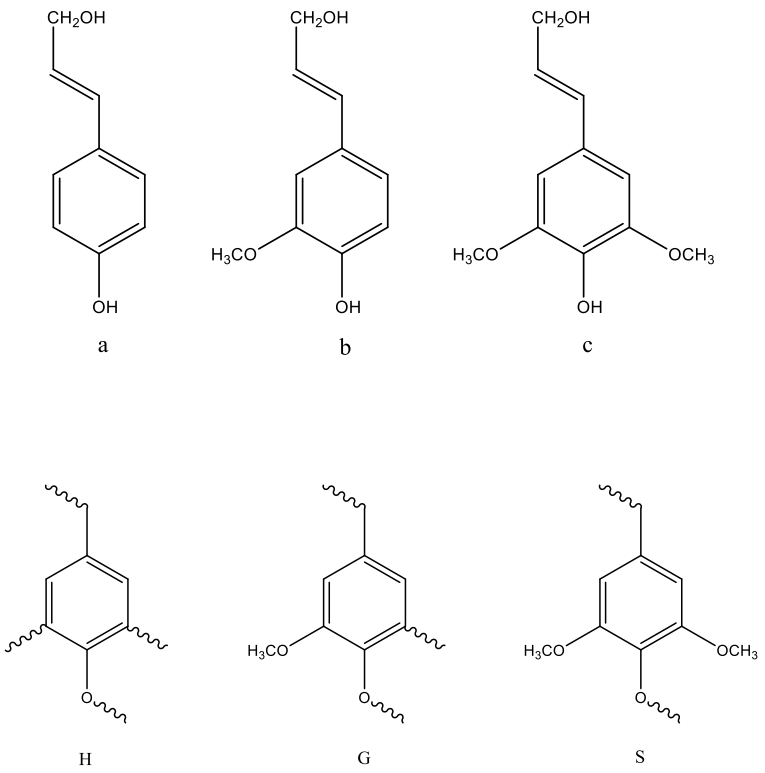

Figure 4. Monomers (a, b and c) and repeating units (H, G and S) of lignin.

The percentages of individual monomers depend on the type of plant and on all the above-mentioned parameters. Lignin surrounds the hemicellulose and cellulose in the plant cell wall, while the cellulose chains are intertwined with the hemicellulose. Lignin is the component that provides greater protection against microbial attacks.[13]

We can therefore consider that cellulose acts as a strengthener of the cell wall, while the amorphous components such as lignin and hemicellulose act as a matrix, thus forming a natural composite material.

Structural characteristics of ligno-cellulosic fibres

Vegetable cells are interconnected with each other through cell walls, which are made up of a dense network of macrofibrils, which are constituted of numerous microfibrils, which in turn are composed of cellulose chains and others constituents above mentioned. A representation in Figure 5.

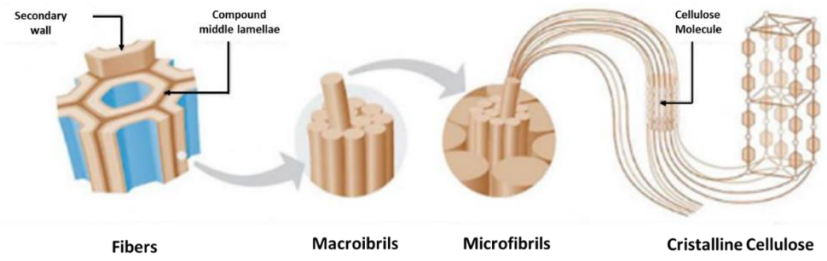

Figure 5. Representation of natural fibres structural units. (Kaith B. S., 2011)[24]

The composition of the cell wall, starting from the outermost part, is based on (Figure 6):

- *Primary cell wall*: it has a structural role, composed of cellulose with low crystallinity and amorphous parts such as hemicellulose and lignin.
- *Secondary cell wall*: it is the most abundant component, and is divided into 3 sections called S1, S2, S3.

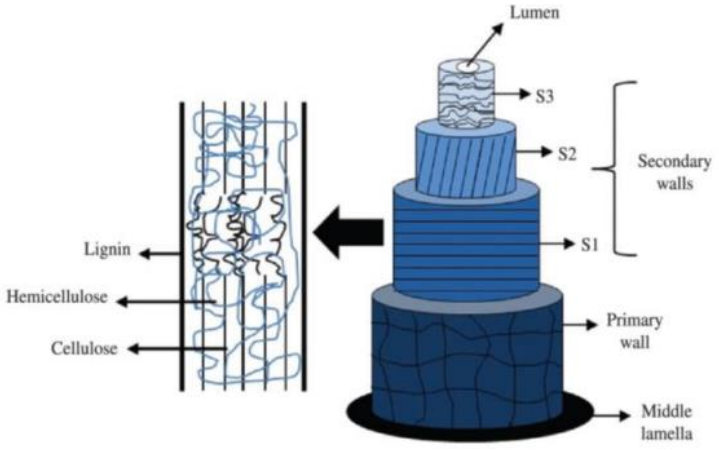

Figure 6. Cell wall structure of vegetable fibres (Benini K. C. C. C. et al., 2015)[25]

In particular, section S2, which constitutes about 80% of the entire wall, is composed of bundles of cellulose with a high degree of crystallinity (depending on the plant species and so on) which develop in parallel helices at a certain inclination, determined by the so-called Micro-Fibrillary Angle (MFA).[26] The MFA is defined as the angle of inclination of cellulose coils with respect to the axis passing through the center of the polygonal section of the cell wall. That of section S2 has an important influence on the mechanical behavior of vegetable fibers. The MFA of flax and hemp fibers, which have high mechanical properties, ranges from 8°

to 11°, while for example sisal, a natural fiber obtained from the leaves of the *Agave Sisalana* from the Yucatan peninsula in Mexico, with a higher MFA (about 20°), shows modest mechanical properties. In addition to the MFA, the percentage of cellulose and its degree of crystallinity are fundamental parameters that must find the right synergy to have excellent physical and mechanical performances. However, we can generally say that the higher the percentage of cellulose, the higher its degree of crystallinity and the lower the MFA, the better the mechanical characteristics.[27] In Figure 7 there is a representation of MFA.

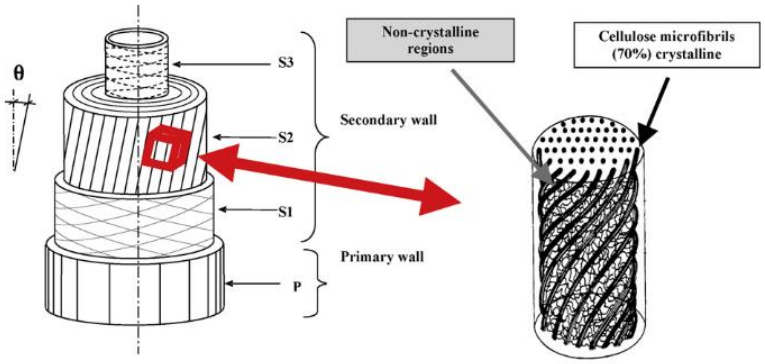

Figure 7. Representation of MFA in relation to the cell wall structure. (Alain B. at all.)[27]

Cellulose

Here the cellulose component will be described in more detail, since it is the main responsible of mechanical characteristics of the vegetable fibre.
Cellulose is a linear macromolecule of the β-anomer of D-glucopyranose linked together by β-1,4-glycosidic linkages (Figure 8). The repeating unit of cellulose is cellobiose, a disaccharide formed by the union of two molecules of β-D-glucopyranose, through β-1,4-glycosidic bonds. The OH groups of cellulose are involved in numerous hydrogen bonds both intra- and intermolecular, which confer a certain degree of crystallinity to the polymer.[28]

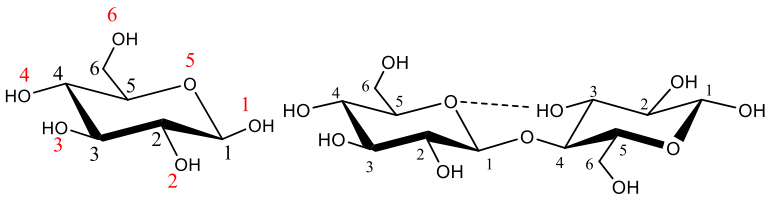

Figure 8. D-glucopyranose (a) and cellobiose (b) structure.

The OH groups of cellulose are involved in numerous hydrogen bonds, both intra- and intermolecular, which confer a certain degree of crystallinity to the polymer. There are different alloforms of cellulose: cellulose I, cellulose II, cellulose III and cellulose IV.[28–30]

Cellulose I is of natural origin and is therefore the most abundant form. The crystalline structure of cellulose I is distributed in two distinct forms: the I_α form (triclinic) and the I_β (monoclinic).[31]

The relative amounts of the two forms depend mainly on the plant species, but in most cases I_β cellulose is the more abundant. Also, for the other forms of cellulose there are different classifications, depending on the type of cellulose to which the treatment is applied: it is possible to obtain cellulose II by treating cellulose I (both α and β) with NaOH, followed by a bath in distilled water. Cellulose III can be obtained by treatment with ammonia both from cellulose I (both α and β), obtaining cellulose III_I, and always by treating cellulose II with ammonia, thus obtaining cellulose III_{II}. By supplying energy in the form of heat to the two forms of cellulose III, cellulose IV_I and cellulose IV_{II} are obtained, respectively (Figure 9).

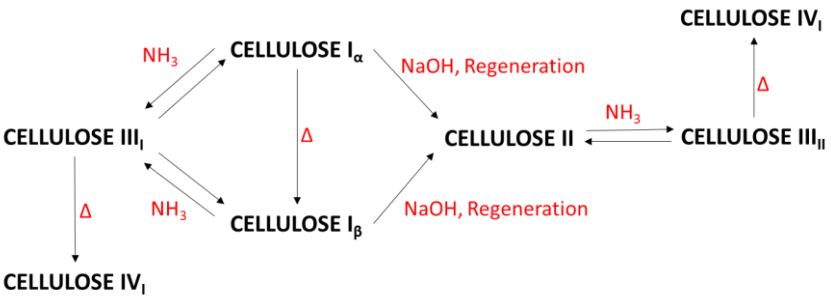

Figure 9. Alloforms of cellulose obtained from two natural forms with different treatments.

Cellulose crystallite sizes are relatively small, approximately 5 nm in width. Depending on the species of plant and other factors, there is a more or less widespread amorphous region of the cellulose.[18]

The hygroscopicity of natural fibers is characterized by the level of "accessibility" of the cellulose, which depends on its degree of crystallinity, but also on other factors such as the presence of hemicellulose and lignin and their % ratio, the porosity of the fiber and the size of the crystallites.[28]

Type I natural cellulose is the structural component of microfibrils, i.e. bundles of chains of cellulose, hemicellulose, lignin, pectins, tannins and waxes which form the cell wall of plant cells. These microfibrils are arranged in an antiparallel manner to each other, and the cellulose I chains composing them are instead arranged in a parallel manner. From the point of view of mechanical performance, cellulose II is the one of greatest interest, as it presents a greater molecular organization and better inter- and intrachain interactions, due to a spatial rearrangement which brings the chains to an antiparallel arrangement with respect to the other, accumulating alternately the OH groups present on the polysaccharide.[32]

Cellulose II usually exhibits a lower chain modulus. This is due to two different conformations of the hydroxymethyl group causing variations in the intermolecular hydrogen bonding,[33] as shown in Figure 9, taken from the study by Northolt et al.[17] in which the structural difference between cellulose I and cellulose II is represented. In Figure 9 (a) it is possible to observe the different conformation of $-C^6H_2-O^6-H$ between cellulose I and cellulose II, and so the different number of intramolecular hydrogen bonds. In fact, cellulose II forms more hydrogen bonds than cellulose I. In Figure 10 a and b a representation of XRD structure of cellulose I and cellulose II.

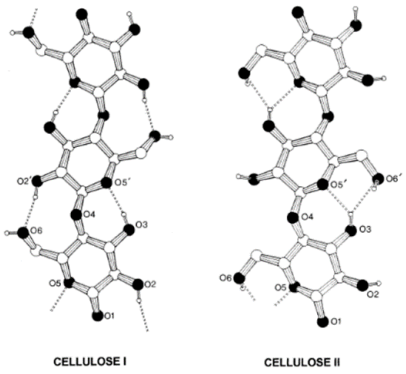

a

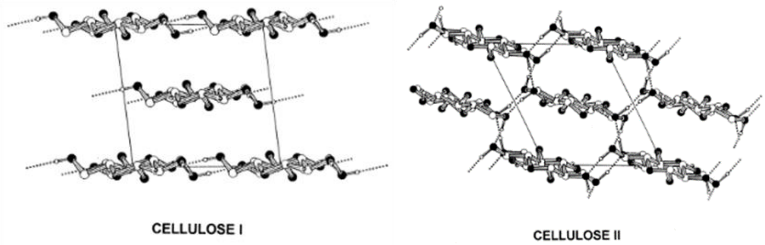

b

Figure 10. XRD structure of cellulose I and cellulose II: (a) representation of different cellulose alloform conformations and different intramolecular hydrogen-bonds; (b) intermolecular disposition along the chain axes, showing the intermolecular hydrogen bonds. Notrholt M, (2001).[17]

The interface in composite materials

In order to obtain a composite fiber/polymer matrix material with suitable physical and mechanical properties, it is of fundamental importance that the so-called "interface" is formed between the two materials (Figure 11).[2,34]

It is the key to obtaining the right synergy between the two components of the composite, with even higher performance than the simple sum of the characteristics of the two materials taken individually, and for the optimal transfer of the loads imposed by the matrix to the fiber. The interface between fiber and matrix is necessary to transfer the load from the matrix to the fiber. We can better define the concept of interface considering that

it must not be understood as a simple superficial superposition of two materials, but as a real "three-dimensional construction" of a so-called "thin third layer" generated by the intercalation of the two materials at a given distance from the superficial level. This is also reflected in different properties near the interface relative to the bulk of the material.[2]

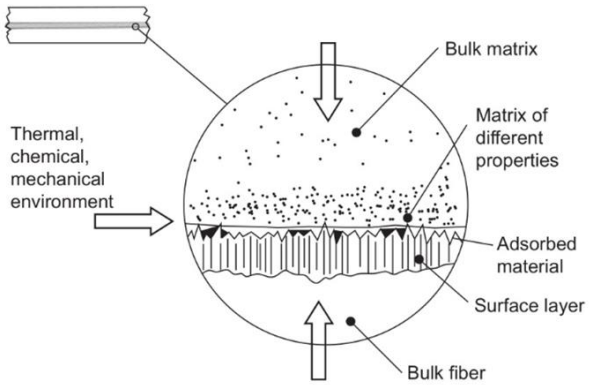

Figure 11. Interface representation in composite materials (Lim G. et al. 2020)[2]

Different types of interfaces are listed below:

a) Molecular entanglement: also known as mechanical bond, it is given by actual interweaving and knots between medium-long chain lateral ramifications.[35]

b) Electrostatic attraction: all secondary interactions such as dipole-dipole, ion-dipole and H-bonds are electrostatic in nature and are established thanks to the presence of polar groups, characterized by the presence of electronegative atoms, in particular N and O.[36]

c) Interdiffusion: elements deriving from materials diffuse between them as if they formed a mixture.[37]

d) Covalent bonds: they are given by the reaction between side groups such as for example. -OH, -NH_2, -COOH etc.[38]

e) Chemical reaction: through a reaction that occurs between substances applied to the material surfaces, a third substance is generated which acts as a glue.[39]

f) Mechanical interlock: simple mechanical interlocking which is as effective as the surfaces are rough and with grooves.[40]

Problems of natural fiber-polymer composites

As explained previously, the use of natural fibers in the construction of polymeric matrix composite materials is made difficult mainly by three factors: the hygroscopicity of the fibers, the high heterogeneity and the poor adhesion power with the polymeric resins used in high performance fields. The difficulty in creating an interface in natural fiber-polymer composites is linked to the hydrophilic character of natural fibers, which is not very compatible with the hydrophobic character of most polymeric matrices. Hydrophilicity is given by the presence of numerous -OH groups on the cellulose chains, which establish both inter- and intramolecular hydrogen bonds, which make the separation of the individual chains difficult by providing a very small contact surface for the establishment of the interface.[8] What happens can be compared to the hydrophobic effect that occurs with oil droplets in water. The high hydrophilicity and hygroscopicity generate problems during the polymerization cycle at high temperatures and pressures in the production of composite materials with resins. The release of water vapor, initially present in the fibers, inside the material during high heat and pressure treatments in an autoclave or press, leads to the formation of countless structural defects in the final material, compromising the quality of the interface and consequently the quality of the final performance of composite materials. Finally, the high heterogeneity of the biochemical and structural characteristics of the fibers causes difficulties in standardizing the production processes of composite materials.

Modification techniques

To solve these problems, treatments are implemented to modify the characteristics of natural fibers and make them more compatible with polymeric resins, or to lower the hygroscopicity and homogenize the materials. The following table shows the most common treatments (Table 1):

Table 1. The most diffused modification techniques of natural fibres. Tanasã et al. (2020)[8]

Chemical	Physical	Chemical-Physical	Biological
Mercerization/Alkali Treatment	Steam explosion process (STEX)	Plasma treatments	Fungi treatment
Acetylation	Thermo-mechanical processes	Corona discharge treatment	Enzymatic treatment
Silanization		Dielectric-barrier discharges	Bacterial treatment
Maleation		High energy radiation methods	
Graft Copolymerization		Ultrasonication	
Others			

The above treatments can be roughly divided into chemical, physical, chemical-physical and biological. They are implemented to eliminate the amorphous matrix, composed of hemicellulose and lignin, present in the fibers, to lower the hygroscopicity and increase the purity of the cellulose. The simplest and most advantageous treatment from an industrial point of view is Mercerization / Alkali Treatment which we will describe in detail later. Unlike chemical processes, physical and biological processes have the advantage of not using substances that can be dangerous to handle, and do not require further treatments to eliminate unreacted substances or by-products. However, they have several disadvantages, in fact they are generally very expensive processes that require special equipment and the fiber purification step is uncontrollable and non-homogeneous.[8]

Mercerization

From an industrial point of view, mercerization (or alkaline treatment) represents the simplest and most economical solution. It is often used as a preliminary treatment for other more complex functionalizations, as it is always desirable to purify the cellulose from the other amorphous components as much as possible. The main purpose of mercerization is to break the primary and secondary interactions that bind hemicellulose, lignin and other amorphous components to cellulose. Furthermore, cellulose can also suffer a weakening of its structure due to the decrease in inter- and intramolecular hydrogen bonds. In this way, after treatment a fiber enriched in cellulose is obtained, which has much more empty space between its chains in the microfibrils. This is where the second phase of the treatment comes into play: regeneration in distilled water. In this step the fiber is immersed in a bath of distilled water, to favor the reassembly mechanisms of the cellulose chains thanks to the formation of new -OH groups which can establish new hydrogen bonds. Thanks to the greater interchain space available, cellulose has the possibility of assembling into more compact and resistant crystalline structures, generating the so-called cellulose II (Figure 10b). A schematic representation of the two Mercerization steps is given in Figure 12.

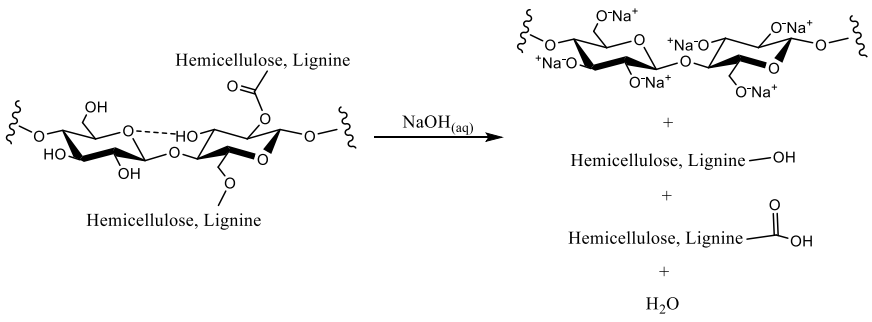

a

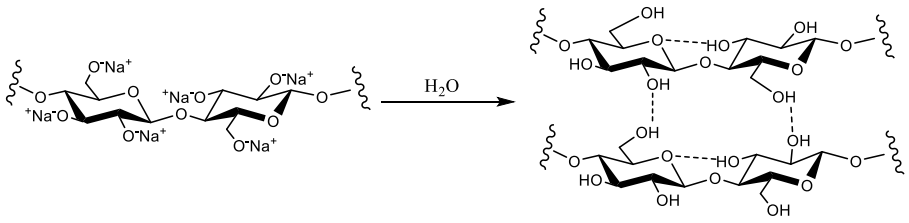

b

Figure 12. Mercerization steps: a) alkaline solution immersion; b) regeneration phase.

The quality of the final product of the treatment, i.e. the fiber with new biochemical and physical characteristics, depends on various parameters that can be modulated during the treatment itself. They are: the temperature at which the fibers are immersed in the NaOH solution; the immersion time; the concentration of NaOH and therefore the pH of the alkaline solution; the regeneration time. The difficulty of the treatment lies precisely in finding the right combination between the different parameters depending on the type of starting fiber, and this was the main objective of my doctoral work.

Hemp and flax fibres in high performance application

In the field of composite materials there are many fibres of plant origin that are studied and used. For example, bamboo, sisal, kenaf, hemp, linen, cotton and many others are widely used in many fields such as construction, aeronautics, nautical, automotive, etc. For applications where the best mechanical and physical performances are required, such as for example for the external covering of aircraft, boat hulls and sports car bodies, where high mechanical stresses of the materials used are reached, hemp and flax have been identified as the best candidates to fill this role and replace synthetic materials such as carbon and fiberglass.[41]
In Table 2 some examples of natural fibres characteristics are reported.

Table 2. Mechanical properties and composition of the most common natural fibres. Khalid et al. (2021)[41]

Natural Fibers/ Propertes	Cotton	Jute	Hemp	Coir	Date palm	Flax	Sisal	Pineapple
Elongation (%)	3-10	1,5-1,8	1,6	15-30	2-19	1,2-3,0	2-14	14
Density (g/cm^3)	1,5-1,6	1,3-1,4	1,4	1,2	0,9-12	1,4-1,5	1,3-1,5	1,4
Tensile Strenght (MPa)	280-580	400-800	550-900	175-220	300-800	400-1500	400-700	400-1600
Cellulose (%)	82-91	60-70	71-75	32-42	46	71	67-78	70-82
Lignine (%)	-	12-13	3,7-5,7	40-45	20	2,5	8-11	5-12
Tensile Modulus (GPa)	6-13	10-30	70	4-6	7	28-80	9-38	34-82

The growing interest in hemp is due to its suitability in meeting the high need for environmental protection due to the increase in air temperature and related climate changes. Hemp is an annual plant characterized by a well-developed leaf system and is one of the fastest growing plants on Earth. It can absorb more than 10 tons of CO_2 from the atmosphere, thus contributing to lowering the greenhouse effect. Additional benefits of growing hemp include suppression of weed growth, anti-erosion, remediation properties and the ability to drain the soil of organic pollutants and heavy metals. The ability of hemp plants to kill resistant weeds comes from several factors such as the thickness of the leaves, the height of the plants and the fact that they can be grown densely.[42]

Flax plants are characterized by the importance of the single stem, the short vegetative cycle, the resistance to lodging and parasites, the productivity and the technological qualities of the fibers. The range of flax varieties is very wide and the selection criteria depend on the specific cultivation

conditions, taking into account disease problems and the nature of the soil. According to the Commission Report of 20 May 2008 to the Council and the European Parliament "the cultivation of flax has positive effects on the diversity of ecosystems and offers a beneficial environmental change for soil quality, biodiversity and landscapes".

Linen is a species to be considered with low environmental impact, in fact linen not only requires reduced fertilization, but the robustness of its fibre extends the life cycle of the products obtained. Flax is considered a soil improver, because it has a low requirement for inputs, such as fertilizers, pesticides and herbicides, and above all it has a root system that develops in depth, improving the structure and fertility of the soil.[43]

Experimental

Materials and Methods

HP Composites supplied flax and hemp fabrics with a 0-90 warp/weft structure, that is two bundles of fibers intertwined with directions orthogonal to each other. Fibers were characterized using IR spectroscopy, TGA, SEM, AFM and XRD analysis. IR spectra were recorded from 4000 to 400 cm−1 with a PerkinElmer Spectrum 100 FT-IR instrument. Thermal gravimetric analyses (TGA) were carried out in a N_2 stream with a PerkinElmer STA 6000 simultaneous thermal analyser (heating rate: 30 °C/min). SEM spectra and EDX analyses were carried out using a Scanning Electron Microscope Zeiss Sigma 300 FESEM (Field Emission SEM).

XRD analyses were performed with a Philips PW 1710 diffractometer (Bruker, Rivas-Vacia, Madrid, Spain) provided with a CuKα radiation and a nickel filter that removes κβ radiation.

For the alkaline treatments, 98% purity NaOH tablets and distilled water were used to prepare the alkaline solutions. The fiber treatments were carried out in a ventilated oven at a controlled temperature. To prepare the

samples for subsequent characterizations, the fibers were finely pulverized using the Vibromill MV-400.

Preparation of the samples

The flax and hemp fabrics were cut into 7 cm x 7 cm squares and the samples thus obtained were dried in an oven at 80 ° C for 24 h. They were weighed with an analytical balance and the masses of samples were all in the range between 1.5 and 2 grams (g). The alkaline treatment was performed by immersing each sample in 50 mL of basic solution, using sealed flasks.

Procedure of Treatments

There are four parameters to be controlled in these processes, in detail:
(1) the concentration of the alkaline solution,
(2) the exposure temperature to alkaline treatment,
(3) the exposure time to alkaline treatment,
(4) the time of immersion in distilled water, that is the "regeneration" phase of the cellulose, after the alkaline treatment.
The last step is essential for the reconstitution of the -OH groups by removing the Na^+ cations. In this way the structural readjustment of the chains is allowed to the cellulose through the establishment of intra-chain and inter-chain H bonds, which will help to increase the degree of crystallinity of the polymer and to improve its mechanical characteristics and its processability in the production of composites with epoxy matrices.
The procedure for this study was based on the following fixed parameters:
(1) Alkaline solutions at different concentrations of NaOH, 0.5%, 1%, and 1.5 % m / v.
(2) The alkaline treatment temperatures investigated were two: 60 and 80°C.
(3) For each alkaline concentration, different exposure times were performed: 30, 90, 150 minutes.

(4) Each treated sample was finally immersed in a distilled water bath for 90 minutes (changing water every 30 minutes) controlling the pH that must be neutral at the start.

The fibers were then left to dry in an oven at 80°C for all the night and finally weighed to check the residual mass.

Results and Discussion

Virgin flax and hemp fibers characterization and comparison

First, we will briefly comment on the physico-chemical properties of virgin fibers. They were characterized through FT-IR spectroscopic analysis, thermal gravimetric analysis (TGA), SEM, AFM and XRD analysis. In the FT-IR spectra, shown in Figure 13, the characteristic absorptions of natural fibers can be observed, in detail: (a) an intense and broad band at 3312 cm^{-1} due to the stretching of the -OH groups present on the repetitive glucopyranoside units, through which intra-chain H-interactions are established, (b) between 2970 and 2840 cm^{-1} three low intensity absorptions corresponding to the stretches of the aliphatic C-H bonds, (c) low-intensity absorptions at 1408 and 1338 cm^{-1}, associated to the bending of the C-H and O-H bonds, (d) between 1100 and 1000 cm^{-1} very intense absorptions, corresponding to the C-O-C stretches of the ether and acetal groups present in the cellulose, (e) the intense band at 1712 cm^{-1} characteristic of the non-conjugated carbonyl, in accordance with the presence of ester groups, and (f) at 1241 cm^{-1} another intense band assignable to the ethereal groups of aromatic substances, typical of lignin.[44]

The hemp IR spectrum is very similar to pure cellulose, however the absorptions at 1712 cm^{-1} and 1245 cm^{-1} are not present. This evidence suggests the absence of strong covalent interactions such as ester and ether bonds between the cellulose and the amorphous matrix.

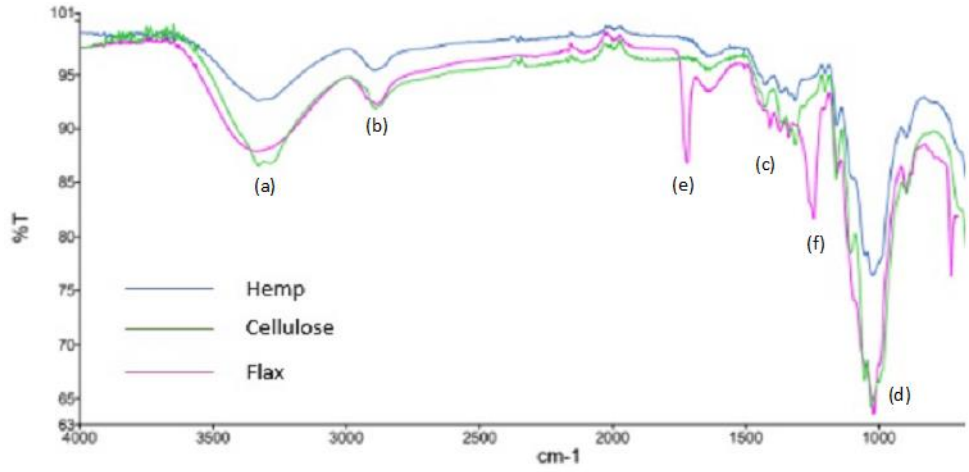

Figure 13. IR spectra of Hemp (blue), Cellulose (green) and Flax (purple)

The TGA analysis was carried out on the raw fibers powder under nitrogen flow at 20 ml/min, with a T ramp of 30°C/min. In Figure 14 the following steps can be identified from the flax TGA: (1) the starting thermal decomposition phase, which goes from about 255°C to about 342°C, (2) a phase of thermal degradation at a constant speed ranging from 342°C to 375°C approximately, (3) an abrupt slowdown in thermal degradation up to approximately 452°C, and (4) the mass of the sample remains almost constant at 20% up to 600°C. Each phase of the fiber thermal degradation is characterized by the percentage composition of the fiber itself. The curve shape is influenced by the presence of amorphous components such as hemicellulose and lignin, which influence the trend of thermal degradation of the cellulose. The percentage of residual mass is mainly influenced by lignin which, having a lower oxygen content than the other components, is the one that contributes most to the carbonaceous residue. This is also due to the high degree of branching and the high condensation of the aromatic fractions.[45–47]

On the other hand, observing the degradation curve of hemp, one notices the difference between 375°C and 452°C, in which the elongated hump that is instead seen for flax is absent. This fact is a further confirmation of the hypothesis made previously by analyzing the FT-IR analyses: probably, the interactions between cellulose and amorphous matrix in hemp are weaker, due to the absence of ester and etheric bonds. Therefore, the energy required to decompose hemp is lower than for flax. As regards

the beginning of the degradation phase, hemp is similar to flax: the curve between 255°C and 342°C is due to the presence of hemicellulose, which is the most thermally labile component.[14,48]

In fact, considering the curve of pure cellulose, it is possible to observe the fastest degradation of the polysaccharide alone, with a very short initial phase. Finally, it is possible to observe that the residue of the hemp mass is similar to flax, around 18%. This value is much higher than the pure cellulose residue, which is 7%.

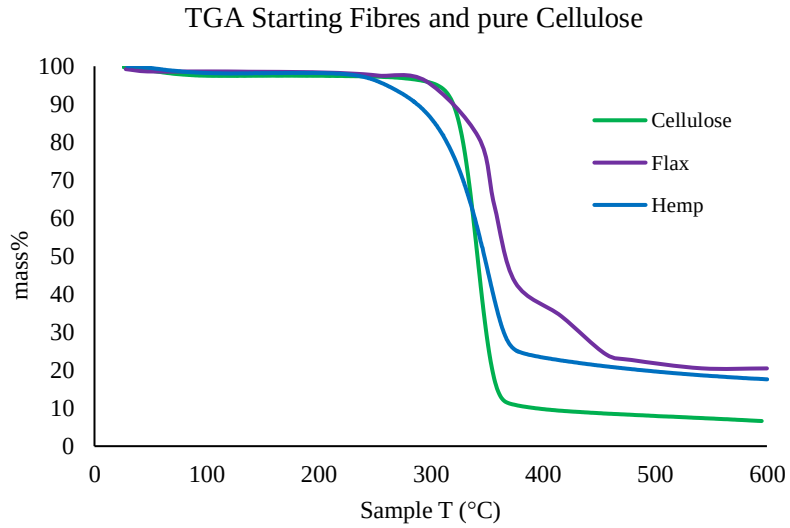

Figure 14. TGA Analysis of starting flax and hemp fibers, compared with pure cellulose I

The SEM images acquired at 5000 magnifications of the raw fibers are shown in Figure 15. From these images it is possible to observe the surface morphology of the two materials. Surface roughness is very low for flax (Figure 15A), due to the presence of amorphous components, and this would lead to poor adhesion due to mechanical interlocking between the reinforcement constituted by the fiber and the polymeric matrix which forms the final composite material. One of the objectives to be achieved through the alkaline treatment is therefore to increase the surface roughness. In this way it will be possible to obtain a better adhesion between the fiber and the polymeric matrix.[49]

Figure 15B shows the morphology of hemp which is also quite smooth, but still a better starting point than flax.

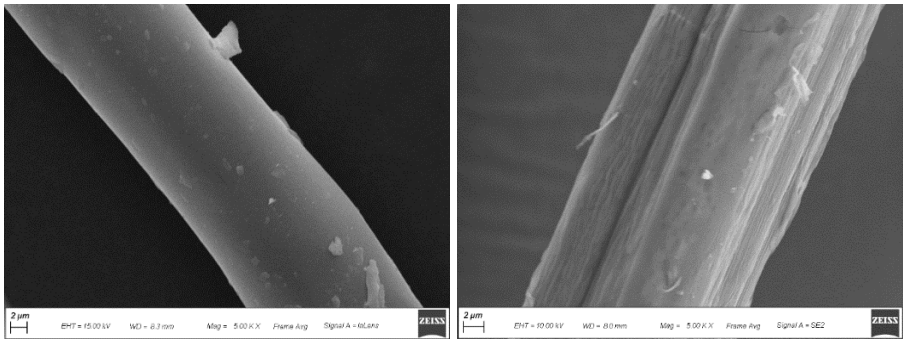

(A) **(B)**

Figure 15. SEM images at 5000 of magnification of (A) flax and (B) hemp.

Alkaline treatment

After being treated, the fibers were washed and left to soak in distilled water at pH 7. After 90 minutes, changing water every 30 minutes, the fibers were dried in an oven overnight and then weighed to verify how much mass percentage was lost. This mass corresponds to the amount of amorphous matrix extracted from the fiber. From the graphs in Figure 16 A-F, it is possible to see that the most important parameter influencing the extractive capacity of the fiber mercerization process is temperature, since the 80°C treatment is the most effective and it enhance the effects of others parameters. This suggests that the hydrolysis process of the amorphous components of the fibers is strongly endothermic.

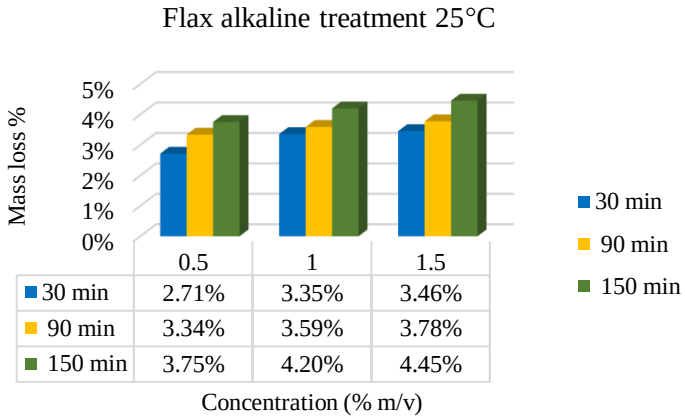

A

Hemp alkaline treatment 25°C

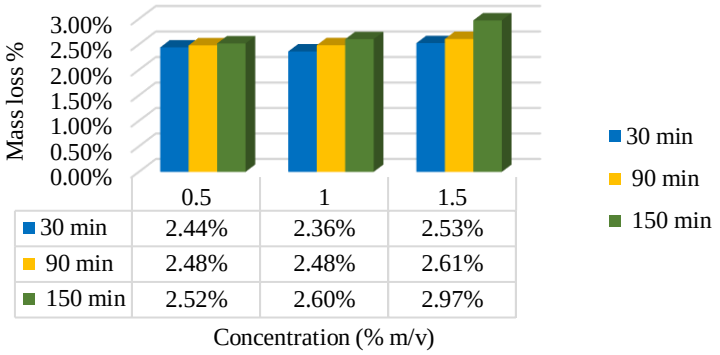

B

Flax alkaline treatment at 60°C

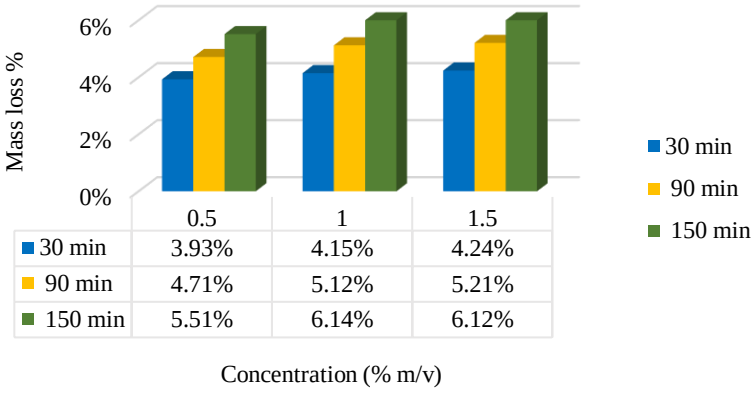

C

Hemp alkaline treatment 60°C

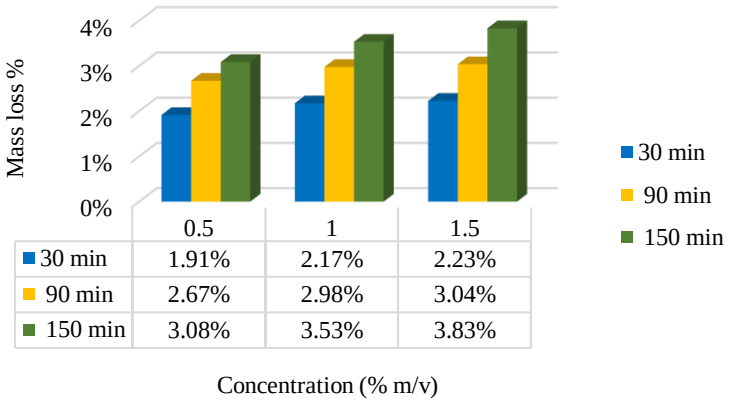

D

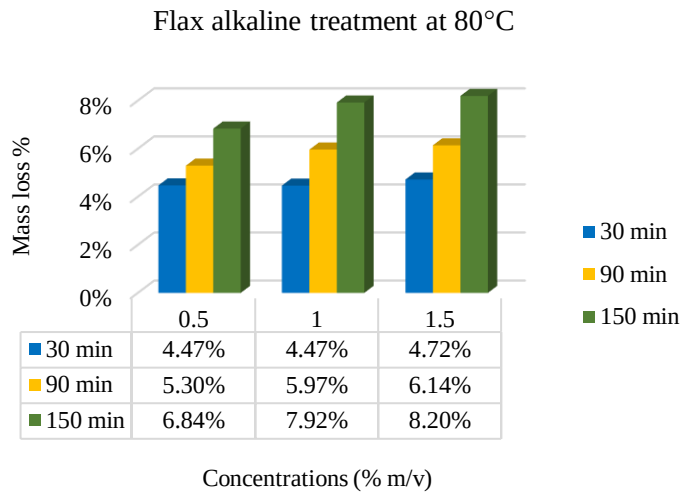

E

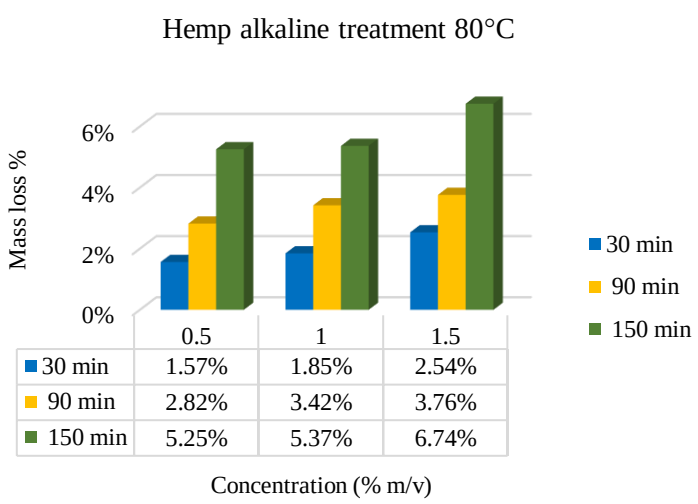

F

Figure 16. (A) Alkaline treatment of flax at 25°C; (B) Alkaline treatment of hemp at 25°C; (C) Alkaline treatment of flax at 60°C; (D) Alkaline treatment of hemp at 60°C; (E) Alkaline treatment of flax at 80°C; (F) Alkaline treatment of hemp at 80°C.

By increasing the immersion time in alkaline solution, the amount of mass loss increases. The parameter that seems to have less influence on the amount of mass extracted is the concentration of NaOH. Negligible differences are observed between treatments with alkaline solution of concentrations 0.5% m/v, 1.0% m/v and 1.5% m/v, and for the same temperature and time of immersion in alkaline solution, the mass of the extracted amorphous matrix is very similar among the various samples. This would suggest that large differences are not obtained for small variations in the concentration of alkaline solution. As it is known from

many data in the literature,[6,41] the chemical composition and structural characteristics of natural fibers change considerably depending on many factors, such as the climate of the region where the plant grows, the type of land, the cultivation period, and therefore the amount of sunlight that the plant receives, the harvesting period, the harvesting method, and finally the processing method to obtain the fibers and fabrics. So, it is likely that the starting hemp, objects of this study, possesses less amount of hemicellulose, lignin and others amorphous matrix components.

TGA Analysis of samples treated

The treated fibers samples have been analyzed at TGA to verify the purification degree obtained after alkaline treatment.[41]

It has been seen that the trends of these curves are very similar to each other, therefore the TGAs of the three most representative samples of treated fibers were taken and compared with the degradation curves of raw fibers and pure cellulose purchased by Sigma Aldrich (Figure 17). All TGA analysis are conducted over nitrogen flux at 20 ml/min, starting from 30°C to 600°C, with a temperature rump of 30°C/min. The shown samples are Flax and Hemp treated at 0.5% and 30 min, 1.0% and 90 min, 1.5% and 150 min, for each temperature: 25°C, 60°C and 80°C.

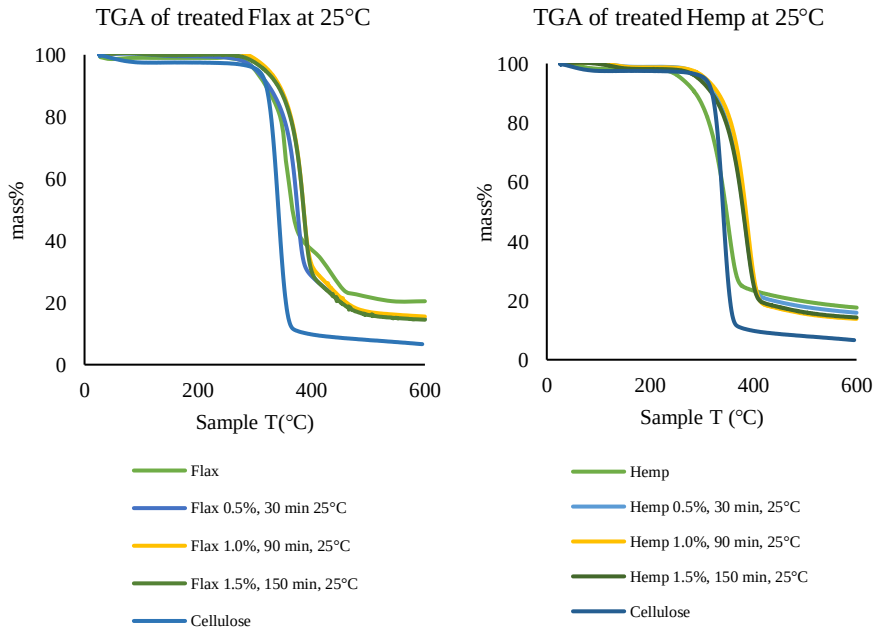

A B

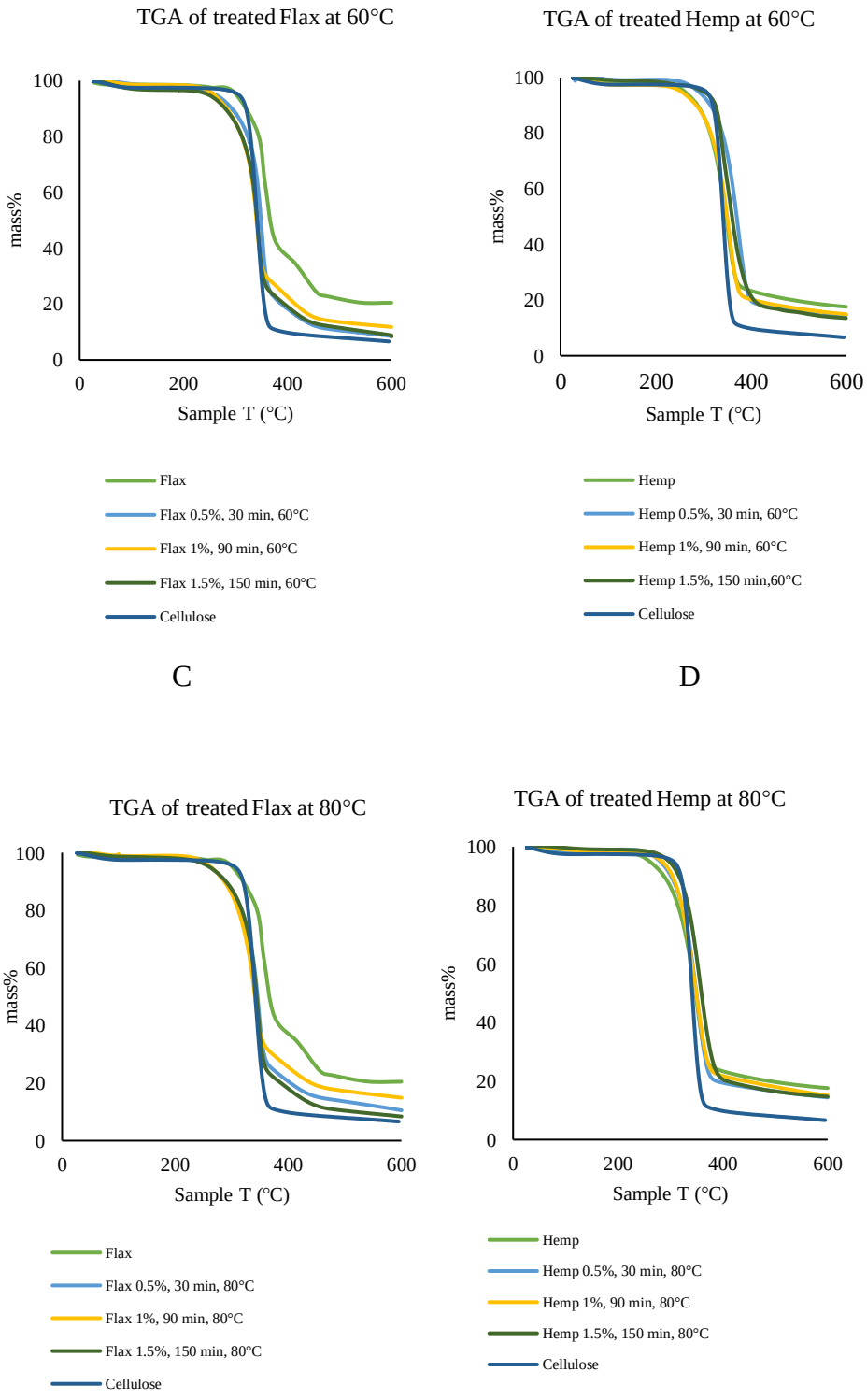

Figure 17. TGA analysis of the most representative samples of treated fibres, compared to starting materials and pure Cellulose.

The first observation is that untreated flax has a degradation curve with less slope than the other curves; it has a much broader initial degradation phase ranging from about 270°C to 330°C; at about 380°C there is a first

inflection point, where the curve develops in a concave way, up to a second inflection point at about 460°C; the degradation ends with a residual mass of about 20%, much higher than the other curves. The second reference used is pure cellulose. The maximum slope of its thermal degradation is reached between 330°C and at about 365°C. After that, there is an inflection point, with the residual mass around 10% which decreases until 7% to 600°C. By observing the thermal degradation of flax (Figures 17A, 17C and 17E), compared to pure cellulose, it is noted that the treatments carried out with different conditions bring to significant differences with respect to the starting material. In fact, a substantial lowering of the degradation curve is observed between 375°C and 452°C, and it is possible to assume that they are not anymore, the strong interaction between flax cellulose and amorphous components like lignin. Furthermore, a greater slope of the curve between 342 °C and 375 °C is evident, which means that the treated flax degrades with a greater speed, very similar to that of pure cellulose; the degradation start temperature is lower, and this could be linked to the lower quantity of lignin present, which is the most thermally resistant component. Finally, the % of residual mass at 600°C drops considerably, around 10% for the fibers treated at 60°C and 80°C. This result is also due to the lower quantity of lignin present in the treated flax. It is possible to observe that the treatment at room temperature is less efficient, in fact the residual mass at the end of analysis is around 15% (Figure 17A). No important differences are observable between the various treated flax samples at the same temperature. It is a confirmation of the more importance of the temperature effect for the alkaline treatment. Concerning hemp, it can be observed that alkaline treatments under different conditions did not cause significant changes in the thermal behavior of the treated samples compared to the untreated reference hemp. The rate of degradation, the shape of the curve and the residual mass at 600°C remain very similar to the reference sample. The results of the thermal tests of both treated materials are a confirmation of the hypothesis made previously, that the starting hemp has a lower quantity of hemicellulose, lignin and other components of the amorphous matrix.

SEM Analysis of samples treated

SEM analyses were performed to obtain information on the morphology of the treated fibers. From the surface morphology of the fibers, it is in fact possible to obtain interesting information on the possible adhesion capacity of the fibers to the polymeric matrix, during the processing phase of composite materials.[26,49]

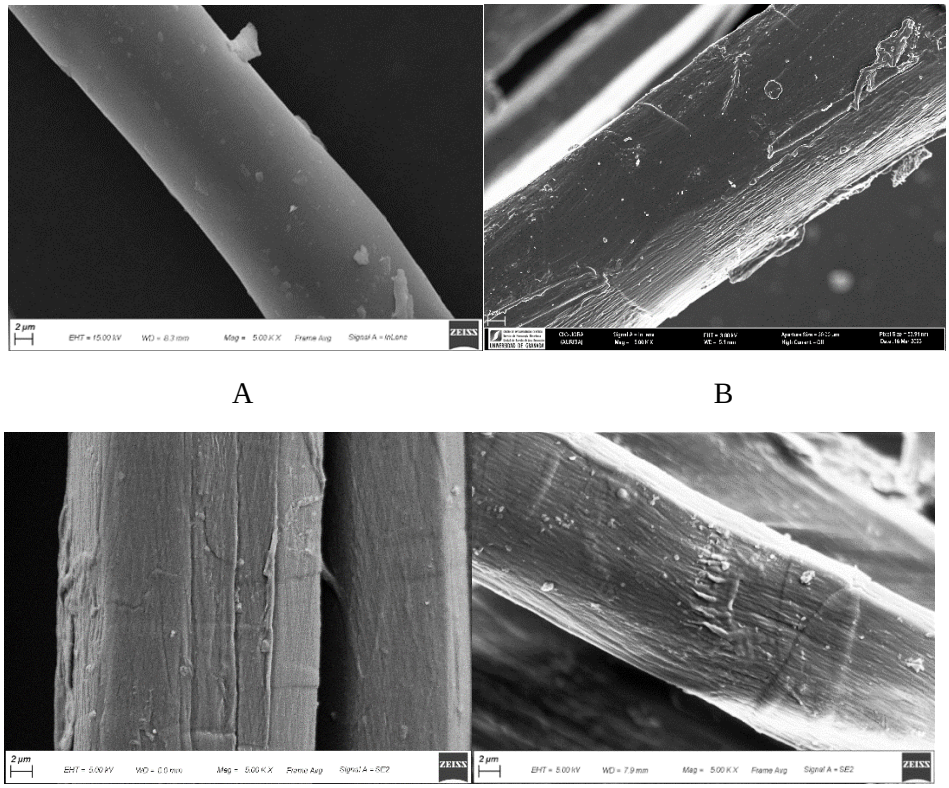

A B

C D

Figure 18. SEM images at 5000 of magnification of (A) starting flax, (B) flax treated at 0.5%, 30min, 25°C and (C) flax treated at 1.0%, 90min, 60°C. (D) flax treated at 1.5%, 150min, 80°C.

Figure 18A shows the untreated flax, while Figures 18B, 18C and 18D show the flax fibers treated respectively in 0.5% NaOH alkaline solutions, for 30 min of immersion at 25°C, in alkaline solution at 1.0% NaOH, for 90 min of immersion at 60°C and in alkaline solution at 1.5% NaOH, for 150 min of immersion at 80°C. It can be observed that treatment with a more concentrated alkaline solution produces a sample with a much

rougher morphology. Indeed, in Figure 18D, they are much more visible than the depressions and grooves which are an important advantage when processing fibers together with polymer resins, to obtain a stronger interface for mechanical interlocking. Furthermore, it is possible to observe on the surface a series of parallel filaments, which develop along the vertical axis of the fiber. These filaments are called microfibrils and the angle formed by the vertical axis of the fiber and their direction of propagation is the microfibrillar angle (MFA). This angle is closely related to the quality of the mechanical properties of the fiber: the smaller it is, the better the mechanical properties of the fiber. Flax and hemp have a microfibrillar angle between 8° and 11° and their chemical composition, cellulose content and degree of crystallinity make flax and hemp the best natural fibers for high performance applications.[27]

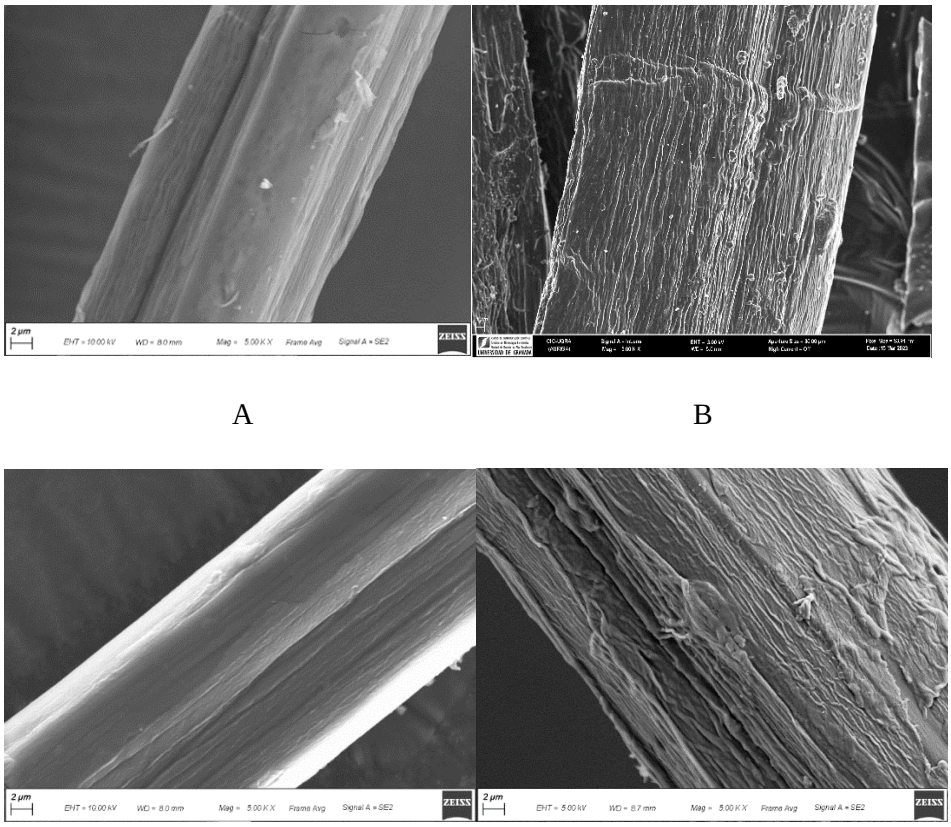

A B

C D

Figure 19. SEM images at 5000 of magnification of (A) not treated hemp, (B) hemp treated at 0.5%, 30 min, 25°C, (C)hemp treated at 1.0% 90 min, 60°C and (D) hemp treated at 1.5%, 150 min, 80°C.

In the case of hemp fibers (Figure 19 A, B, C and D), it is possible to observe the same results: the alkaline treatment with a more concentrated NaOH solution gives the greatest morphological modification, and a greater degree of surface roughness is obtained. It is also important to highlight the fact that the dimensions of the individual fibers are very heterogeneous.

In the field of composite materials, the search for alternative materials is constantly growing. The goal is to be able to use materials deriving from renewable sources, with a low environmental impact, and which can be introduced into a circular economy system. Natural fibers, especially lignocellulosic fibers, are potential substitutes for synthetic fibers such as carbon and glass fibers.

XRD Analysis

X-ray diffraction method is important to verify structural characteristics of treated fibres, that should be modified during the regeneration step, after the treatment in alkaline solution. In plant fibers, two distinct diffraction peaks are observed. The first peak is around 2θ = 18, corresponding to the 1 0 1 plane, which indicates the presence of amorphous constituents such as hemicellulose, pectin, lignin, wax, etc. The second peak is located along the reticular plane 0 0 2, where 2θ is observed around the value of 22 θ corresponding to cellulose I. The crystallinity index of cellulose I (CI) can be estimated with the following equation (Eq.1) developed by Segal (1959):

$$CI = \frac{I_{002} - I_{am}}{I_{002}} x\ 100$$

Equation 1

Where I_{002} is the maximum intensity of the diffraction peak in the crystalline plane 0 0 2 and I_{am} is the diffuse intensity from the amorphous fraction of the sample corresponding to 2θ = 18°.[49]

Here an example from the literature (Figure 20):

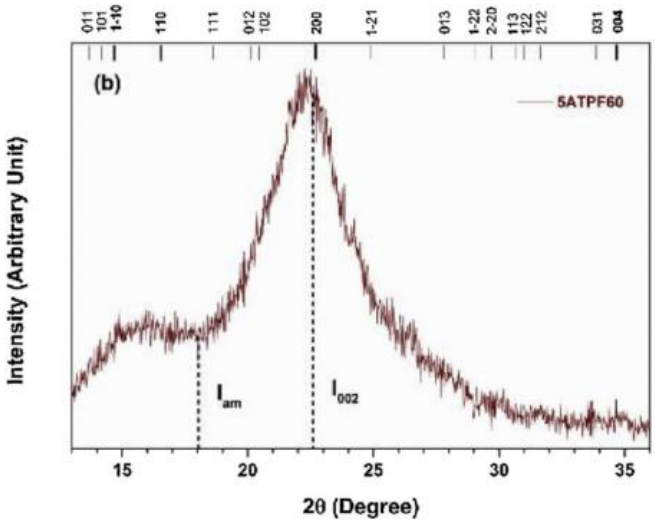

Figure 20. Example of XRD of cellulose I_β (Kathirselvam et all.) [49]

The size of the crystallites (CS) of the fibres is another important parameter and it is inversely proportional to the peak width at 22°.

The shape of the peak is very important to identify the alloform of Cellulose. Here an example from the literature (Figure 21):

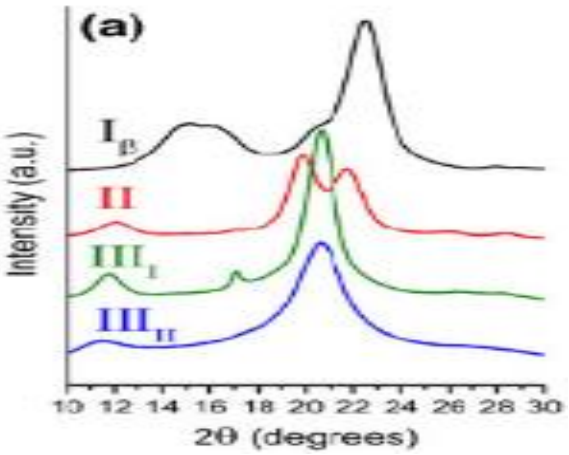

Figure 21. XRD shape of different alloform of cellulose. [29]

Considering these informations, it is possible evaluate the effect of alkaline treatments on the crystallinity of the cellulose contained in the treated flax and hemp samples.

Follow the CI values of fibres are reported:

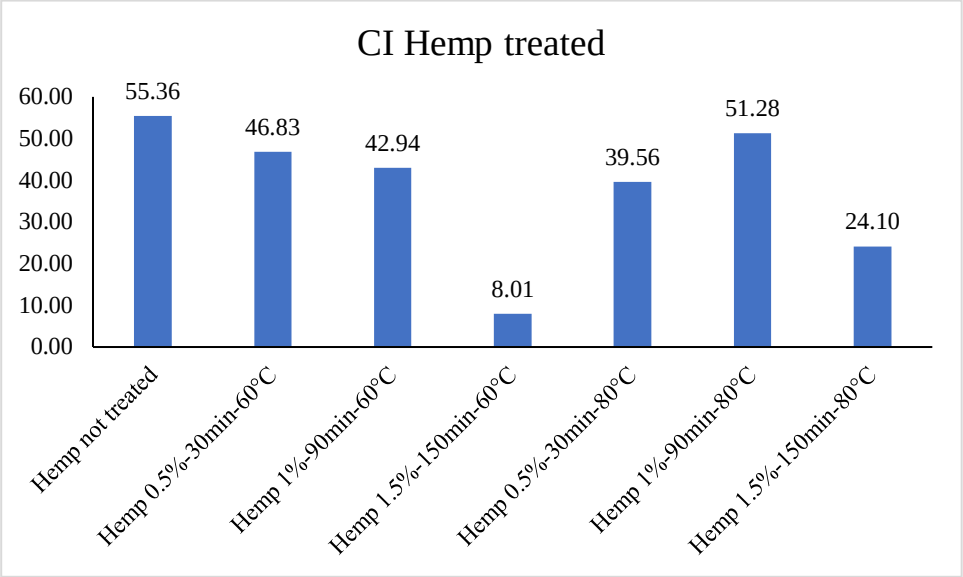

A

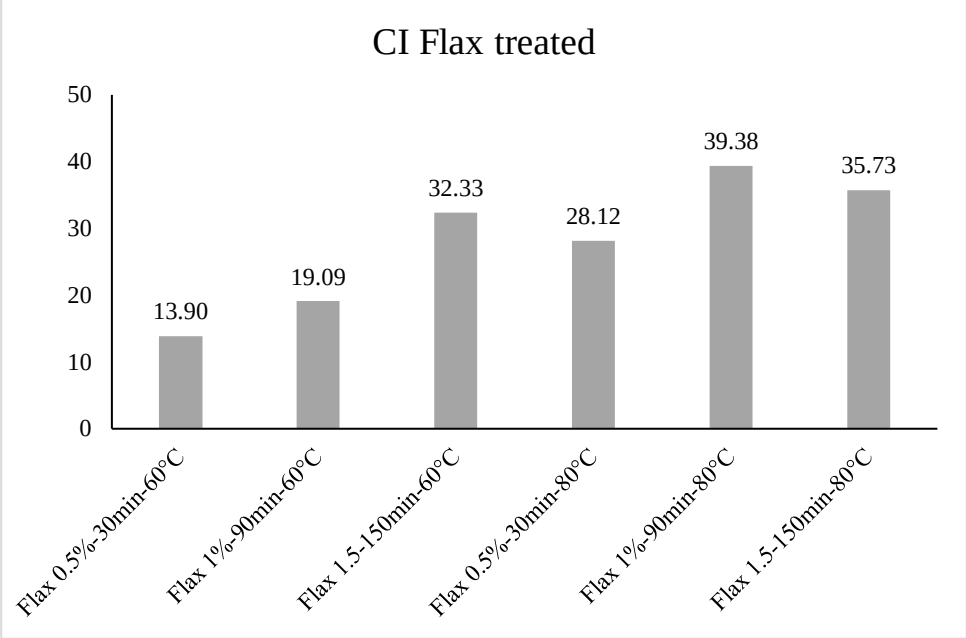

B

Figure 22. Graphical representation of Crystallinity Index of Hemp (A) and Flax (B).

Considering the Figure 22A, the CI of hemp treat is lower than CI of hemp not treated. For the samples treated at 60°C the crystallinity index lowering raising the treatment parameters. On the contrary, the samples treated at

80°C show the opposite behaviour, except for the hardest treatment. At this point it is possible to make two assumptions: the first is that the treatments are too aggressive and irreversibly damage the structure of the cellulose in the treated fibres; the second is that the regeneration time of the fibre in distilled water, used in this study, of an hour and a half is not enough to promote the restructuring of cellulose crystallites.

Considering the Figure 22B, the treatments have a good impact on CI of flax treated. So, it is possible to assume that for flax the treatment parameters are right and cellulose and the cellulose is not damaged.

Probably, only the hardest treatment could need of a regeneration time higher of 90 minutes. Unfortunately, the data of untreated flax is not available for an instrumental problem.

Some graphs of the x-ray analysis of fibre samples are given below (Figure 23 and 24):

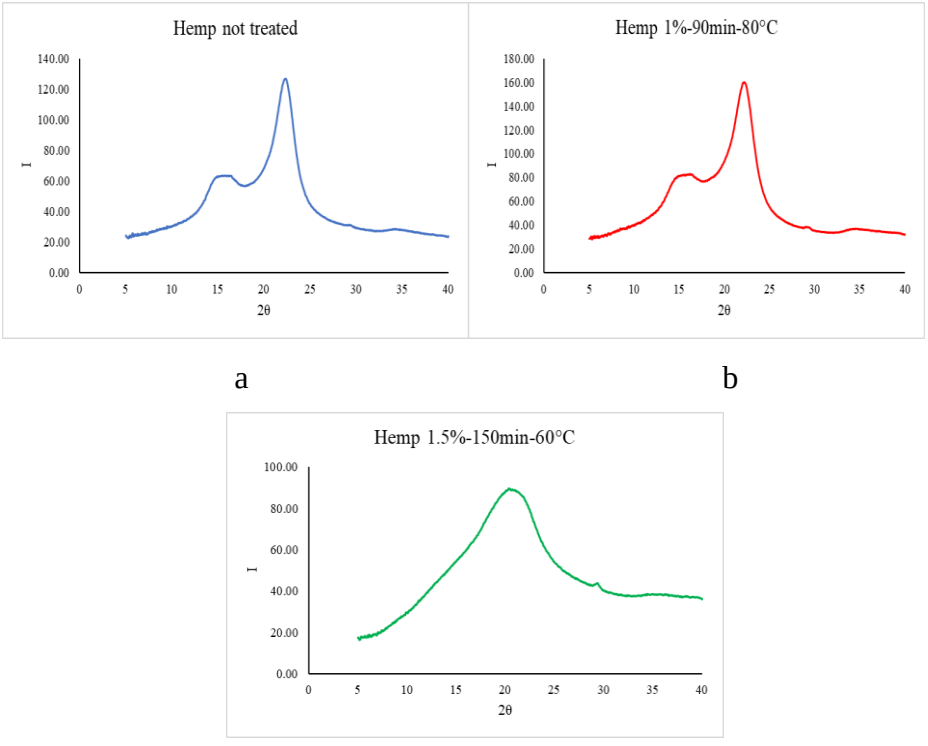

Figure 23. X-Ray analysis of hemp not treated (a), hemp 1%-90min-80°C (b) that is the best sample and hemp 1.5%-150min-60°C (c) that is the worst sample.

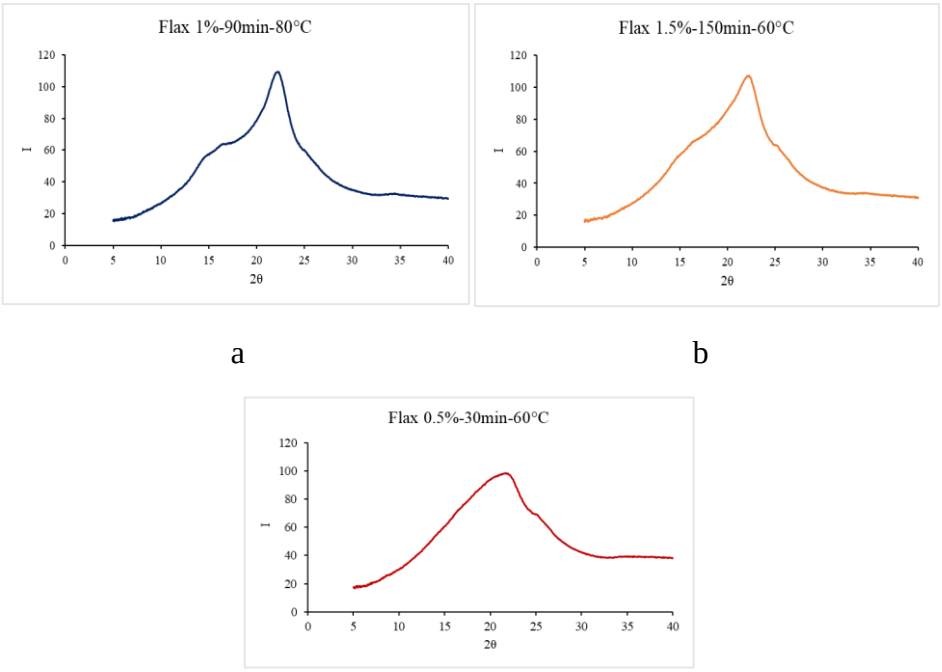

Figure 24. X-Ray analysis of flax 1%-90min-80°C (a) the best result, flax 1.5%-150min-60°C (b) the intermediate and flax 0.5%-30min-60°C (c) the worst.

It is interesting to observe that higher is CI and narrower are the peaks. This fact is correlated with the crystallites size of cellulose contained in fibres. Probably, a longer time of regeneration is needed to promote the recrystallisation of cellulose. Unfortunately, the transormation from cellulose I to cellulose II is not observe for any sample.

Conclusions

In this work, treatments in alkaline solution have been studied aimed at improving some characteristics of linen and hemp fabrics. It has been found that temperature is the parameter that most influences the extraction capacity of the treatment of amorphous components such as hemicellulose and lignin. As regards the other parameters investigated, it was found that they do not determine substantial differences between the treated samples. However, they cause important changes in the characteristics of the treated fibers with respect to the starting raw materials. The SEM images show very interesting results on the morphology, and it is clear that the higher the concentration of NaOH in the solutions used for the alkaline treatment,

the greater the modification of the surface characteristics, in particular the roughness which can lead to a better interaction between the fibers and the polymeric matrices, through mechanical interlocking, in the preparation of composite materials. The small NaOH concentration differences do not produce important effects in the extraction of amorphous components, but the immersion time is a parameter to be taken into consideration.

Future studies will have to verify the efficiency of treated fibers in obtaining better composite materials than those made with untreated fibers. From an industrial point of view, it is important to optimize the various parameters of a process also from an economic point of view, with the best results in terms of mechanical properties of the final composite materials.

References

(1) Santeramo, F. G. Circular and Green Economy: The State-of-the-Art. *Heliyon* **2022**, *8* (4), e09297. DOI: 10.1016/j.heliyon.2022.e09297.

(2) Goh, K. L., Aswathi, M. K., De Silva, R. T., Thomas, S., Eds.; *Interfaces in Particle and Fibre Reinforced Composites: Current Perspectives on Polymer, Ceramic, Metal and Extracellular Matrices*; Woodhead Publishing series in composites science and engineering; Woodhead Publishing, an imprint of Elsevier: Duxford Cambridge, MA Kidlington, 2020. ISBN: 9780081026656

(3) Akil, H. M.; Omar, M. F.; Mazuki, A. A. M.; Safiee, S.; Ishak, Z. A. M.; Abu Bakar, A. Kenaf Fiber Reinforced Composites: A Review. *Materials & Design* **2011**, *32* (8–9), 4107–4121. DOI: 10.1016/j.matdes.2011.04.008.

(4) Carbon-Containing Polymer Composites, M. Rahaman, D. Khastgir, A. K. Aldalbahi, Springer **2019**. ISBN: 9789811348013.

(5) Ahn, H.; Yeo, S. Y.; Lee, B.-S. Designing Materials and Processes for Strong Polyacrylonitrile Precursor Fibers. *Polymers* **2021**, *13* (17), DOI: 10.3390/polym13172863.

(6) Vinod, A.; Sanjay, M. R.; Suchart, S.; Jyotishkumar, P. Renewable and Sustainable Biobased Materials: An Assessment on Biofibers, Biofilms, Biopolymers and Biocomposites. *Journal of Cleaner Production* **2020**, *258*, 120978. DOI: 10.1016/j.jclepro.2020.120978.

(7) Khalid, M. Y.; Imran, R.; Arif, Z. U.; Akram, N.; Arshad, H.; Al Rashid, A.; García Márquez, F. P. Developments in Chemical Treatments, Manufacturing Techniques and Potential Applications of Natural-Fibers-Based Biodegradable Composites. *Coatings* **2021**, *11* (3), 293. DOI: 10.3390/coatings11030293.

(8) Tanasă, F.; Zănoagă, M.; Teacă, C.; Nechifor, M.; Shahzad, A. Modified Hemp Fibers Intended for Fiber-reinforced Polymer Composites Used in Structural Applications—A Review. I. Methods of Modification. *Polymer Composites* **2020**, *41* (1), 5–31. DOI: 10.1002/pc.25354.

(9) Bahrami, R.; Bagheri, R.; Dai, C. Influence of Fine Structure on the Variations of Thermal and Mechanical Properties in Flax Fibers Modified with Different Alkaline Treatment Conditions. *Journal of Natural Fibers* **2022**, *19* (13), 5239–5257. DOI: 10.1080/15440478.2021.1875367.

(10) Azwa, Z. N.; Yousif, B. F. Characteristics of Kenaf Fibre/Epoxy Composites Subjected to Thermal Degradation. *Polymer Degradation and Stability* **2013**, *98* (12), 2752–2759. DOI: 10.1016/j.polymdegradstab.2013.10.008.

(11) Hassan, F.; Zulkifli, R.; Ghazali, M. J.; Azhari, C. H. Kenaf Fiber Composite in Automotive Industry: An Overview. *International Journal on Advanced Science, Engineering and Information Technology* **2017**, *7* (1), 315. DOI: 10.18517/ijaseit.7.1.1180.

(12) Kumaravel, S.; Thiruvengetam, P.; Karthick, K.; Sankar, S. S.; Karmakar, A.; Kundu, S. Green and Sustainable Route for Oxidative Depolymerization of Lignin: New Platform for Fine Chemicals and Fuels. *Biotechnology Progress* **2021**, *37* (2), e3111. DOI: 10.1002/btpr.3111.

(13) Questell-Santiago, Y. M.; Galkin, M. V.; Barta, K.; Luterbacher, J. S. Stabilization Strategies in Biomass Depolymerization Using

Chemical Functionalization. *Nat Rev Chem* **2020**, *4* (6), 311–330. DOI: 10.1038/s41570-020-0187-y.

(14) Väisänen, T.; Batello, P.; Lappalainen, R.; Tomppo, L. Modification of Hemp Fibers (Cannabis Sativa L.) for Composite Applications. *Industrial Crops and Products* **2018**, *111*, 422–429. DOI: 10.1016/j.indcrop.2017.10.049.

(15) Gassan, J.; Mildner, I.; Bledzki, A. K. Influence of Fiber Structure Modification on the Mechanical Properties of Flax Fiber-Epoxy Composites. *Mech Compos Mater* **1999**, *35* (5), 435–440. DOI: 10.1007/BF02329330.

(16) Avril, C.; Bailly, P. A.; Njuguna, J.; Nassiopoulos, E.; Larminat, A. D. DEVELOPMENT OF FLAX-REINFORCED BIO-COMPOSITES FOR HIGH-LOAD BEARING AUTOMOTIVE PARTS. **2012**.

(17) Northolt, M. G.; Boerstoel, H.; Maatman, H.; Huisman, R.; Veurink, J.; Elzerman, H. The Structure and Properties of Cellulose fibres Spun from an Anisotropic Phosphoric Acid Solution. **2001**, *42* (19), 8249-8264. DOI: 10.1016/S0032-3861(01)00211-7

(18) Åkerholm, M.; Hinterstoisser, B.; Salmén, L. Characterization of the Crystalline Structure of Cellulose Using Static and Dynamic FT-IR Spectroscopy. *Carbohydrate Research* **2004**, *339* (3), 569–578. DOI: 10.1016/j.carres.2003.11.012.

(19) Evans, R.; Newman, R. H.; Roick, U. C.; Suckling, I. D.; Wallis, A. F. A. Changes in Cellulose Crystallinity During Kraft Pulping. Comparison of Infrared, X-Ray Diffraction and Solid State NMR Results. *hfsg* **1995**, *49* (6), 498–504. DOI: 10.1515/hfsg.1995.49.6.498.

(20) Rao, J.; Lv, Z.; Chen, G.; Peng, F. Hemicellulose: Structure, Chemical Modification, and Application. *Progress in Polymer Science* **2023**, *140*, 101675. DOI: 10.1016/j.progpolymsci.2023.101675.

(21) Reshmy, R.; Athiyaman Balakumaran, P.; Divakar, K.; Philip, E.; Madhavan, A.; Pugazhendhi, A.; Sirohi, R.; Binod, P.; Kumar Awasthi, M.; Sindhu, R. Microbial Valorization of Lignin: Prospects

and Challenges. *Bioresource Technology* **2022**, *344*, 126240. DOI: 10.1016/j.biortech.2021.126240.

(22) Kumar, A.; Biswas, B.; Kaur, R.; Krishna, B. B.; Bhaskar, T. Hydrothermal Oxidative Valorisation of Lignin into Functional Chemicals: A Review. *Bioresource Technology* **2021**, *342*, 126016. DOI: 10.1016/j.biortech.2021.126016.

(23) Davis, K.; Rover, M.; Brown, R.; Bai, X.; Wen, Z.; Jarboe, L. Recovery and Utilization of Lignin Monomers as Part of the Biorefinery Approach. *Energies* **2016**, *9* (10), 808. DOI: 10.3390/en9100808.

(24) Kalia, S., Kaith, B. S., Kaur, I., Eds.;*Cellulose Fibers: Bio- and Nano-Polymer Composites: Green Chemistry and Technology*; Springer Berlin Heidelberg: Berlin, Heidelberg, **2011**. DOI: 10.1007/978-3-642-17370-7.

(25) Pereira, P. H. F.; Rosa, M. D. F.; Cioffi, M. O. H.; Benini, K. C. C. D. C.; Milanese, A. C.; Voorwald, H. J. C.; Mulinari, D. R. Vegetal Fibers in Polymeric Composites: A Review. *Polímeros* **2015**, *25* (1), 9–22. DOI: 10.1590/0104-1428.1722.

(26) Bismarck, A.; Aranberri-Askargorta, I.; Springer, J.; Lampke, T.; Wielage, B.; Stamboulis, A.; Shenderovich, I.; Limbach, H.-H. Surface Characterization of Flax, Hemp and Cellulose Fibers; Surface Properties and the Water Uptake Behavior. *Polym. Compos.* **2002**, *23* (5), 872–894. DOI: 10.1002/pc.10485.

(27) Bourmaud, A.; Morvan, C.; Bouali, A.; Placet, V.; Perré, P.; Baley, C. Relationships between Micro-Fibrillar Angle, Mechanical Properties and Biochemical Composition of Flax Fibers. *Industrial Crops and Products* **2013**, *44*, 343–351. DOI: 10.1016/j.indcrop.2012.11.031.

(28) Park, S.; Baker, J. O.; Himmel, M. E.; Parilla, P. A.; Johnson, D. K. Cellulose Crystallinity Index: Measurement Techniques and Their Impact on Interpreting Cellulase Performance. **2010**, *3* (10). DOI: 10.1186/1754-6834-3-10.

(29) Lee, C. M.; Mittal, A.; Barnette, A. L.; Kafle, K.; Park, Y. B.; Shin, H.; Johnson, D. K.; Park, S.; Kim, S. H. Cellulose Polymorphism Study with Sum-Frequency-Generation (SFG) Vibration

Spectroscopy: Identification of Exocyclic CH2OH Conformation and Chain Orientation. *Cellulose* **2013**, *20* (3), 991–1000. DOI: 10.1007/s10570-013-9917-3.

(30) Hayashi, J.; Sufoka, A.; Ohkita, J.; Watanabe, S. The Confirmation of Existences of Cellulose IIII, IIIII, IVI, and IVII by the X-Ray Method. *J. Polym. Sci. B Polym. Lett. Ed.* **1975**, *13* (1), 23–27. DOI: 10.1002/pol.1975.130130104.

(31) Atalla, R. H.; VanderHart, D. L. Native Cellulose: A Composite of Two Distinct Crystalline Forms. *Science* **1984**, *223* (4633), 283–285. DOI: 10.1126/science.223.4633.283.

(32) Revol, J. F.; Dietrich, A.; Goring, D. A. I. Effect of Mercerization on the Crystallite Size and Crystallinity Index in Cellulose from Different Sources. *Can. J. Chem.* **1987**, *65* (8), 1724–1725. DOI: 10.1139/v87-288.

(33) Zuber, M.; Zia, K. M.; Bhatti, I. A.; Ali, Z.; Arshad, M. U.; Saif, M. J. Modification of Cellulosic Fibers by UV-Irradiation. Part II: After Treatments Effects. *International Journal of Biological Macromolecules* **2012**, *51* (5), 743–748. DOI: 10.1016/j.ijbiomac.2012.07.001.

(34) Ehrburger, P. Interface in Composite Materials. *Philosophical Transactions of the Royal Society of London. Series A, Mathematical and Physical Sciences* **1980**, *294* (1411), 495–505. DOI: 10.1098/rsta.1980.0059

(35) Eyckens, D. J.; Demir, B.; Randall, J. D.; Gengenbach, T. R.; Servinis, L.; Walsh, T. R.; Henderson, L. C. Using Molecular Entanglement as a Strategy to Enhance Carbon Fiber-Epoxy Composite Interfaces. *Composites Science and Technology* **2020**, *196*, 108225. DOI: 10.1016/j.compscitech.2020.108225.

(36) Li, H.; Lu, L.; Liu, H.; Yuan, W.; Zhang, B.; Li, J.; Li, Y.; Fu, Y. Controllable Construction and Theoretical Simulation of Silica Aerogel/Polymer Composites with Electrostatic Interaction Interfaces. *Composites Science and Technology* **2021**, *213*, 108934. DOI: 10.1016/j.compscitech.2021.108934.

(37) Wolff, D.; Geiger, S.; Ding, P.; Staehle, H. J.; Frese, C. Analysis of the Interdiffusion of Resin Monomers into Pre-Polymerized Fiber-Reinforced Composites. *Dental Materials* **2012**, *28* (5), 541–547. DOI: 10.1016/j.dental.2011.12.001.

(38) Benazzo, F.; Sodano, H. A. Evaluation of Interfacial Shear Strength Healing Efficiency between Dynamic Covalent Bond-Based Epoxy and Functionalized Fiberglass. *ACS Appl. Polym. Mater.* **2022**, *4* (4), 2925–2934. DOI: 10.1021/acsapm.2c00215.

(39) Chiang, C.-H.; Koenig, J. L. Chemical Reactions Occurring at the Interface of Epoxy Matrix and Aminosilane Coupling Agents in Fiber-reinforced Composites. *Polymer Composites* **1980**, *1* (2), 88–92. DOI: 10.1002/pc.750010207

(40) Fuentes, C. A.; Brughmans, G.; Tran, L. Q. N.; Dupont-Gillain, C.; Verpoest, I.; Van Vuure, A. W. Mechanical Behaviour and Practical Adhesion at a Bamboo Composite Interface: Physical Adhesion and Mechanical Interlocking. *Composites Science and Technology* **2015**, *109*, 40–47. DOI: 10.1016/j.compscitech.2015.01.013.

(41) Khalid, M. Y.; Imran, R.; Arif, Z. U.; Akram, N.; Arshad, H.; Al Rashid, A.; Garcia Marquez, F. P. Developments in Chemical Treatments, Manufacturing Techniques and Potential Applications of Natural-Fibers-Based Biodegradable Composites. *Coatings* **2021**, *11* (3), 293. DOI: 10.3390/coatings11030293

(42) Zimniewska, M. Hemp Fibre Properties and Processing Target Textile: A Review. *Materials* **2022**, *15* (5), 1901. DOI: 10.3390/ma15051901.

(43) Fernando, A. L.; Duarte, M. P.; Vatsanidou, A.; Alexopoulou, E. Environmental Aspects of Fiber Crops Cultivation and Use. *Industrial Crops and Products* **2015**, *68*, 105–115. DOI: 10.1016/j.indcrop.2014.10.003.

(44) Md Salim, R.; Asik, J.; Sarjadi, M. S. Chemical Functional Groups of Extractives, Cellulose and Lignin Extracted from Native Leucaena Leucocephala Bark. *Wood Sci Technol* **2021**, *55* (2), 295–313. DOI: 10.1007/s00226-020-01258-2.

(45) Mohamad Ibrahim, M. N.; Zakaria, N.; Sipaut, C. S.; Sulaiman, O.; Hashim, R. Chemical and Thermal Properties of Lignins from Oil Palm Biomass as a Substitute for Phenol in a Phenol Formaldehyde Resin Production. *Carbohydrate Polymers* **2011**, *86* (1), 112–119. DOI: 10.1016/j.carbpol.2011.04.018.

(46) Pasangulapati, V.; Ramachandriya, K. D.; Kumar, A.; Wilkins, M. R.; Jones, C. L.; Huhnke, R. L. Effects of Cellulose, Hemicellulose and Lignin on Thermochemical Conversion Characteristics of the Selected Biomass. *Bioresource Technology* **2012**, *114*, 663–669. DOI: 10.1016/j.biortech.2012.03.036.

(47) Hosoya, T.; Kawamoto, H.; Saka, S. Cellulose–Hemicellulose and Cellulose–Lignin Interactions in Wood Pyrolysis at Gasification Temperature. *Journal of Analytical and Applied Pyrolysis* **2007**, *80* (1), 118–125. DOI: 10.1016/j.jaap.2007.01.006.

(48) Dorez, G.; Ferry, L.; Sonnier, R.; Taguet, A.; Lopez-Cuesta, J.-M. Effect of Cellulose, Hemicellulose and Lignin Contents on Pyrolysis and Combustion of Natural Fibers. *Journal of Analytical and Applied Pyrolysis* **2014**, *107*, 323–331. DOI: 10.1016/j.jaap.2014.03.017.

(49) Kathirselvam, M.; Kumaravel, A.; Arthanarieswaran, V. P.; Saravanakumar, S. S. Characterization of Cellulose Fibers in Thespesia Populnea Barks: Influence of Alkali Treatment. *Carbohydrate Polymers* **2019**, *217*, 178–189. DOI: 10.1016/j.carbpol.2019.04.063.

Ruthenium complexes in biological application

Introduction

Platinum-based drugs (Figure 25) comprise some of the most important chemotherapeutics in cancer treatments, and the progenitor, cisplatin, is now widely used to treat testicular, bladder and ovarian cancers.[50]

Although cisplatin has achieved many successes in clinical use, it is not free from serious problems, including serious side effects such as nephrotoxicity, ototoxicity and neurotoxicity, with the presence of intrinsic or acquired tumour resistance.[51]

Efforts to circumvent/mitigate these toxicity and resistance issues led to the development of several approved cisplatin analogues, including carboplatin and oxaliplatin, that exhibit lower toxicity and a wider spectrum of activity compared to cisplatin.[52]

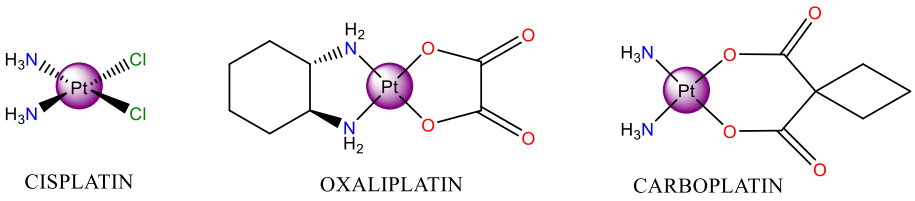

Figure 25.Graphic representation of platinum-based anticancer agents: Cisplatin, Oxaliplatin and Carboplatin.

The search for more effective and less toxic anticancer drugs has also included non-platinum-containing compounds. Among many other metals, ruthenium-based anticancer agents show great promise.[53,54]

Ruthenium Anticancer Agents

Anticancer metallodrugs based on ruthenium are among the most investigated and advanced non-platinum metallodrugs.[55]

KP1019 and NAMI-A (Figure 26) are two very important representative complexes of Ru(III) in active clinical trials. NAMI-A is very effective in killing secondary cancer cells that have spread from the primary tumour (metastasis) and shows a remarkable degree of selectivity[56], while KP1019 is the most advanced and promising ruthenium-based anticancer agent to treat primary tumours.[57,58]

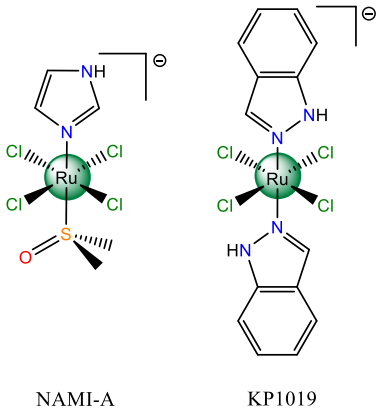

Figure 26. Graphic representation of NAMI-A (left) and KP1019 (right).

The mode of action of KP1019 and its tumor-specific activity are believed to be regulated by extensive binding to serum proteins in the blood. Then, hypoxic environment of cancer cells would be responsible for generating the more reactive Ru(II) species. They would ultimately bind to DNA or other cellular protein targets resulting in cancer cell death. It was later shown that KP1019 induces apoptosis via the mitochondrial pathway in colorectal carcinoma (SW480) cell lines.[59]

NAMI-A was the first Ru-based anticancer agent to enter clinical trials and the selection was based on the higher stability, good solubility and effective inhibition of spontaneous metastasis formation.[60–62]

It displays good disease stabilization capacity of lung carcinoma and it is also studied for combined treatment with other drugs, for example gemcitabine. NAMI-A is very promising in lower doses, on the contrary of classic clinical practices to administer the maximum tolerated doses.[62,63]

Here a representation of action mechanism of KP1019 and NAMI-A (Figure 27)

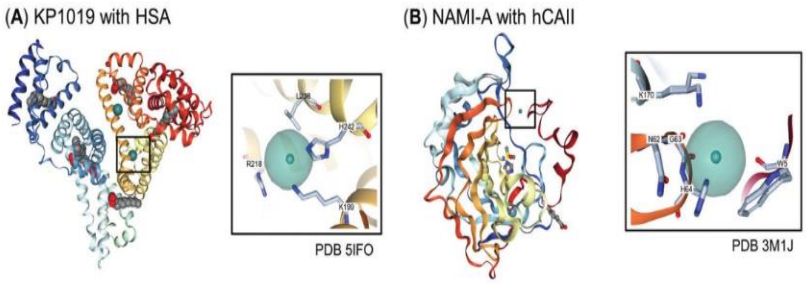

Figure 27. Molecular information derived from X-ray diffraction studies on the binding mode of ruthenium anticancer drug candidates to biomolecules: (A) KP1019 exposed to human serum albumin (HSA) and (B) NAMI-A to human carbonic anhydrase II (hCAII). Both Ru(III) compounds undergo extensive ligand exchange reactions.[55]

As previously reported and confirmed by several subsequent studies, in the process of antitumor action by KP1019 and NAMI-A, the "activation by reduction" hypothesis was confirmed, in which Ruthenium(III) is reduced to Ru(II) once it enters the more reducing environment of the tumor cells, due to the lower presence of oxygen.[64]

Therefore subsequent research had as its main objective the development of Ru(II) complexes, in which the metal center is present directly in its lower oxidation state. The first problem is related to the lability of Ru in its reduced form.[65] In the early 2000s, it was discovered that the use of η^6-arene rings was the best solution to this requirement. Now, organometallic compounds designed with the Ru center coordinating aromatic ligands are major objects of study, in the world's leading research centers working on the design and synthesis of potential anticancer agents. Professor P.J. Dyson and Professor P. Sadler are the main pioneers in this field of research.[66,67]

η^6-Arene Ru(II) complexes

In further studies, we aimed to stabilize ruthenium in the +2 oxidation state via a η^6-arene moiety, which shows ideal chemical properties as σ-,π-donor/π-acceptor. With Ru(II) stabilized in this way, the mechanism of

antitumor action depends on the ability of ligand exchange in the cancer environment.[55]

These compounds are called also “half-sandwich piano-stool” compounds for their structural characteristics which remember a sandwich without a bread slice, or a three-legged stool (Figure 28).[68,69]

The ruthenium center coordinates the aromatic moiety involving three facial sites of its octahedral coordination environment. The other three coordination sites are free to bind other donor atoms to obtain a pseudo-tetrahedral structure.

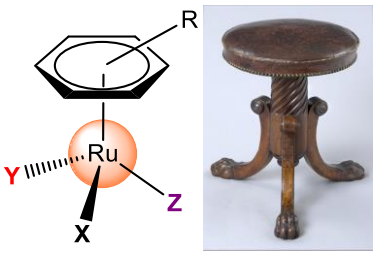

Figure 28. Half-sandwich piano-stool structure of arene-Ru(II) compounds.

In this field the most promising results have arisen from the research of professors P.J. Dyson and P. Sadler. Professor Dyson's research group at the “Ecole Polytechnique Fédérale de Lausanne”, Switzerland, has developed RAPTA (Ruthenium-Arene-PTA) complexes in which 1,3,5-triaza-7-phosphaadamantane (PTA) is coordinated to the center of Ru(II) through the P donor atom (Figure 29). Professor Sadler's research group at the University of Warwick, England, has instead developed the so-called RAED (Ruthenium-Arene-Ethylene-Diamine) complexes in which a ligand is present N,N-chelator such as ethylenediamine (Figure 29).[66]

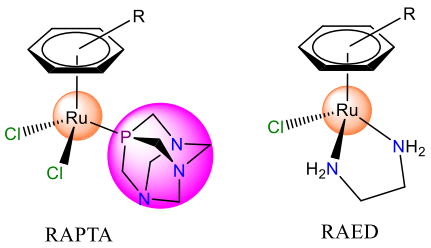

Figure 29. Graphic representation of RAPTA and RAED complexes

PTA is a sterically undemanding ligand relative to other phosphines (cone angle of 103°) and may confer a good degree of water solubility to the RAPTA complexes depending on the nature of the co-ligands.[70]

The two remaining coordination sites are usually occupied by relatively labile chloride ligands, which can exit the primary coordination sphere according to the equilibria shown in Figure 30:[71–73]

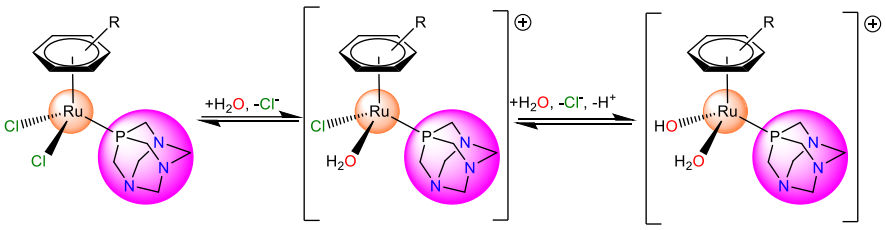

Figure 30. Graphic representation of equilibria involving RAPTA complexes in physiological environment.

Living coordination sites of chloride ligands are favored when prodrugs in the neutral form pass from the extra- to the intracellular environment where the Cl^- concentration is lower, exchanging the chloride for water and switching to the cationic form more active for subsequent exchange reactions of coordinated water with donor atoms in the target biological molecules. Generally, this happens with the two bases guanine and adenine, thus altering the functions of DNA.

Figure 31 shows the first RAPTA complexes synthetized and tested as antitumoral agents:

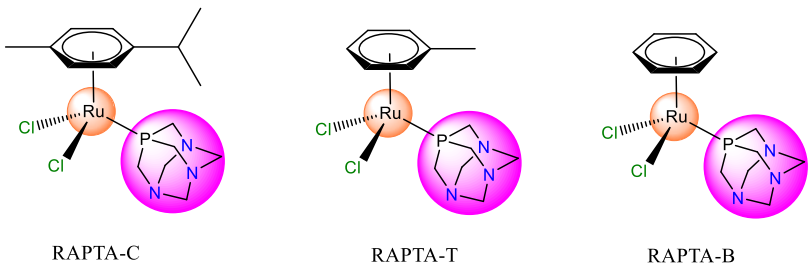

Figure 31. Graphic representation of the first RAPTA complexes tested as antitumoral agents.

RAPTA compounds have shown notable selectivity characteristics towards tumor cells, both for the primary tumor and for metastases.

In particular, the RAPTA-C complex is capable of damaging cellular DNA at pH lower than 6.5 but not at physiological pH 7.5. This indicates that RAPTA-C can be used to selectively damage DNA in diseased cells.[66]

The RAPTA-T complex showed very promising antitumor activity, providing excellent cytotoxicity against several tumor cell lines in the absence of toxicity towards non-tumour cell lines.[74]

The antimetastatic properties of RAPTA-T were investigated in more detail, showing the efficacy of this compound to hinder the formation of metastases.[75]

The series of RAED compounds, which were first reported in 2001, are able to coordinate to DNA through the N7 of guanine residues and, when bearing an extended arene ligand such as biphenyl, dihydroanthracene, and tetrahydro anthracene, may concomitantly intercalate DNA.

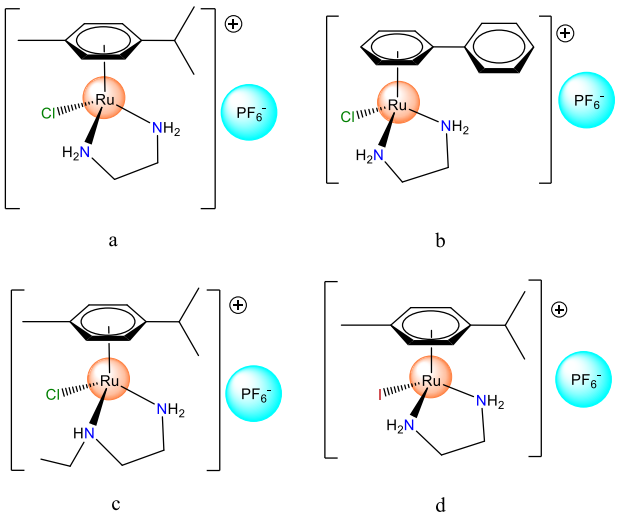

Figure 32. Graphic representation of the first RAED complexes reported in 2001.[67]

The RAED complexes shown in Figure 32 demonstrated very high cytotoxicity towards human ovarian cancer cells with IC_{50} values comparable to that of carboplatin.[67]

The results obtained from the study of these piano-stool half-sandwich ruthenium complexes have encouraged the development of numerous lines of research, which include the synthesis and characterization of new

ligands capable of coordinating the Ru(II) center, and capable to confer toxicity and selectivity towards diseased tissues. The Camerino research group of Profs. Fabio Marchetti, Riccardo Pettinari, Corrado Di Nicola and Claudio Pettinari, where I carried out my doctoral thesis, has contributed in recent years to the development of this sector with the synthesis of numerous new arene Ru(II) complexes, focusing on focus on particular organic ligands from natural sources, themselves having an interesting biological activity: curcumins and acylpyrazolones. Acylpyrazolones and their use in the synthesis of new Ru(II) complexes with potential anti-tumor activity are the objective of this doctoral thesis.

Pyrazolones and Acylpyrazolones

Pyrazole is a five-membered heterocycle, containing two adjacent nitrogen atoms. It is considered a very important ligand in coordination chemistry because it can form a variety of metal coordination complexes with several main groups, transition and lanthanoid cations, providing varying coordination geometries. Pyrazole finds a very large field of application,[76] and in particular two of its derivatives attract the researchers' attention for medical and pharmacological applications: pyrazolones, in which a carbonyl is introduced in C-5 position, and acylpyrazolones obtained from the acylation of pyrazolone ring in C-4 position (Figure 33).

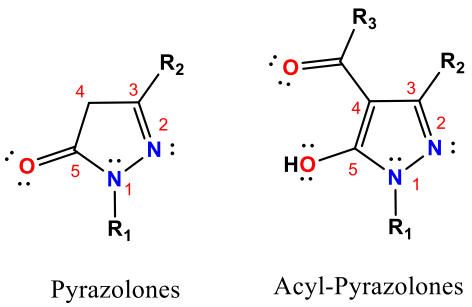

Figure 33. Graphic representation of pyrazolones and acylpyrazolones.

3-Methyl-5-pyrazolone is an interesting synthon for the synthesis of numerous molecules with potential applications in pharmaceutical

chemistry[77,78] and one of its derivatives with a phenyl group condensed in N1 was recently approved by the Food and Drug Administration to treat amyotrophic lateral sclerosis (ALS).[79–81]

It is the 3-methyl-1-phenyl-5-pyrazolone, also called Edaravone and commercially known as Radicava® or Radicut, which is the most effective in halting ALS progression during early stages.[81]

It has been seen that starting from this molecule, it is possible to synthesize countless organic compounds through a simple acylation in the C-4 position with acyl chlorides or anhydrides (Figure 34). The compounds obtained can be used as O,O- donor ligands in their deprotonated form.

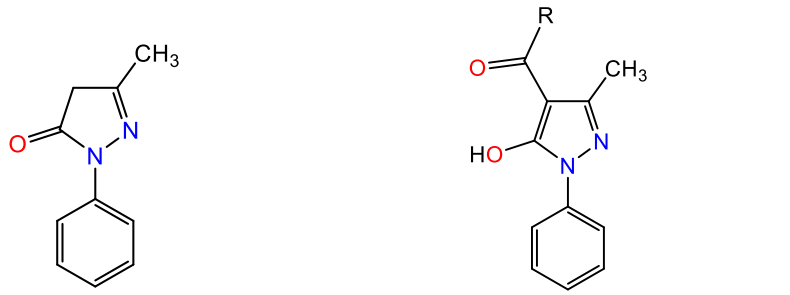

3-methyl-1-phenyl-5-pyrazolone 3-methyl-1-phenyl-4-acyl-5-pyrazolone

Figure 34. Graphic representation of Edaravone (left) and its acylpyrazolones (right).

The synthesis of compounds analogous to Edaravone and their conversion into acyl pyrazolones, and their use in the synthesis of new potential antitumor arene-Ru(II) drugs has been the subject of study by our research group for many years, demonstrating that varying the nature of the substituents around the main skeleton of the ligand brought about changes in the chemical-physical characteristics of the obtained complexes, thus altering their cytotoxic capabilities.[82]

Figure 35 displays some examples of neutral and ionic arene-Ru(II) complexes with acylpyrazolone ligands previously reported and investigated as antitumor compounds:

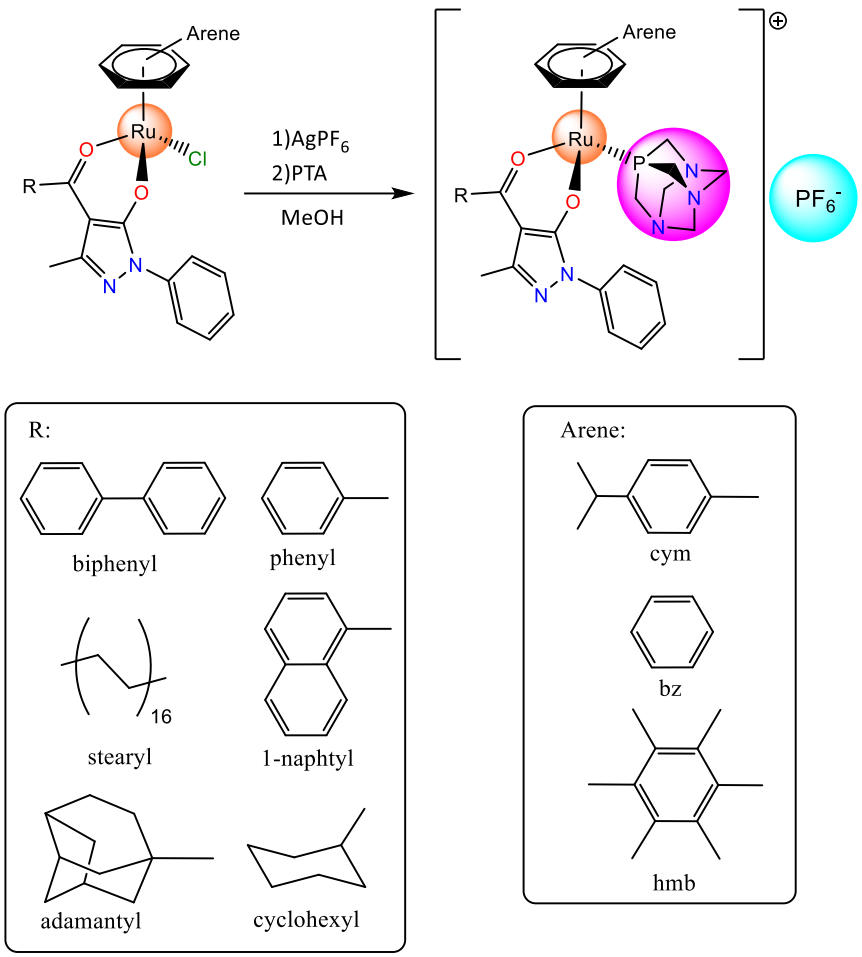

Figure 35. schematic representation of arene-Ru(II) complexes with acylpyrazolones arising Edaravone.[82]

In 2004 the research group of Professor Marchetti and collaborators reported the synthesis, characterization and silver(I) coordination mode of an acylpyrazolone with bearing a pyridine linked to N1 of pyrazole (Figure 36). This ligand in its deprotonated form shown the ability to coordinate two metal centers through *N,N*- and *O,O*- coordination. The precursor of this ligand is 1-(2-pyridyl)-3-methyl-5-pyrazolone (HL^{py}), an analogue of Edaravone but, instead of the phenyl, there is a condensed pyridine ring to N1. The final pro-ligand was 3-methyl-1-(pyridin-2-yl)-4-trifluoroacetyl-5-pyrazolone ($HQ^{py,CF3}$), named Janus ligand like the roman God of entrances, doorways, gateways, thresholds, and beginnings (Figure 37).[83]

Here the reaction scheme of synthesis of HL^{py} and $HQ^{py,CF3}$:

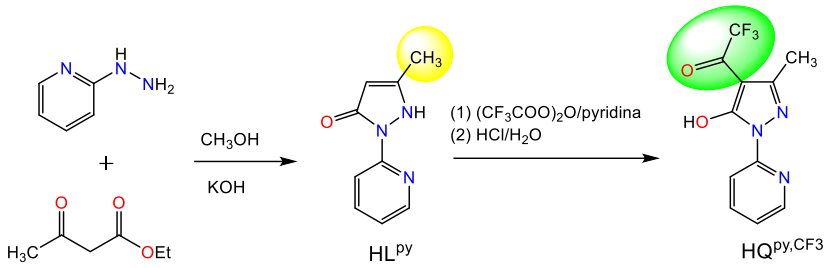

Figure 36. Graphic representation of the reaction scheme for the HL^{py} and $HQ^{py,CF3}$ synthesis.[83]

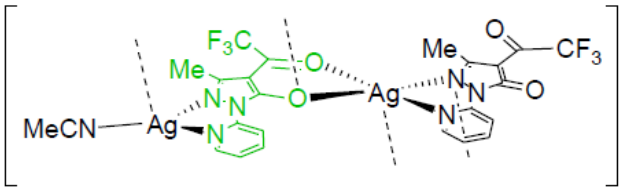

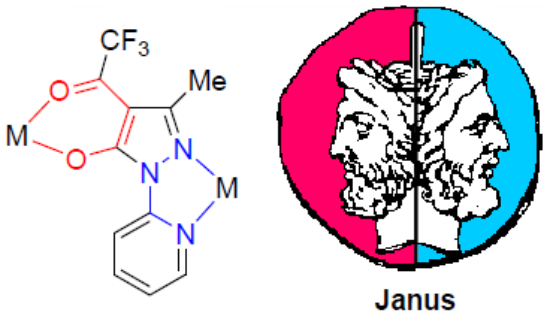

Figure 37. Coordination mode of Janus ligand.[83]

After some years, the coordination ability of $HQ^{py,CF3}$ and HL^{py} toward arene-Ru(II) fragments was explored, and in 2021 a paper was published reporting new potential arene-Ru(II) anticancer agents obtained by the reaction of arene-Ru(II) dimers and the deprotonated form of Janus ligand and its precursor (Figure 38).[84]

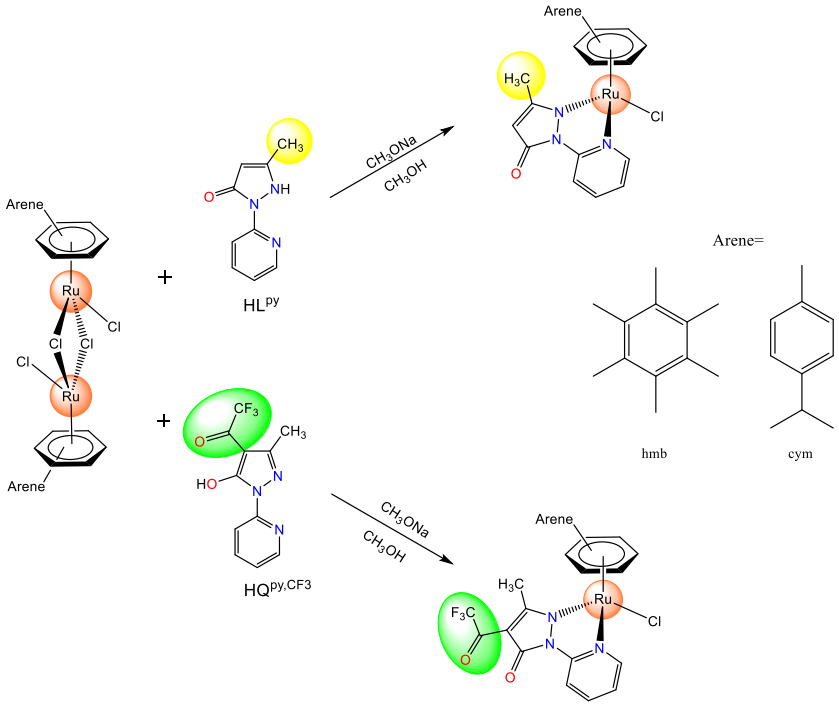

Figure 38. Reaction scheme of Arene-Ru(II) complexes with HL^{py} and HQ^{py,CF3}

It was confirmed by X-Ray characterization and DFT study (Figure 39) that the most favorite coordination action of these two ligands is trough *N,N*- donor atoms, that is different to other acylpyrazolones with a phenyl condensed to N1 of pyrazolone moiety, where coordination to the Ru(II) center occurs through the oxygen atoms. This result can be explained considering the soft-borderline nature of Ru(II) according to the HSAB theory, and the softer nature of nitrogen with respect to oxygen.

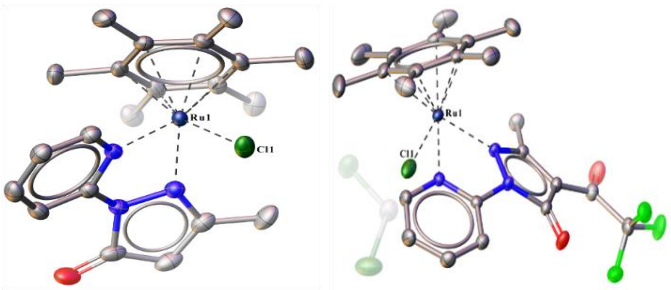

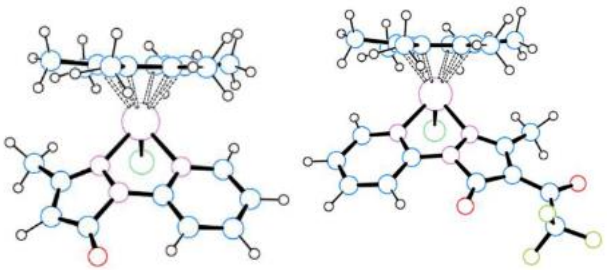

Figure 39. X-Ray and DFT structures as confirmation of N,N'-coordination mode of HL^{py} and $HQ^{py,CF3}$

Anticancer tests on A2780, A2780cisR tumor cell lines and non-tumoral cell line HEK293T of free pro-ligands and Ru(II) complexes were compared with IC_{50} of Cisplatin and RAPTA-C, giving interesting results. Based on these interesting findings on structures and biological activities, the work continued during my PhD period with the synthesis of ionic analogues of RAPTA with the aim of increasing water solubility and improving biological activities. Furthermore, another ligand previously synthesized by others was introduced,[85–88] the 5-phenyl-2-(pyridin-2-yl)-2,4-dihydro-3H-pyrazol-3-one signed $HL^{py,ph}$, of which it was never explored the coordination abilities to Ru(II) center. It was recently published the work titled "Steric and Electronic Effects Responsible for N,O- or N,N-Chelating Coordination of Pyrazolones Containing a Pyridine Ring in Ruthenium Arene Systems" reporting the results that we are going to explain in detail.

Experimental

Materials and Methods

Solvents were used as provided or distilled using standard methods. All chemicals were purchased from Aldrich (Milwaukee) and used as received. The dimers [Ru(arene)-Cl_2]$_2$ (arene is or p-cymene (cym) or hexamethylbenzene (hmb)) were acquired from Aldrich. The ligands $HL^{py,me}$ and $HQ^{py,CF3}$ were synthesized by a procedure similar to that previously reported.[84]

IR spectra were recorded on a PerkinElmer Frontier FT-IR instrument. ^{1}H, ^{13}C, ^{31}P NMR spectra were recorded on a 500 Bruker Ascen instrument operating at room temperature relative to TMS. Positive ion electrospray mass spectra were obtained on a Series 1100 MSI detector HP spectrometer, using methanol and acetonitrile as solvent for all complexes 1−8. Solutions (3 mg/mL) for electrospray ionization mass spectrometry (ESI-MS) were prepared using reagent-grade methanol. Masses and intensities were compared to those calculated using IsoPro Isotopic Abundance Simulator, version 2.1.28. Melting points are uncorrected and were recorded on a STMP3 Stuart scientific instrument and on a capillary apparatus. Samples for microanalysis were dried in vacuo to constant weight (20 °C, ca. 0.1 Torr) and analyzed on a Fisons Instruments 1108 CHNS-O elemental analyzer.

X-ray Crystallography

The difraction data of $HL^{py,ph}$ and 3 were obtained, at 140 K, using Cu Kα radiation. Appropriate crystals of $HL^{py,ph}$ and 3 were selected and located on an XtaLAB Synergy R, DW system, HyPix-Arc 150 difractometer. The data sets were reduced and corrected for absorption, with the help of a set of faces enclosing the crystals as snugly as possible, with the latest available version of $CrysAlis^{Pro}$.[89]

The solution and refinement of the structures were performed by the latest available version of ShelXT [90] and ShelXL[91] using Olex 2−1.5 [92,93] as the graphical interface. All non-hydrogen atoms were refined anisotropically using full-matrix least-squares based on $|F|^2$. The hydrogen atoms were placed at calculated positions employing the "riding" model, where each H atom was assigned a fixed isotropic displacement parameter with a value equal to 1.2 U_{eq} of its parent C atom. In $HL^{py,ph}$, the hydrogen atom bound to O1 was found in a difference map and refined freely.

Computational Details

The electronic structures and geometries of the $HL^{py,ph}$ proligand and the $[L^{py,ph}]-$ anion, their tautomers, rotamers and ruthenium complexes 1−8 and some of their isomers were investigated by using density functional theory at the B3LYP level.[94,95]

For the proligand, tautomers, rotamers and its anion the 6-311+G** basis set was used for the optimization, while for Ru compounds the optimization was carried out using LANL2DZ,[96]

for the Ru atom and the 6-31G* basis set for the remaining atoms. Molecular geometries were optimized without symmetry restrictions. Frequency calculations were carried out at the same level of theory to identify all the stationary points as minima (zero imaginary frequencies) and to provide the thermal correction to free energies at 298.15 K and 1 atm. The GIAO method was used for the NMR calculations ^{1}H, ^{13}C, and ^{15}N NMR isotropic shielding tensors) which were carried out at the 6-311+G(2d,p) level of theory. The computed IR spectra were scaled by a factor of 0.96.[97,98]

The DFT calculations were executed using the Gaussian 09 program package[99]

Cytotoxicity Tests on A2780, A2780cis, and HEK293T Cell Lines.

The human ovarian carcinoma cell line and its Cisplatin resistant form, A2780 and A2780cis, were purchased from the European Collection of Cell Cultures (ECACC, United Kingdom). The human embryonic kidney 293T cell line (HEK293T) was kindly provided by the biological screening facility (EPFL, Switzerland). Fetal bovine serum (FBS) was obtained from Sigma, Switzerland. RPMI 1640 GlutaMAX and DMEM GlutaMAX media were purchased from Life Technologies. The cells were cultured in RPMI 1640 GlutaMAX supplemented for the ovarian cancer cell lines A2780 and A2780cis and in DMEM GlutaMAX supplemented for HEK293T with 10% heat-inactivated FBS at 37 °C and CO_2 (5%). To uphold Cisplatin resistance, the A2780cis cell line was routinely treated with Cisplatin at a final concentration of 2 μM in the media. MTT (3-(4,5-dimethyl-2- thiazolyl)-2,5-diphenyl-2H-tetrazolium bromide) assay was used to evaluate the cytotoxicity of the compounds. Stock solutions were prepared in DMSO and sequentially diluted in cell culture grade water to obtain a concentration range of 0−1 mM. Ten μL aliquots of these prepared compound solutions were added in triplicates to a 96-well plate to which 90 μL of the cell suspension (approximately 1.4 × 104 cells/well) were added (final volume 100 μL/concentrations range 0−100 μM). Cisplatin and RAPTA-C were used as positive (0−100 μM) and negative (0−100 μM) controls, respectively, and the plates were incubated for 72 h. Ten microliters of an MTT solution prepared at a concentration of 5 mg/mL in Dulbecco's phosphate buffered saline (DPBS) was added to the cells, and the plates were incubated for additional 4 h. The culture media was carefully aspirated to preserve the purple formazan crystals that were dissolved in DMSO (100 μL/well). The absorbance of the resulting solutions, which is directly proportional to the number of surviving cells, was measured at 590 nm using SpectroMax M5e microplate reader and the data was analyzed with GraphPad Prism software (version 9.3.1). The reported IC_{50} values are based on the means of three independent experiments, each comprising three tests per concentration level.

Synthesis of Proligand $HL^{py,ph}$ and Complexes 1−8

Proligand $HL^{py,ph}$

Reaction in Figure 40:

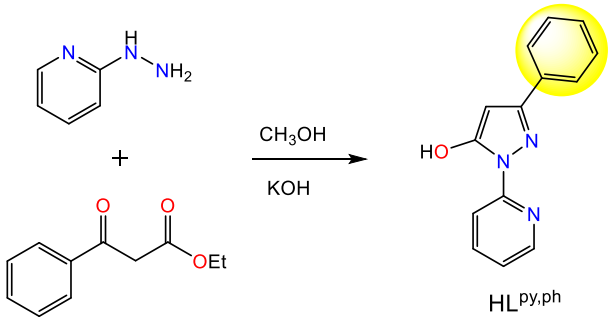

Figure 40. Reaction Scheme of Proligand $HL^{py,ph}$ synthesis.

It was synthesized by reacting equimolar amounts of 2-hydrazineylpyridine (2.29 g, 21 mmol), and ethyl 3-oxo-3-phenyl-propanoate (4.04 g, 21 mmol) at room temperature. A solution of KOH (87.9%) (100 mg, 1.57 mmol) in methanol (about 20 mL) was added to the mixture. The initial violet mixture was stirred 1 h at room temperature, changing to dark blue. The solution was dried on a rotavapor until an oil was obtained, which was dissolved in hot acetonitrile. The final product crystallized by slow cooling and evaporation (4.52 g, 0.019 mol, yield 90.7%). It is a dark blue solid opaque crystal, highly soluble in alcohols, DMSO, DMF, acetone, acetonitrile, and chlorinate solvents Anal. Calcd for $C_{14}H_{11}N_3O$ (MW: 237 g/mol): C, 70.87; H, 4.67; N, 17.71%. Found: C, 70.51; H, 4.58; N, 17.83%. mp 121−122 °C. IR (cm−1): 3056w ν(C−H aromatics), 1656m ν(C=O), 1624w ν(C=N), 1596m and 1579m ν(C=C), 1537w, 1489m, 1469s, 1456s, 1441s, 1385m, 1330m, 1296m, 1280m, 999m, 943m, 840m, 814m, 783vs, 749vs, 691s, 655s, 677m, 652m, 590w, 523m, 441s, 407m, 326m, 266w, 194w, 151vs. ^{1}H NMR (500 MHz, $CDCl_3$, 298 K): δ 5.98s (1H, C4−H of $HL^{py,ph}$), 7.17t (1H, $^3J_{(H-H)}$ = 7.5 Hz, C9−H of $HL^{py,ph}$), 7.38t (1H, $^3J_{(H-H)}$ = 7.2 Hz, C14−H of $HL^{py,ph}$), 7.45t (2H, $^3J_{(H-H)}$ = 7.5 Hz, C13,13′-H of $HL^{py,ph}$), 7.90m (3H, C12,12′-H and

C8−H of $HL^{py,ph}$), 8.08d (1H, $^{3}J_{(H-H)}$ = 8.4 Hz, C7−H of $HL^{py,ph}$), 8.30d (1H, $^{3}J_{(H-H)}$ = 4.6 Hz, C10−H of $HL^{py,ph}$), 12.84s (1H, OH of $HL^{py,ph}$). ^{13}C NMR ($CDCl_3$, 298 K): δ 8.8 (C4 of $HL^{py,ph}$), 112.3 (C7 of $HL^{py,ph}$), 119.9 (C9 of $HL^{py,ph}$), 125.9 (C13−13′ of $HL^{py,ph}$), 128.6 (C14 of $HL^{py,ph}$), 128.6 (C12−12′ of $HL^{py,ph}$), 133.0 (C11 of $HL^{py,ph}$), 140.0 (C8 of $HL^{py,ph}$), 145.1 (C10 of $HL^{py,ph}$), 152.7 (C3 of $HL^{py,ph}$), 154.5 (C6 of $HL^{py,ph}$), 157.3 (C5 of $HL^{py,ph}$). {1H−15N}-g-HMBC NMR ($CDCl_3$, 51 MHz, $^{3}J_{(N-H)}$ = 3 Hz, 298 K): δN 194.5 (N2 of $HL^{py,ph}$), 251.9 (Npy of $HL^{py,ph}$), 263.1 (N1 of $HL^{py,ph}$). ESI-MS(−) (CH_3OH) (m/z, relative intensity%): 236 [100] $[Lpy,ph]^{-}$.

[Ru(cym)($L^{py,ph}$)Cl] ***(1)***

Reaction in Figure 41:

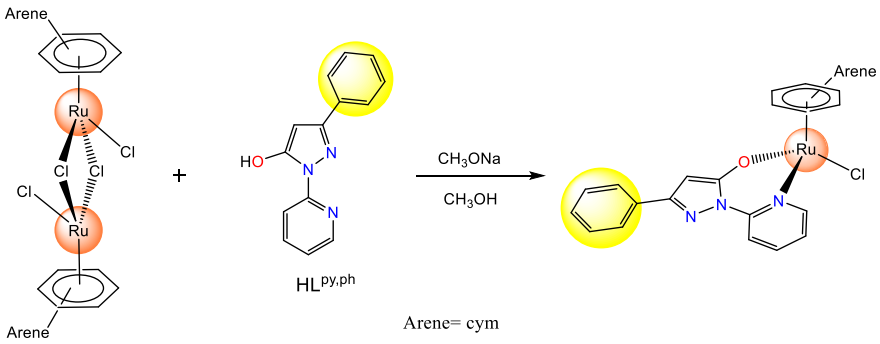

Figure 41. Reaction scheme of Complex 1 synthesis.

$HL^{py,ph}$ (222.7 mg, 0.94 mmol) was dissolved in 20 ml of methanol, KOH (87.9 %) was added (65.1 mg, 0.94 mmol) and the mixture was stirred 1 h at room temperature. Then a methanol solution (30 ml) of $[Ru(cym)Cl_2]_2$ (287.8 mg, 0.47 mmol) was slowly added affording a dark green mixture, which was left under stirring at room temperature overnight. The solvent was removed by rotary evaporator, and the crude solid was dissolved in 30 ml of dichloromethane. The mixture was filtered to remove the by-product KCl, and the volume of filtrate reduced to ca. 4 ml. Then, 30 mL of n-hexane were added affording a dark green precipitate, which was filtered off and dried to constant weight (261.4 mg, 0.51 mmol, yield 54.8%). It is soluble in alcohols, DMSO, DMF, acetone, acetonitrile, and chlorinated

solvents. Anal. Calcd for $C_{24}H_{24}ClN_3ORu$ (mw: 508): C, 56.86; H, 4.77; N, 8.29%. Found: C, 56.59; H, 4.64; N, 8.19%. Λ_m (DMSO, 295 K, $9.8 \cdot 10^{-4}$ mol/L): 2.2 S cm^2 mol^{-1}. It decomposes gradually with temperature, starting from about 234°C. IR (cm^{-1}): 3419vb (O-H···O, hydrogen bond), 3058w ν(C-H aromatics), 2965w ν(C-H aliphatic), 1635vs ν(C=O), 1483vs and 1461vs δ(C-H), 1370s ν(C-N), 1189w, 1145w, 1091w, 1029w, 940m, 872m, 769vs, 740s, 662s, 520m ν(Ru-N), 450m, 440m ν(Ru-O), 403m, 287vs ν(Ru-Cl), 246vs, 228s, 202m. ^{1}H NMR (500 MHz, CD_3CN, 298 K): δ, 0.94d, 0.97d (6H, $^3J_{(H—H)}$ = 6.9 Hz, CH_3-C_6H_4-CH-(CH_3)$_2$ of cym), 2.17s (3H, CH_3-C_6H_4-CH-(CH_3)$_2$ of cym), 2.32hept (1H, $^3J_{(H—H)}$ = 6.9 Hz, CH_3-C_6H_4-C*H*-(CH_3)$_2$ of cym), 4.76d, 4.88d (2H, $^3J_{(H—H)}$ = 6.0 Hz, CH_3-C_6H_4-CH-(CH_3)$_2$ of cym), 5.14s (1H, C4-H of $L^{py,ph}$), 5.17d, 5.43d (2H, $^3J_{(H—H)}$ = 6.0 Hz, CH_3-C_6H_4-CH-(CH_3)$_2$ of cym), 5.14s (1H, C4-H of $L^{py,ph}$), 7.16ddd (1H, $^3J_{(H—H)}$ = 7.2, 5.8 Hz, $^4J_{(H—H)}$= 1.3 Hz, C9-H of $L^{py,ph}$), 7.58m (3H, C13,13',14-H of $L^{py,ph}$), 7.92ddd (1H, $^3J_{(H—H)}$ = 8.7, 7.3 Hz, $^4J_{(H—H)}$= 1.5 Hz, C8-H of $L^{py,ph}$), 7.99dd (2H, $^3J_{(H—H)}$ = 7.9 Hz, $^4J_{(H—H)}$= 1.7 Hz, C12,12'-H of $L^{py,ph}$), 8.61dd (1H, $^3J_{(H—H)}$ = 8.5 Hz, $^4J_{(H—H)}$ = 1.3 Hz, C7-H of $L^{py,ph}$), 8.86dd (1H, $^3J_{(H—H)}$ = 5.8 Hz, $^4J_{(H—H)}$= 1.6 Hz, C10-H of $L^{py,ph}$). $^{13}C\{^1H\}$ NMR (500 MHz, CD_3CN, 298 K): δ, 18.0 ((CH_3-C_6H_4-CH-(CH_3)$_2$ of cym), 20.8, 21.4 ((CH_3-C_6H_4-CH-(CH_3)$_2$), 81.8, 83.0, 84.3, 84.5 (CH_3-C_6H_4-CH-(CH_3)$_2$ of cym), 88.0 (C4 of $L^{py,ph}$), 101.9, 103.1 (CH_3-C_6H_4-CH-(CH_3)$_2$ of cym), 111.1 (C7 of $L^{py,ph}$), 119.4 (C9 of $L^{py,ph}$), 128.4 (C13,13' oh $L^{py,ph}$), 129.2 (C14,12,12' of $L^{py,ph}$), 135.0 (C11 oh $L^{py,ph}$), 140.0 (C8 of $L^{py,ph}$), 150.7 (C6 of $L^{py,ph}$), 152.6 (C10 of $L^{py,ph}$), 161.5 (C3 of $L^{py,ph}$), 165.3 (C5 of $L^{py,ph}$). $\{^1H$-$^{15}N\}$-g-HMBC NMR (**(**CD_3CN, 51 MHz, $^3J_{(N—H)}$= 3 Hz, at 298 K): δ_N, 157.0 (N2 of L^{py}), 202.9 (N_{py} of L^{py}), 205.3 (N1 of L^{py}). ESI-MS (+) (CH_3CN) (m/z, relative intensity %): 472 [100] $[Ru(hmb)L^{py,ph}]^+$.

[Ru(hmb)($L^{py,ph}$)Cl] ***(2)***

Reaction in Figure 42:

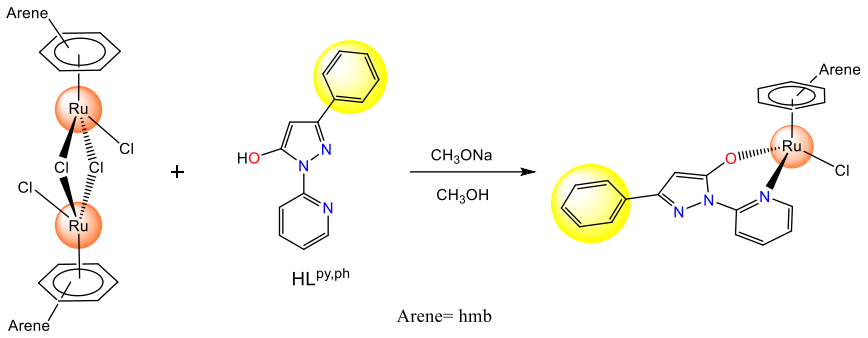

Figure 42.Reaction scheme of Complex 2 synthesis

Complex **2** was prepared using a method similar to that of **1**, using $HL^{py,ph}$ (184.9 mg, 0.78 mmol), KOH (87.9 %) (49 mg, 0.78 mmol), and $[Ru(hmb)Cl_2]_2$ (260.7 mg, 0.39 mmol). It was isolated as an orange powder (310 mg, 0.58 mmols, yield 74.3 %). It is slightly soluble in alcohols and acetonitrile and soluble in DMSO, DMF, and chlorinated solvents. Anal. Calcd for $C_{26}H_{28}ClN_3ORu$ (mw: 535): C, 58.37; H, 5.28; N, 7.85%. Found: C, 58.26; H, 5.27; N, 7.72%. Λ_m (DMSO, 296 K, $8.3 \cdot 10^{-4}$ mol/L): 2.8 S cm^2 mol^{-1}. It decomposes gradually with temperature starting from about 295°C. IR (cm^{-1}): 3105w νs(C-H aromatics), 3054w νa(C-H aromatics), 2921w ν(C-H aliphatic), 1633vs ν(C=O), 1593s ν(C=C), 1578m ν(C=N), 1558m, 1485vs and 1405m δ(C-H), 1356s ν(C-N), 1289m, 1235w, 1183w, 1147w, 1087w, 1075w, 1025m, 992m, 762vs, 749s, 676w, 666s, 627m, 529m, 507m ν(Ru-N), 473m, 455m, 439m ν(Ru-O), 401m, 355w, 304s, 291s ν(Ru-Cl), 264m, 227m, 202s. ^{1}H NMR (500 MHz, $CDCl_3$, 298K) δ, 2.00s (18H, $C_6(CH_3)$ of hmb), 5.86s (1H, C4-H of $L^{py,ph}$), 7.13ddd (1H, $^3J_{(H\text{-}H)}$= 7.3, 5.8 Hz; $^4J_{(H—H)}$= 1.5 Hz, C9-H of $L^{py,ph}$), 7.37m (1H, C14-H of $L^{py,ph}$), 7.44dd (2H, $^3J_{(H—H)}$= 8.3, 6.9 Hz, C13,13'-H of $L^{py,ph}$), 7.80ddd (1H, $^3J_{(H—H)}$= 8.7, 7.1 Hz, $^4J_{(H—H)}$= 1.8 Hz, C8-H of $L^{py,ph}$), 7.90m (3H, $^3J_{(H\text{-}H)}$= 8.3, 1.6 Hz, C12,12'-H of $L^{py,ph}$ and C7-H of $L^{py,ph}$), 8.47dd (1H, $^3J_{(H\text{-}H)}$= 5.9 Hz, $^4J_{(H—H)}$= 1.8 Hz, C10-H of $L^{py,ph}$). ^{13}C-NMR (500 MHz, $CDCl_3$, 298K): δ 15.2 (CH_3 of hmb), 87.2 (C4 of $L^{py,ph}$), 91.4 (C_{arom} of

hmb), 115.3 (C7 of $L^{py,ph}$), 119.8 (C9 of $L^{py,ph}$), 125.8 (C12-12' of $L^{py,ph}$), 128.3 (C14 of $L^{py,ph}$) 128.4 (C13-13' of $L^{py,ph}$), 133.9 (C11 of $L^{py,ph}$), 139.1 (C8 of $L^{py,ph}$), 150.7 (C6 of $L^{py,ph}$), 152.0 (C10 of $L^{py,ph}$), 155.3 (C3 of $L^{py,ph}$), 163.7 (C5 of $L^{py,ph}$). {^{1}H-^{15}N}-g-HMBC NMR ($CDCl_3$, 51 MHz, $^{3}J_{(N—H)}$ = 3 Hz, 298K): δ_N, 206.1 (N1 of $L^{py,ph}$), N_{py} and N2 of $L^{py,ph}$ not observed. ESI-MS (+) (CH_3CN) (m/z, relative intensity %): 500 [100] $[Ru(hmb)L^{py,ph}]^{+}$.

[Ru(cym)($L^{py,ph}$)PTA]BF_4 ***(3)***

Reaction in Figure 43:

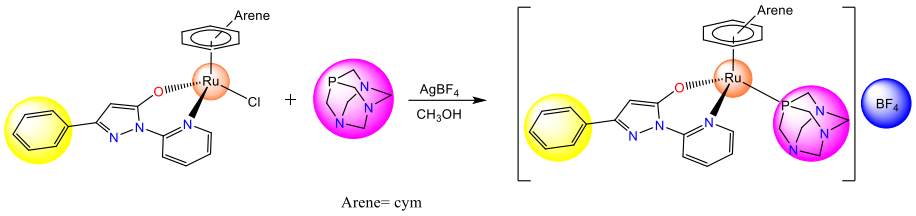

Figure 43. Reaction scheme of Complex 3 synthesis.

Complex **1** (107.5 mg, 0.21 mmol) was dissolved in 30 ml of methanol and 3 mL of an aqueous solution of $AgBF_4$ (41.7 mg, 0.21 mmol) were added. PTA (0.034 mg, 0.21 mmol) was then added, and the mixture stirred 2 h at room temperature. The initial brown-green solution turned to pale green within time. After removal of the by-product AgCl by filtration, the volume of filtrate was reduced to ca. 4 ml and Et_2O (about 30 mL) was added, with formation of a dark green precipitate, which was identified as complex **3** (101 mg, 0.14 mmol, yield 67 %). It is very soluble in alcohols, acetonitrile, DMSO, DMF and acetone, and slightly soluble in water and chlorinated solvents. Anal. Calcd for $C_{30}H_{36}BF_4N_6OPRu$ (mw: 715): C, 50.36; H, 5.07; N, 11.75%. Found: C, 50.13; H, 5.17; N, 11.65%. Λ_m (DMSO, 294 K, $9.9.10^{-4}$ mol/L): 23.4 S cm^2 mol^{-1}. It decomposes gradually with temperature starting from about 235°C. IR (cm^{-3}): 3074w ν(C-H aromatics), 2924w ν(C-H aliphatic), 1626s ν(C=O), 1483s, 1447s, 1373s, 1054vs and 1034vs ν(BF_4), 973s, 947s, 803m, 742s, 698s, 662m,

581vs, 519s, 476s, 451s, 389s, 336m, 305m, 229m, 203m. ^{1}H NMR (500 MHz, CD_3CN, 298K): δ, 0.82d, 0.94d (6H, $^{3}J_{(H—H)}$= 6.9 Hz, CH_3-C_6H_4-CH-(CH_3)$_2$ of cym), 2.22s (3H, CH_3-C_6H_4-CH-(CH_3)$_2$), 2.33hept (1H, $^{3}J_{(H—H)}$ = 6.9 Hz, CH_3-C_6H_4-CH-(CH_3)$_2$ of cym), 4.01m (6H, (P-CH_2-N)$_3$ of PTA phosphine), 4.45s (6H, (N-CH_2-N)$_3$ of PTA phosphine), 4.90d, 5.16d (2H, $^{3}J_{(H—H)}$= 6.2 Hz, CH_3-C_6H_4-CH-(CH_3)$_2$ of cym), 5.22s (1H, C4-H of $L^{py,ph}$), 5.69d, 5.72d (2H, $^{3}J_{(H—H)}$= 6.2 Hz, CH_3-C_6H_4-CH-(CH_3)$_2$ of cym), 7.25ddd (1H, $^{3}J_{(H—H)}$ = 7.3, 5.9 Hz, $^{4}J_{(H—H)}$= 1.4 Hz, C9-H of $L^{py,ph}$), 7.57m (2H, C13,13'-H of $L^{py,ph}$), 7.64m (1H, C14-H of $L^{py,ph}$), 7.68m (2H, C12,12'-H of $L^{py,ph}$), 8.10ddd (1H, $^{3}J_{(H—H)}$= 8.8, 7.2 Hz, $^{4}J_{(H—H)}$= 1.6 Hz, C8-H of $L^{py,ph}$), 8.40dd (1H, $^{3}J_{(H—H)}$= 6.0, $^{4}J_{(H—H)}$= 1.5 Hz, C10-H of $L^{py,ph}$), 8.78dd (1H, $^{3}J_{(H—H)}$= 8.7, $^{4}J_{(H—H)}$= 1.4 Hz, C7-H of $L^{py,ph}$). ^{13}C-NMR (500 Hz, 298 K, CD_3CN): δ, 18.7 (CH_3-C_6H_4-CH-(CH_3)$_2$ of cym), 20.4, 21.5 (CH_3-C_6H_4-CH-(CH_3)$_2$ of cym), 30.9 (CH_3-C_6H_4-CH-(CH_3)$_2$ of cym), 50.7d ($^{1}J_{(P—C)}$= 13.6 Hz, (P-CH_2-N)$_3$ of PTA phosphine), 72.1 ($^{3}J_{(P—C)}$= 7.5 Hz, (N-CH_2-N)$_3$ of PTA phosphine), 86.6, 87.6, 89.5 (CH_3-C_6H_4-CH-(CH_3)$_2$ of cym), 89.8 (C4 of $L^{py,ph}$), 90.6, 103.4 (CH_3-C_6H_4-CH-(CH_3)$_2$ of cym), 112.4 (C7 of $L^{py,ph}$), 120.4 (CH_3-C_6H_4-CH-(CH_3)$_2$ of cym), 121.0 (C9 of $L^{py,ph}$), 128.3 (C13,13' of $L^{py,ph}$), 129.0 (C12,12' of $L^{py,ph}$), 129.8 (C14 of $L^{py,ph}$), 133.9 (C11 of cym), 141.5 (C8 of cym), 151.3 (C3 of $L^{py,ph}$), 153.3d ($^{1}J_{(N—C)}$= 5.6 Hz C10 of $L^{py,ph}$), 164.1 (C6 of $L^{py,ph}$), 165.5 (C5 of $L^{py,ph}$). ^{31}P-NMR (500 Hz, 298K, CD_3CN): δ, -37.7. {^{1}H-^{15}N}-g-HMBC NMR in **(**CD_3CN, 51 MHz, $^{3}J_{(N—H)}$ = 3 Hz, at 298 K): δ_N, 42.5 (N_{PTA}), 131.5 (N2 of $L^{py,ph}$), 176.5 (N_{py} of $L^{py,ph}$), 206.8 (N1 of $L^{py,ph}$). ESI-MS (+) (CH_3CN) (m/z, relative intensity %): 472 [100] $[Ru(cym)L^{py,ph}]^{+}$, 629 [91] $[Ru(cym)(L^{py,ph})PTA]^{+}$.

[Ru(hmb)($L^{py,ph}$)PTA]BF_4 ***(4)***

Reaction in Figure 44:

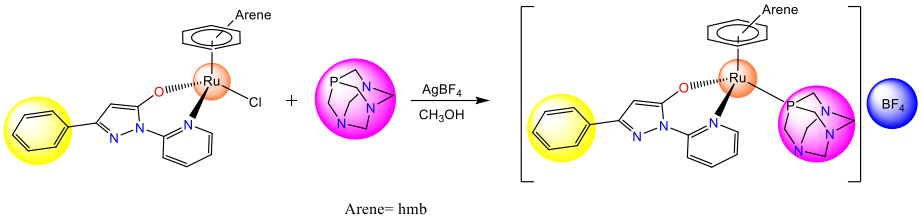

Figure 44. Reaction scheme of Complex 4 synthesis.

Complex **4** has been synthetized similarly to **3**, using complex **2** (75.4 mg, 0.14 mmol), $AgBF_4$ (98 % of purity) (28.8 mg, 0.14 mmol), and PTA (97%) (23.5 mg, 0.14 mmol). It is an orange solid (78.0 mg, 0.10 mmol, yield 72.3 %) which is very soluble in alcohols, DMSO, DMF and acetone and chlorinated solvents and slightly soluble in water and acetonitrile. Anal. Calcd for $C_{32}H_{40}BF_4N_6OPRu$ (mw: 743): C, 51.69; H, 5.42; N, 11.30%. Found: C, 51.53; H, 5.37; N, 11.21%. Λ_m (DMSO, 297 K, $1 \cdot 10^{-3}$ mol/L): 25.9 S cm^2 mol^{-1}. It decomposes gradually with temperature after 249°C. IR (cm^{-3}): 2920w ν(C-H), 1602w ν(C-N), 1587s ν(C=O), 1576s, 1554s, 1469s, 1447m, 1411m, 1365m, 1295w, 1244w, 1053vs and 1028vs ν(BF_4), 974vs, 950vs, 944m, 785s, 773s, 684w, 671w, 643w, 609w, 582m, 572m, 557s, 524w, 475m, 453m, 392w, 329m, 203m. ^{1}H-NMR (500 Hz, 298 K, CD_3CN): δ, 2.16s (18H, CH_3 of hmb), 4.04m (6H, (P-C*H*$_2$-N)$_3$ of PTA phosphine), 4.45m (6H, (N-C*H*$_2$-N)$_3$ of PTA phosphine), 5.91s (1H, C4-H of $L^{py,ph}$), 7.30ddd (1H, $^3J_{(H—H)}$= 7.3, 5.9 Hz, $^4J_{(H—H)}$= 1.7 Hz, C9-H of $L^{py,ph}$), 7.42m (1H, C14-H of $L^{py,ph}$), 7.48m (2H, C13,13'-H of $L^{py,ph}$), 7.90m (2H, C12,12'-H of $L^{py,ph}$), 8.05dd (1H, $^3J_{(H—H)}$= 7.5 Hz, $^4J_{(H—H)}$= 1.6 Hz, C7-H of $L^{py,ph}$), 8.10ddd (1H, $^3J_{(H—H)}$= 8.7, 7.1, $^4J_{(H—H)}$= 1.6 Hz, C8-H of $L^{py,ph}$), 8.13dd (1H, $^3J_{(H—H)}$= 6.0 Hz, $^4J_{(H—H)}$= 1.6 Hz, C10-H of $L^{py,ph}$). ^{13}C-NMR (500 Hz, 298K, CD_3CN): δ, 15.3 (CH_3 of hmb), 43.4d ($^1J_{(P—C)}$= 13.5 Hz, (P-*C*H$_2$-N)$_3$ of PTA phosphine), 72.3d ($^3J_{(P—C)}$= 7 Hz, (N-*C*H$_2$-N)$_3$ of PTA phosphine), 88.2 (C4 of $L^{py,ph}$), 99.0 (C_{arom} of hmb), 117.3 (C7 of $L^{py,ph}$), 121.8 (C9 of $L^{py,ph}$), 125.5 (C12,12' of $L^{py,ph}$), 128.7

(C14,13,13' of $L^{py,ph}$), 133.4 (C11 of $L^{py,ph}$), 141.4 (C8 of $L^{py,ph}$), 151.1 (C6 of $L^{py,ph}$),153.4 (C10 of $L^{py,ph}$), 154.7 (C3 of $L^{py,ph}$), 162.0 (C5 of $L^{py,ph}$). {^{1}H-^{15}N}-g-HMBC NMR in **(**CD_3CN, 51 MHz, $^{3}J_{(N—H)}$ = 3 Hz, at 298 K): δ_N, 39.6 (N_{PTA}), 186.5 (N_{py} of $L^{py,ph}$), 205.6 (N1 of $L^{py,ph}$), N2 of $L^{py,ph}$ not observed.. ESI-MS (+) (CH_3OH) (m/z, relative intensity %): 657 [100] [Ru(hmb)($L^{py,ph}$)PTA]$^{+}$.

[Ru(cym)($L^{py,me}$)PTA]BF_4 ***(5)***

Reaction in Figure 45:

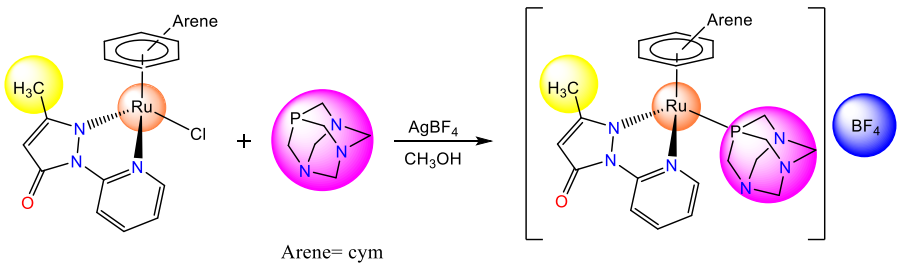

Figure 45. Reaction scheme of Complex 5 synthesis.

Complex **5** was prepared from [Ru(cym)($L^{py,me}$)Cl], previously reported.[84] 82.4 mg (0.15 mmol) of the starting complex were dissolved in 30 ml of methanol and it was added to 1 ml of an aqueous solution of $AgBF_4$ (98 % of purity) (29.8 mg, 0.15 mmol). PTA (97 % of purity) was added (24.3 mg, 0.15 mmol) and the solution was stirred for 2h. An orange solution appeared. AgCl was formed as by-product, and it was filtered. The remaining solution was dried to about 4 ml and about 30 ml of Et_2O was added, affording a brown precipitate which was shown to be complex **5** (240 mg, 0.37 mmol, yield 75.1%). It is soluble in alcohols, acetonitrile, DMSO, DMF and water. It is slightly soluble in acetone and chlorinated solvents. Anal. Calcd for $C_{25}H_{34}BF_4N_6OPRu$ (mw: 653.44): C, 45.95; H, 5.24; N, 12.86%. Found: C, 45.80; H, 5.28; N, 12.72%. Λ_m (DMSO, 297 K, $1 \cdot 10^{-3}$ M): 25.3 S cm^2 mol^{-1}. It decomposes gradually with temperature starting from about 234°C. IR (cm^{-3}): 3596w, 3077w ν(C-H aromatics),

2930w ν(C-H aliphatic), 1625s ν(C=O), 1594m, 1474s, 1442m, 1418m, 1363m, 1289m, 1244m, 1213m, 1059vs and 1026vs ν(BF_4), 1013vs, 972vs, 947vs, 895m, 802m, 777m, 741s, 609s, 573s, 520m, 476m, 451m, 392m, 322w, 278m, 248w, 234w, 214w, 202s. ^{1}H-NMR (500 Hz, 298 K, DMSO): δ, 0.86d, 0.99 (6H, $^{3}J_{(H—H)}$= 6.9 Hz, CH_3-C_6H_4-CH-(C*H*$_3$)$_2$ of cym), 2.17s (3H, C-C*H*$_3$ of $L^{py,me}$), 2.45s (3H, C*H*$_3$-C_6H_4-CH-(CH_3)$_2$ of cym), 2.52m (1H, CH_3-C_6H_4-C*H*-(CH_3)$_2$ of cym), 3.75m (6H, (P-C*H*$_2$-N)$_3$ of PTA phosphine), 4.36m (6H, (N-C*H*$_2$-N)$_3$ of PTA phosphine), 4.85s (1H, C4-H of $L^{py,me}$), 6.12d, 6.18d, 6.27d, 6.28d (4H, $^{3}J_{(H—H)}$= 6.3 Hz, CH_3-C_6*H*$_4$-CH-(CH_3)$_2$ of cym), 7.22t (1H, $^{3}J_{(H—H)}$= 6.6 Hz, H9 of $L^{py,me}$), 8.08t (1H, $^{3}J_{(H—H)}$= 7.9 Hz, C8-H of $L^{py,me}$), 8.49d (1H $^{3}J_{(H—H)}$= 8.6 Hz, C7-H of $L^{py,me}$), 8.56d (1H, $^{3}J_{(H—H)}$= 5.9 Hz, C10-H of $L^{py,me}$). ^{13}C{^{1}H} NMR (500 Hz, 298 K, DMSO): δ, 17.4 (C3-*C*H$_3$ of $L^{py,me}$), 19.5 (*C*H$_3$-C_6H_4-CH-(CH_3)$_2$ of cym), 21.7, 22.8 (CH_3-C_6H_4-CH-(*C*H$_3$)$_2$ of cym), 31.5 (CH_3-C_6H_4-*C*H-(CH_3)$_2$ of cym), 51.0d ($^{1}J_{(P—C)}$= 14.0 Hz, (P-*C*H$_2$-N)$_3$ of PTA phosphine), 72.1d ($^{3}J_{(P—C)}$= 7.7 Hz, (N-*C*H$_2$-N)$_3$ of PTA phosphine), 88.5 (C4 of $L^{py,me}$), 88.6, 89.1, 89.1, 89.2, 89.6, 89.6 (CH_3-*C*$_6$H$_4$-CH-(CH_3)$_2$ of cym), 111.3 (C7 of $L^{py,me}$), 120.9 (C9 of $L^{py,me}$), 142.0 (C8 of $L^{py,me}$), 151.1 (C3 of $L^{py,me}$), 154.4 (C10 of $L^{py,me}$), 160.6 (C6 of $L^{py,me}$), 165.8 (C5 of $L^{py,me}$). ^{31}P{^{1}H} NMR (500 Hz, 298 K, DMSO): δ, -31.78. {^{1}H-^{15}N}-g-HMBC NMR **(**DMSO, 51 MHz, $^{3}J_{(N—H)}$= 3 Hz, at 298 K): δ_N, 43.4 (N_{PTA}), 135.0 (N2 of $L^{py,me}$), 177.1 (N_{py} of $L^{py,me}$), 205.6 (N1 of $L^{py,me}$). ESI-MS (+) (CH_3OH) (m/z, relative intensity %): 410 [100] [Ru(cym)($L^{py,me}$)]$^{+}$, 567 [81] [Ru(cym)($L^{py,me}$)PTA]$^{+}$.

[Ru(hmb)(L^{py,me})PTA]BF$_4$ ***(6)***

Reaction in Figure 46:

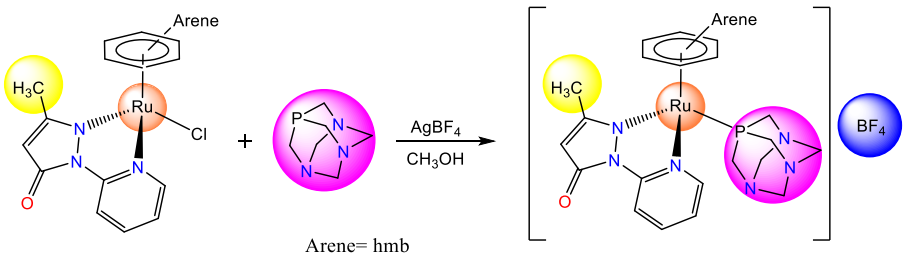

Figure 46. Reaction scheme of Complex 6 synthesis.

Complex **6** was prepared using a method similar to that of **5** from [Ru(hmb)(L^{py,me})Cl], previously reported.[84] 213.7 mg (0.45 mmol) of the starting complex were dissolved in 30 ml of methanol. 89.7 mg (0.45 mmol) of $AgBF_4$ (98 % of purity) and 73.2 mg (0.45 mmol) of PTA phosphine (97 % of purity) were used, affording a brown precipitate which was shown to be complex **6** (168.9 mg, 0.26 mmol, yield 57.5%). It is soluble in water, alcohols, DMSO, DMF, acetonitrile and chlorinated solvents. It is slightly soluble in acetone. Anal. Calcd for $C_{27}H_{38}BF_4N_6OPRu$ (mw: 681.49): C, 47.59; H, 5.62; N, 12.33%. Found: C, 47.36; H, 5.59; N, 12.20%. Λ_m (DMSO, 297 K, $4.5 \cdot 10^{-4}$ M): 13.12 S cm^2 mol^{-1}. It decomposes gradually with temperature starting from about 205°C. IR (cm^{-3}): 3118w ν(C-H aromatics), 2948w, 2919w, 2871w ν(C-H aliphatic), 1655s ν(C=O), 1603m ν(C-N), 1475s, 1441m, 1420m, 1358s, 1286m, 1241m, 1156m and 1024vs ν(BF_4), 1007vs, 972vs, 946vs, 893m, 799m, 779s, 734s, 708m, 670w, 609w, 572m, 519m, 475m, 452m, 392w, 355w, 322w, 277w, 248w, 202m. ^{1}H-NMR (500 Hz, 298 K, DMSO): δ, 2.11s (18H, C*H*$_3$ of hmb), 2.13s (C3-C*H*$_3$ of L^{py,me}) 3.63dd, 3.79dd (6H, $^2J_{(H—H)}$= 15.0, $^3J_{(P—H)}$= 3.6 Hz, (P-C*H*$_2$-N)$_3$ of PTA phosphine), 4.34s (6H, (N-C*H*$_2$-N) of PTA phosphine), 4.82s (1H, C4-H of L^{py,me}), 7.28ddd (1H, $^3J_{(H—H)}$= 7.4, 6.0, $^4J_{(H—H)}$= 1.5 Hz, C9-H of L^{py,me}), 8.08ddd (1H, $^3J_{(H—H)}$= 8.7, 7.2, $^4J_{(H—H)}$= 1.5 Hz, C8-H of L^{py,me}), 8.14dd (1H, $^3J_{(H—H)}$= 6.0, $^4J_{(H—H)}$= 1.6 Hz, C10-H of L$^{py.me}$), 8.56dd (1H, $^3J_{(H-H)}$= 8.6, 1.4 Hz, C7-H

of $L^{py,me}$). $^{13}C\{^1H\}$ NMR (500 Hz, 298 K, DMSO): δ, 16.7 (CH_3 of hmb), 17.5 (C3-CH_3 of $L^{py,me}$), 49.8 ((P-CH_2-N)$_3$ of PTA phosphine), 72.0 ((N-CH_2-N)$_3$ of PTA phosphine), 88.5 (C4 of $L^{py,me}$), 102.3 (Carom of hmb), 110.7 (C10 of $L^{py,me}$), 121.4 (C9 of $L^{py,me}$), 141.7 (C7 of $L^{py,me}$), 151.2 (C6 of $L^{py,me}$), 152.0 (C8 of $L^{py,me}$), 160.9 (C3 of $L^{py,me}$), 166.7 (C5 of $L^{py,me}$). ^{31}P-NMR (500 Hz, 298 K, DMSO): δ, -38.71. $\{^1H$-$^{15}N\}$-g-HMBC NMR **(**DMSO, 51 MHz, $^3J_{(N—H)}$= 3 Hz, at 298 K): δ_N, 40.0 (N_{PTA}), 139.9 (N2 of $L^{py,me}$), 180.4 (N_{py} of $L^{py,me}$), 205.4 (N1 of $L^{py,me}$). ESI-MS (+) (CH_3OH) (m/z, relative intensity %): 438 [100] $[Ru(cym)(L^{py,me})]^+$, 595 [55] $[Ru(cym)(L^{py,me})PTA]^+$.

[Ru(cym)($Q^{py,CF3}$)PTA]PF_6 ***(7)***

Reaction in Figure 47:

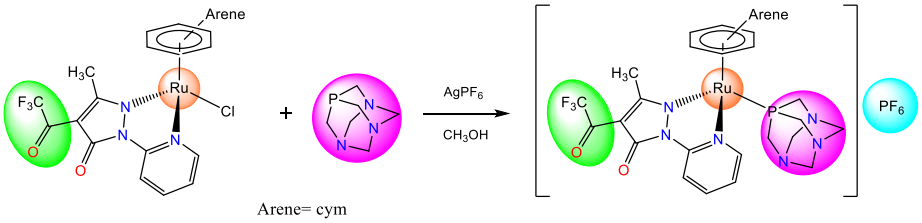

Figure 47. Reaction scheme of Complex 7 synthesis.

Complex **7** was prepared using a method similar to that of **6** from [Ru(cym)($Q^{py,CF3}$)Cl], previously reported.[84] 38.3 mg (0.07 mmol) of the starting complex were dissolved in 30 ml of methanol and an aqueous solution (1 ml) of $AgPF_6$ (18.5 mg, 0.07 mmol) was added. Then, 11.5 mg (0.07 mmol) of PTA (97 % of purity) was added and the solution was stirred for 2h. AgCl was formed as by-product, and it was filtered. The remaining dark yellow solution was dried to about 4 ml and about 30 ml of Et_2O was added, affording a yellow precipitate which was shown to be complex **7** (42.5 mg, 0.05 mmol, yield 75.2%). It is soluble in DMSO, DMF. Anal. Calcd for $C_{27}H_{33}F_9N_6O_2P_2Ru$ (mw: 807.61): C, 40.16; H, 4.12; N, 10.41%. Found: C, 40.05; H, 4.24; N, 10.30%. It decomposes gradually with temperature, starting from about 281°C. Λ_m (DMF, 298 K,

$1.7 \cdot 10^{-4}$ M): 12.23 S cm^2 mol^{-1}. IR (cm^{-1}): 3081w ν(C—H aromatics), 2932w ν(C—H aliphatic), 1697m, 1682 ν(C=O), 1647vs ν(C—N), 1517m, 1464vs, 1340s, 1256s, 1190m, 1150s, 1054vs, 1011vs, 975m, 949m, 834vs ν(PF_6), 773s, 728s, 685m, 611w, 582s,557vs, 525w, 479m, 453m, 384m, 281w. ^{1}H-NMR (500 Hz, DMSO, 298K): δ, 0.77d (3H, $^3J_{(H—H)}$= 6.8 Hz, CH_3-C_6H_4-CH-(C*H*$_3$)$_2$ of cym), 1.02d (3H, $^3J_{(H—H)}$= 6.8 Hz, CH_3-C_6H_4-CH-(C*H*$_3$)$_2$ of cym), 2.46s (3H, C*H*$_3$-C_6H_4-CH-(CH_3)$_2$ of cym), 2.46m (1H, CH_3-C_6H_4-C*H*-(CH_3)$_2$ of cym), 2.54s (3H, C3-CH_3 of $Q^{py,CF3}$) 3.89m (6H, (P-C*H*$_2$-N)$_3$ of PTA phosphine), 4.40m (6H, (N-C*H*$_2$-N)$_3$ of PTA phosphine), 6.12d, 6.31d, 6.33d 6.44d (4H, $^3J_{(H—H)}$= 6.4 Hz, CH_3-C_6*H*$_4$-CH-(CH_3)$_2$ of cym), 7.37ddd (1H, $^3J_{(H—H)}$= 7.4, 5.9 Hz, $^4J_{(H—H)}$= 1.4 Hz, C9-H of $Q^{py,CF3}$), 8.20ddd (1H, $^3J_{(H—H)}$= 8.6, 7.2 Hz, $^4J_{(H—H)}$= 1.5 Hz, C8-H of $Q^{py,CF3}$), 8.47dd (1H, $^3J_{(H—H)}$= 8.6 Hz, $^4J_{(H—H)}$= 1.4 Hz, C7-H of $Q^{py,CF3}$), 8.63dd (1H, $^3J_{(H—H)}$= 5.9 Hz, $^4J_{(H—H)}$= 1.5 Hz, C10-H of $Q^{py,CF3}$). ^{19}F{^{1}H} NMR (500 Hz, DMSO, 298K): δ, -69.4s, -70.9s (PF_6^-), -74.5s (CF_3). ^{31}P{^{1}H} NMR (500 Hz, DMSO, 298K): δ, -32.8 (PTA phosphine), -142.4hept (PF_6^-, $^1J_{(P—F)}$= 711.1 Hz). ^{13}C{^{1}H} NMR (500 Hz, DMSO, 298K): δ, 19.1 (*C*H_3-C_6H_4-CH-(CH_3)$_2$ of cym), 20.0 (C3-*C*H_3 of $Q^{py,CF3}$), 20.9, 22.9 (CH_3-C_6H_4-CH-(*C*H_3)$_2$ of cym), 31.3 (CH_3-C_6H_4-*C*H-(CH_3)$_2$ of cym), 50.5d ($^1J_{(P—C)}$= 14.0 Hz, (P-*C*H_2-N)$_3$ of PTA phosphine), 71.8 ($^4J_{(P—C)}$= 7.8 Hz (N-*C*H_2-N)$_3$ of PTA phosphine), 88.5, 90.1, 90.4 (CH_3-*C*$_6H_4$-CH-(CH_3)$_2$ of cym), 99.7 (C4 of $Q^{py,CF3}$) 102.6 (CH_3-*C*$_6H_4$-CH-(CH_3)$_2$ of cym), 111.7 (C7 of $Q^{py,CF3}$), 117.2q ($^1J_{(C—F)}$: 289.9 Hz, (C=O)*C*F_3 of $Q^{py,CF3}$), 122.2 (C9 of $Q^{py,CF3}$), 122.9 (CH_3-*C*$_6H_4$-CH-(CH_3)$_2$ of cym), 142.6 (C8 of $Q^{py,CF3}$), 150.0 (C6 of $Q^{py,CF3}$), 154.4 (C10 of $Q^{py,CF3}$), 161.5 (C5 of $Q^{py,CF3}$), 164.3 (C3 of $Q^{py,CF3}$), 170.7q ($^2J_{(C—F)}$= 35.9 Hz (*C*=O)CF_3 of $Q^{py,CF3}$). {^{1}H-^{15}N}-g-HMBC NMR **(**DMSO, 51 MHz, $^3J_{(N—H)}$= 3 Hz, at 298 K): δ_N, 42.8 (N_{PTA}), 167.3 (N2 of $Q^{py,CF3}$), 179.7 (N_{py} of $Q^{py,CF3}$), N1 of $Q^{py,CF3}$ not observed. ESI-MS **(+)** (CH_3CN) (m/z, relative intensity %): 663 [100] [Ru(cym)($Q^{py,CF3}$)PTA]$^+$, 506 [29] [Ru(cym)($Q^{py,CF3}$)]$^+$.

[Ru(hmb)($Q^{py,CF3}$)PTA]PF_6 ***(8)***

Reaction in Figure 48:

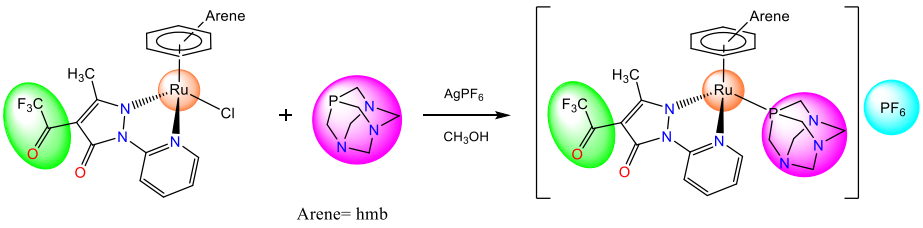

Figure 48. Reaction scheme of Complex 8 synthesis.

Complex **8** was prepared using a method similar to that of **7** from [Ru(hmb)($Q^{py,CF3}$)Cl], previously reported.[84] 96.1 mg (0.17 mmol) of the starting complex were dissolved in 30 ml of methanol and an aqueous solution (1 ml) of $AgPF_6$ (43.0 mg, 0.17 mmol) was added. Then, 27.5 mg (0.17 mmol) of PTA (97 % of purity) was added and the solution was stirred for 2h. AgCl was formed as by-product, and it was filtered. The remaining dark yellow solution was dried to about 4 ml and about 30 ml of Et_2O was added, affording a yellow precipitate which was shown to be complex **8**. It is soluble in DMSO, DMF. Anal.Calcd for $C_{29}H_{37}F_9N_6O_2P_2Ru$ (mw: 835.66): C, 41.68; H, 4.46; N, 10.06%. Found: C, 41.55; H, 4.54; N, 9.97%. It decomposes gradually from 292°C. Λ_m (DMF, 298 K, $2 \cdot 10^{-4}$ M): 11.88 S cm^2 mol^{-1}. IR (cm^{-1}): 3081w ν(C—H aromatics), 2935w ν(C—H aliphatic), 1674m, 1652s ν(C—N), 1516w, 1464s, 1341m, 1255m, 1192m, 1156s, 1048s, 1017m, 925s, 834vs ν(PF_6), 784s, 725m, 684w, 608w, 582s, 557vs, 524w, 475m, 453w, 392w, 329m, 278w, 203w. ^{1}H-NMR (500 Hz, DMSO, 298K): δ, 2.12s (18H, CH_3 of hmb), 2.49s (3H, C3-CH_3 of $Q^{py,CF3}$) 3.83m (6H, (P-CH_2-N)$_3$ of PTA phosphine), 4.37m (6H, (N-CH_2-N)$_3$ of PTA phosphine), 7.42ddd (1H, $^3J_{(H—H)}$= 7.4, 5.9, $^4J_{(H—H)}$= 1.5 Hz, C9-H of $Q^{py,CF3}$), 8.20ddd (1H, $^3J_{(H—H)}$= 8.7, 7.3, $^4J_{(H—H)}$= 1.5 Hz, C8-H of $Q^{py,CF3}$), 8.23dd (1H, $^3J_{(H—H)}$= 6.0 Hz, $^4J_{(H—H)}$= 1.4 Hz, C10-H of $Q^{py,CF3}$), 8.46dd (1H, $^3J_{(H—H)}$= 8.7 Hz, $^4J_{(H—H)}$= 1.3 Hz, C7-H of $Q^{py,CF3}$). ^{19}F{^{1}H} NMR (500 Hz, DMSO, 298K): δ, -69.4s, -70.9s (PF_6^-), -74.5s (CF_3). ^{31}P{^{1}H} NMR (500 Hz, DMSO, 298K): δ, -

40.3 (PTA phosphine), -144.2hept (PF_6^-, $^1J_{(P—F)}$= 711.1 Hz). $^{13}C\{^1H\}$ NMR (500 Hz, DMSO, 298K): δ, 16.7 (CH_3 of hmb), 20.7 (C3-CH_3 of $Q^{py,CF3}$), 49.6d ($^1J_{(P—C)}$= 13.4 Hz, (P-CH_2-N)$_3$ of PTA phosphine), 71.9 ($^4J_{(P—C)}$= 7.5 Hz (N-CH_2-N)$_3$ of PTA phosphine), 99.9 (C4 of $Q^{py,CF3}$), 103.1 ($C_{aromatics}$ of hmb) 111.5 (C7 of $Q^{py,CF3}$), 117.2q ($^1J_{(C—F)}$= 290.4 Hz, (C=O)CF_3 of $Q^{py,CF3}$), 122.8 (C9 of $Q^{py,CF3}$), 142.5 (C8 of $Q^{py,CF3}$), 150.1 (C6 of $Q^{py,CF3}$), 152.4 (C10 of $Q^{py,CF3}$), 162.3 (C5 of $Q^{py,CF3}$), 164.8 (C3 of $Q^{py,CF3}$), 170.5q ($^2J_{(C—F)}$= 35.8 Hz (C=O)CF_3 of $Q^{py,CF3}$). $\{^1H$-$^{15}N\}$-g-HMBC NMR **(**DMSO, 51 MHz, $^3J_{(N—H)}$= 3 Hz, at 298 K): δ_N, 40.0 (N_{PTA}), 172.6 (N2 of $Q^{py,CF3}$), 182.8 (N^{py} of $Q^{py,CF3}$), N1 of $Q^{py,CF3}$ not observed. ESI-MS **(+)** (CH_3CN) (m/z, relative intensity %): 691 [100] $[Ru(cym)(Q^{py,CF3})PTA]^+$.

Results and Discussion

The proligands $HL^{py,ph}$ and $HL^{py,Me}$ are similar but the first has a phenyl instead of the methyl in 3-position of pyrazole. In principle, different tautomeric forms are possible for $HL^{py,ph}$ and they are shown in Figure 49. However, the solid-state X-ray structure corresponds to rotamer I-r, which is stabilized by the intramolecular hydrogen bond O-H···N. Rotamer I-r is the only one observed in chlorinated solvents, as shown by the broad resonance at 12.86 ppm found in the ^{1}H-NMR spectrum at room temperature (Figure 50A). ^{13}C-NMR is shown in Figure 50B. N-H coupling was absent in the HSQC ^{1}H-^{15}N NMR spectrum at room temperature, providing additional evidence for the presence of enol group in $CDCl_3$.

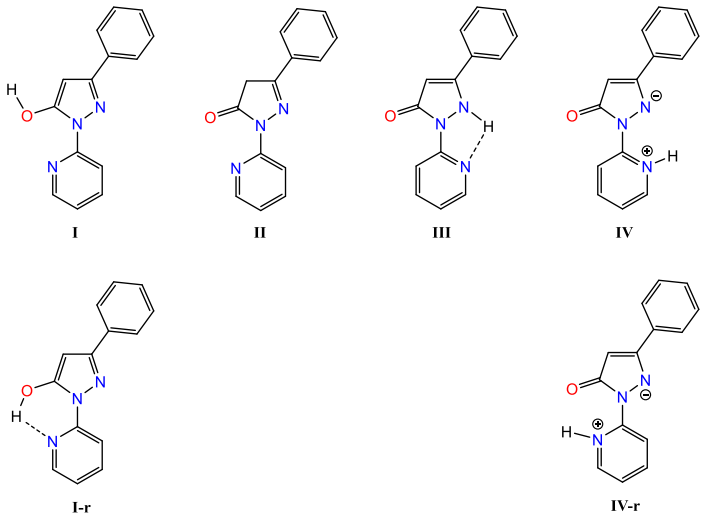

Figure 49. Possible Tautomers and Rotamers of HL^{py,ph}

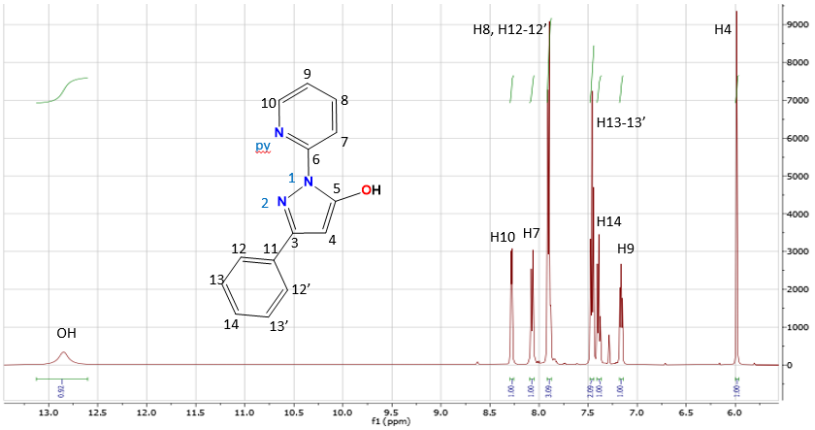

A

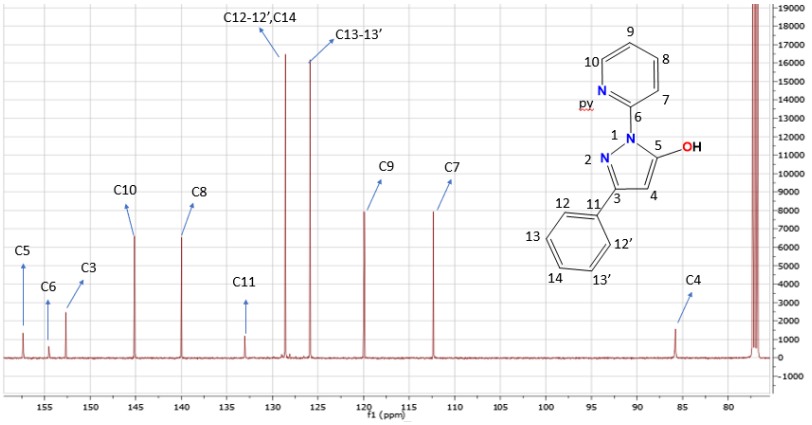

B

Figure 50. ^{1}H-NMR (A) and ^{13}C-NMR (B) of Proligand HL^{py,ph}.

Arene-Ru(II) complexes **1** and **2** were synthesized from reaction of HL^{py,ph} with [Ru(arene)Cl_2]$_2$ [where arene = *p*-cymene (cym) or hexamethyl-

benzene (hmb)] in methanol in the presence of KOH and complexes **3** and **4** were obtained by reaction of **1** and **2** in methanol with aqueous $AgBF_4$ to remove the chloride from the Ru(II) coordination sphere, followed by addition of PTA. X-Ray diffraction analysis show the preference of $HL^{py,ph}$ in its deprotonated form ($L^{py,ph}$) to coordinate Ru center as *N,O*- chelating ligand (Figure 51 show the X-Ray structure of complex **2)**, differently respect $L^{py,Me}$ and its derivative $Q^{py,CF3}$ which coordinates the metal center as *N,N*- donors, as shown in Figure 39. The X-Ray analysis of complex **3** is reported in detail below.

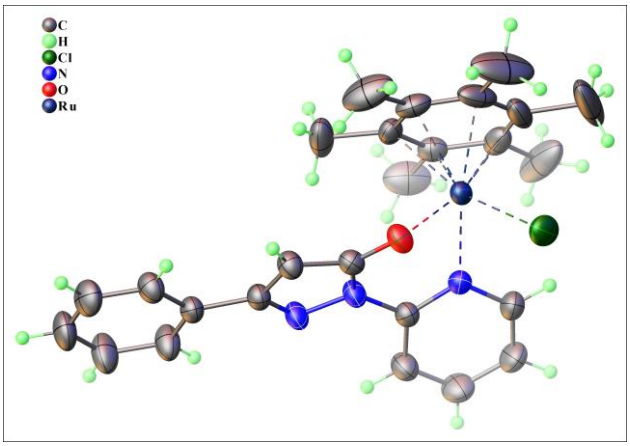

Figure 51. X-Ray structures of complex 2

The different coordination of the two ligands may be described considering the electron-withdrawing behavior of phenyl group in $L^{py,ph}$ which depletes of electron density the N2 atom of pyrazole, causing the coordination through the oxygen atom.

Conductivity measurements of **3** and **4** in DMSO confirmed their ionic nature, with Λ_m values in the range 23-26 $cm^2\ mol^{-1}$, typical of 1:1 electrolytes.[100]

Ionic complexes **3** and **4** have an enhanced solubility in polar solvents, including water, respect neutral compounds **1** and **2**.

In ESI-MS analysis of **1** and **2** performed in methanol/acetonitrile demonstrate the presence of $[Ru(arene)(L^{py,ph})]^+$ in solution, due from the chloride loss. Complexes **3** and **4** ESI-MS measures show the presence of

both [Ru(arene)($L^{py,ph}$)]$^+$ and [Ru(arene)($L^{py,ph}$)(PTA)]$^+$ species in solution.

In the IR spectra, the most relevant aspect is the progressive reduction of the ν(C=O) vibration mode from 1654 cm^{-1} in $HL^{py,ph}$ to 1632-1635 cm^{-1} in the neutral complexes **1** and **2**, in correspondence with coordination in N,O-chelating mode by deprotonation of tautomer I-r of proligand, and to 1626 and 1587 cm^{-1} in the spectra of **3** and **4** respectively, in accordance to the ionic nature of the complexes which further strengths the Ru-O bonding thus lowering the C=O bonding order.[101–104]

IR spectra of **3** and **4** show a strong and sharp absorptions at ca. 1054 and 1028-1034 cm^{-1} that confirm the presence of the BF_4^- anion.[105]

In the far-IR region strong bands due to ν(Ru-N), ν(Ru-O) and ν(Ru-Cl) stretching modes in **1** and **2** were assigned below 500 cm^{-1}.[106]

The proton and carbon assignments of the free ligand and complexes **1**–**4** have been made based on {^{1}H -^{1}H}-COSY, {^{1}H-^{13}C}-HSQC, and {^{1}H-^{13}C}-HMBC spectroscopy that are present in the Supporting Information of the lust publication.[107]

The ^{1}H and ^{13}C NMR spectra of **1**–**4** were recorded in $CDCl_3$ or CD_3CN and show the shift in frequency that we expected for the resonances of the pyrazolone and pyridyl protons and carbon atoms, respect the free ligand.

In the ^{31}P NMR spectra of **3** and **4**, the phosphorus of PTA presents a singlet at −37.7 and −40.7 ppm, respectively. Some examples are shown below in Figure 52A-D:

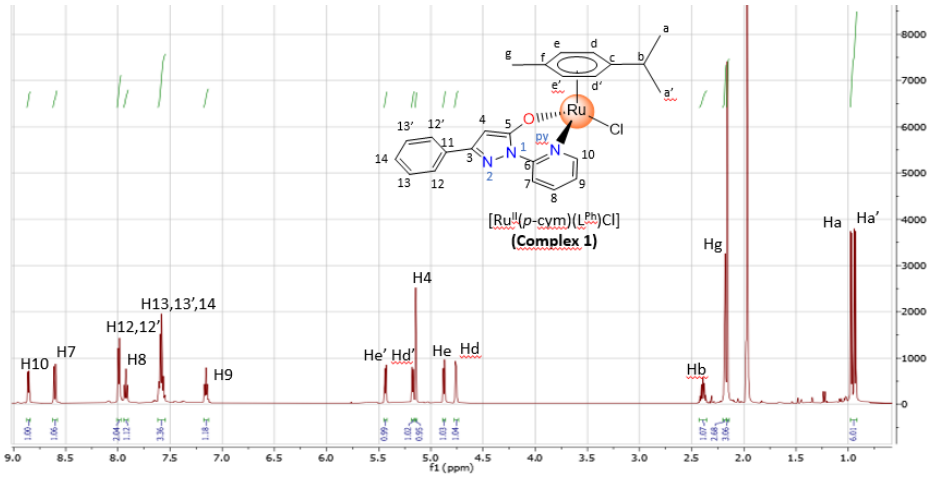

A

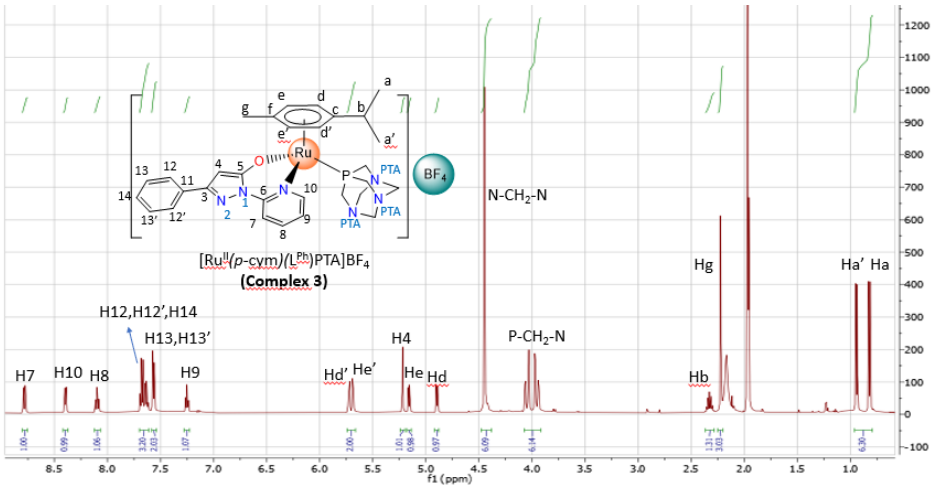

B

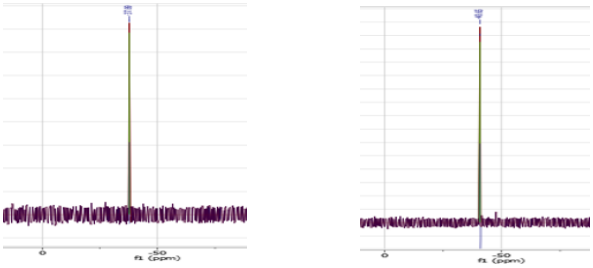

C D

Figure 52. Examples of [1]H-NMR. In A it is represented the Complex 1 and in B it is represented the Complex 3, both performed in CD_3CN. In B appears additional signals related to substitution of chloride with PTA. C and D are [31]P-NMR of complex 3 and 4 respectively

Cationic RAPTA complexes **5-8** were prepared using a procedure similar to that applicated for **3** and **4**, starting from [Ru(arene)($L^{py,me}$)Cl] and [Ru(arene)($Q^{py,CF3}$)Cl].

In **5**–**8** the ligands act in a *N*,*N*-chelating fashion, and in general they are less soluble in common solvents than **1**–**4**. Electrical conductivity measurements were carried out in DMSO, showing that all **5-8** complexes are 1:1 electrolytes. In the IR spectra we can see displacements of the stretching of the carbonyl to larger wave numbers after coordination, in agreement with the non-involvement of the oxygen atom of the pyrazole-ring in the coordination of Ruthenium. The presence of the counterions is confirmed by the bands at medium-high intensity at ca. 1050 and 1030 cm^{-1} for the BF_4^- in **5** and **6** and a very strong band at 834 cm^{-1} relative to the PF_6^- in complexes **7** and **8**.[108,109]

ESI-MS of **5** and **6** reveal the presence of $[Ru(arene)(L^{py,me})]^+$ and $[Ru(arene)(L^{py,me})PTA]^+$ fragments whereas in the MS spectra of **7** and **8** a unique peak is observed corresponding to $[Ru(arene)(Q^{py,CF3})PTA]^+$.
In ^1H and ^{13}C NMR spectra of **5-8** the expected variation of chemical shifts was observed for the pyrazolone ligands upon coordination. The ^{31}P NMR spectra of **7** and **8** contain a singlet at −32 and −40 ppm, respectively, with the PF_6^- anion giving a septet at ca. −143 ppm, related to the coupling with the six fluorine atoms. Comparing the $\{^1H$-$^{15}N\}$-HMBC spectra of the free ligands with their metal complexes, the assignation of indirect ^{15}N-NMR chemical shifts is possible (Table 3). A general observation involves a shift of the N1 and N2 atoms of pyrazolone resonances and that of N_{py} of the pyridine moiety upon chelation to ruthenium, with the shift of N_{py} being much larger when PTA is present in primary coordination sphere.

Table 3. ^{15}N chemical shifts (ppm) in the free ligands and complexes obtained from $\{^1H$-$^{15}N\}$ HMBC NMR spectroscopy.

	N1	N2	N_{py}	N_{PTA}
$HL^{py,ph}$	263.1	194.5	251.9	
$[Ru(cym)(L^{py,ph})Cl]$ (**1**)	205.3	157.0	202.9	
$[Ru(hmb)(L^{py,ph})Cl]$ (**2**)	206.1	not observed	not observed	
$[Ru(cym)(L^{py,ph})(PTA)]BF_4$ (**3**)	206.8	131.5	176.5	42.5
$[Ru(hmb)(L^{py,ph})(PTA)]BF_4$ (**4**)	205.6	not observed	186.5	39.6
$HL^{py,me}$ [84]	191.4	322.2	252.4	
$[Ru(cym)(L^{py,me})(PTA)]BF_4$ (**5**)	205.6	135.0	177.1	43.4
$[Ru(hmb)(L^{py,me})(PTA)]BF_4$ (**6**)	205.4	139.9	180.4	40.0
$HQ^{py,CF3}$ [84]	not observed	267.9	229.6	
$[Ru(cym)(Q^{py,CF3})(PTA)]PF_6$ (**7**)	not observed	167.3	179.7	42.8
$[Ru(hmb)(Q^{py,CF3})(PTA)]PF_6$ (**8**)	not observed	172.6	182.8	40.0

X-Ray Diffraction study

The crystal structure of the $HL^{py,ph}$ ligand previously reported[88] (Figure 53) confirms the rotamer I-r, as also DFT calculations results (see below) show like the most stable.

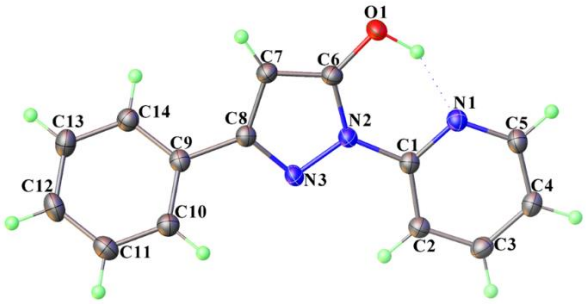

Figure 53. X-Ray crystallography structure of Rotamer $HL^{py,ph}$ I-r.

Complex **3** X-Ray analysis are reported. It is crystallized in a monoclinic system with a space group $P2_1/n$, made of 8 molecules in the unit cell. In its X-ray structure analysis, it is noteworthy to mention that there are two independent salts with similar structural parameters and that the crystal shows both enantiomers. In Figure 54 is shown one of the independent asymmetric unit of **3**.

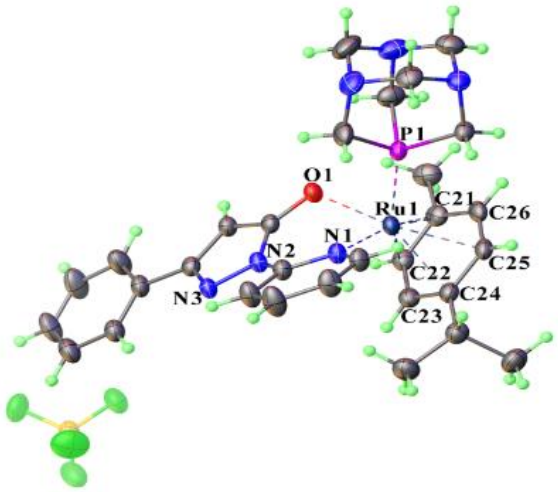

Figure 54. X-Ray structure of Complex 3

In general, the coordination sphere around Ru(II) center acquires a pseudo-tetrahedral geometry, where the p-cymene molecule is bonded in η^6-coordination mode to the ion center, while the remaining sites of coordination are filled by deprotonated bidentate L^- ligand through N1 pyridine atom and deprotonated O1 atom, and P atom of the PTA ligand.

The coordination of pyrazole ligand to the metal center with N and O forms a six-membered ring with bite angle N(7)-Ru(2)-O(2) 83.38(7)° and N(1)-Ru(1)-O(1) 83.10(7)°, bond length O(1)-Ru(1) 2.0892(15) and O(2)-Ru(2) 2.0883(15); N(1)- Ru(1) 2.1258(18) and N(7)- Ru(1) 2.1210(18) Å for the complexes. The Ru(II) ion is π-bonded to the arene ring with an average Ru(1)-C and Ru(2)-C distance of 1.746 Å and 1.716 Å respectively. Is has been possible to demonstrate the distorted octahedron structure of the complexes thanks these results.

DFT study

With the collaboration of Professor Galindo of the University of Lisbon, Density functional theory (DFT) was used to examinate the possible $HL^{py,ph}$ proligand tautomers and rotamers. The resulting structures and their relative energies are reported in Figure 55.

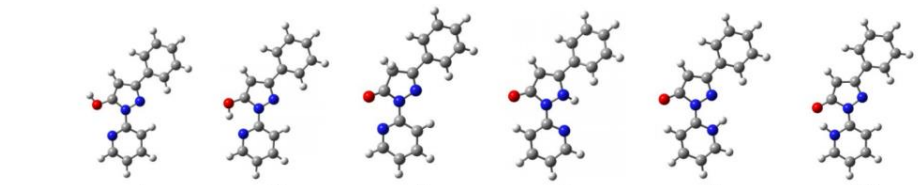

	I	I-r	II	III	IV	IV-r
E	-779.771866806	-779.789886434	-779.778761223	-779.784208708	-779.768829482	-779.776187311
Eo	-779.547996000	-779.565307000	-779.555578000	-779.559843000	-779.544629000	-779.553443000
Et	-779.533919000	-779.552650000	-779.541613000	-779.546047000	-779.531763000	-779.539831000
H	-779.532975000	-779.551706000	-779.540669000	-779.545103000	-779.530819000	-779.538887000
G	-779.591083000	-779.605208000	-779.598475000	-779.601925000	-779.584619000	-779.596435000
ΔE	11.3	0.0	7.0	3.6	13.2	8.6
ΔG	8.9	0.0	4.2	2.1	12.9	5.5

Figure 55. Optimized structures of possible tautomers and rotamers of $HL^{py,ph}$.

Rotamer I-r is the most stable form, and the theoretical data obtained match well with the experimental behavior of the $HL^{py,Ph}$ proligand, both in solution and in the solid state. The calculated NMR spectrum of II correlates well with the experimental spectrum and, additionally, a good fit was found in the comparison of the structural parameters of the calculated $HL^{py,ph}$ molecule with those determined by X-ray crystallography (Figure 53). This confirms the appropriateness of the selected combination of method and basis sets. As previously noted for the related proligand $HL^{py,me}$,[84] the existence in tautomer II of an

intramolecular hydrogen bond (O-H···N, 1.781 Å) is the key stabilizing factor. Complexes **1**–**4** were also studied by DFT calculations. The selected combination of the method and basis sets provides a good structural description of these complexes based on the comparison of the calculated and experimental structural parameters of complex **3** (Table 4).

Table 4. Comparison of experimental and calculated data of complex 3

Bond distances (Å) and angles (º)	**Complex 3**	
	X-ray	**Calculated**
Ru-N	2.126	2.144
Ru-O	2.089	2.090
Ru-P	2.306	2.354
Ru-centroid	1.715	1.850
P-Ru-N	89.9	88.2
O-Ru-N	83.1	84.6
P-Ru-O	80.6	78.5

The resulting optimized structures (Figure 56) show the typical three-legged piano-stool structure, where $L^{py,ph}$ acts as a *N,O* bidentate ligand. The six-membered [Ru($L^{py,ph}$)] metallacycle in these complexes displays a half-chair conformation.

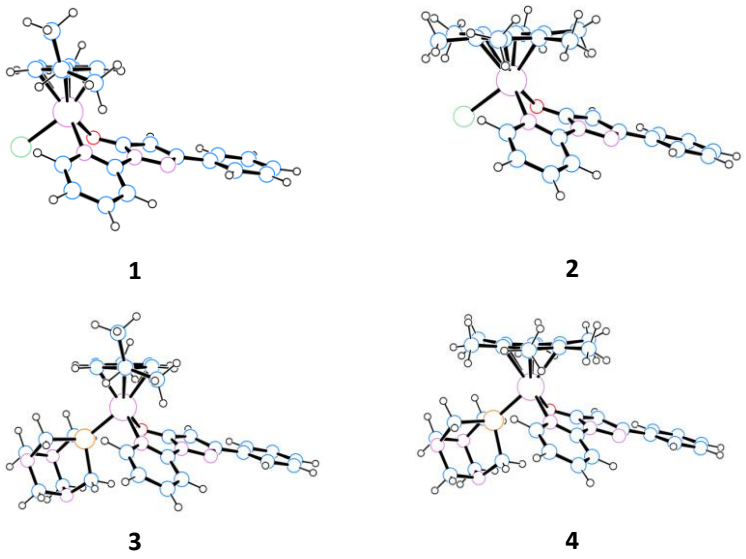

Figure 56. DFT Structure of Arene-Ru(II)$L^{py,ph}$ Complexes.

The angles between the pyrazolone plane and the plane defined by Ru and the N and O donor atoms are around 45º for **1** and **3** (*ca.* 48º in the X-ray structure) and 41º for **2** and **4**. To rationalize this difference, the structure of the anion $[L^{py,ph}]^-$ was also optimized. Two rotamers with similar energies were located, corresponding to the potential *N,O* or *N,N* bidentate ligands (Figure 57).

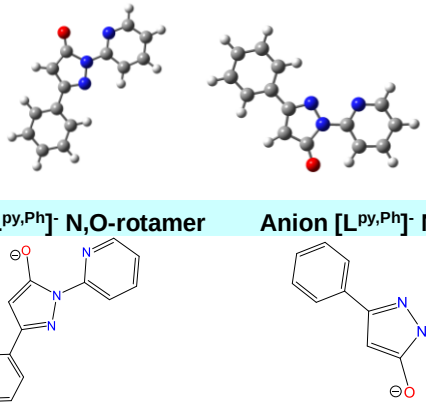

Anion $[L^{py,Ph}]^-$ N,O-rotamer	Anion $[L^{py,Ph}]^-$ N,N-rotamer

E	-779.237429190	-779.243261495
Eo	-779.027781000	-779.033238000
Et	-779.013987000	-779.019610000
H	-779.013043000	-779.018666000
G	-779.071051000	-779.075624000
ΔE	3.7	0.0
ΔG	2.9	0.0

Figure 57. Optimized structures and energies of the two rotamers of the anion $[L^{py,Ph}]^-$.

The deprotonation of tautomer II affords a C-O bond of 1.23 Å for the *N,O* rotamer. Upon coordination, this distance increases to approximately 1.29 Å (complexes **1** and **2**) and to around 1.31 Å (**3** and **4**), suggesting a bond order greater than one,[110] and delocalization along the [Ru($L^{py,ph}$)] metallacycle. These values agree with the observed decrease of the ν_{CO} vibration mode from neutral complexes **1** and **2** to cationic **3** and **4** discussed above. The MOs of $[L^{py,ph}]^-$ involved in the *in-plane N,O* coordination to the ruthenium center are HOMO-1, HOMO-4 and HOMO-6 (Figure 58), these being MOs in which the lone pairs of the donor N and O atoms participate in the *in-phase* and *out-of-phase* contributions of σ type that provide the M-O and M-N bonds in **1-4**. However, considering the conformation of the [Ru($L^{py,ph}$)] metallacycle, some supplementary contribution to the Ru-O bond comes from the π part of the HOMO of the ligand (Figure 58).

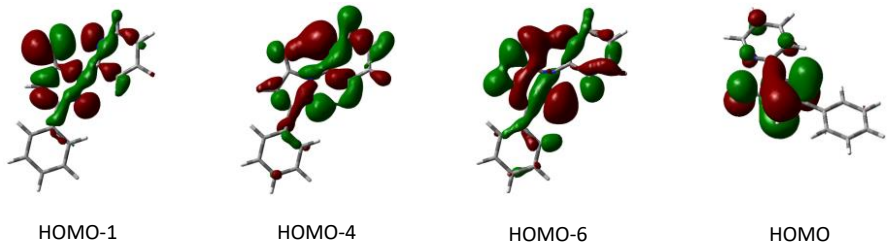

Figure 58. MOs of anionic ligand $[L^{py,ph}]^-$ involved in the N,O-coordination to Ru center.

Since the $[L^{py,ph}]^-$ ligand also exists as a *N,N* rotamer, the possible ruthenium isomers of **1-4** with the *N,N* bidentate ligand were also optimized (Figure 59). Surprisingly, despite the steric hindrance of the Ph substituent, the *N,N* isomers are not clearly destabilized, except for complex **4**.

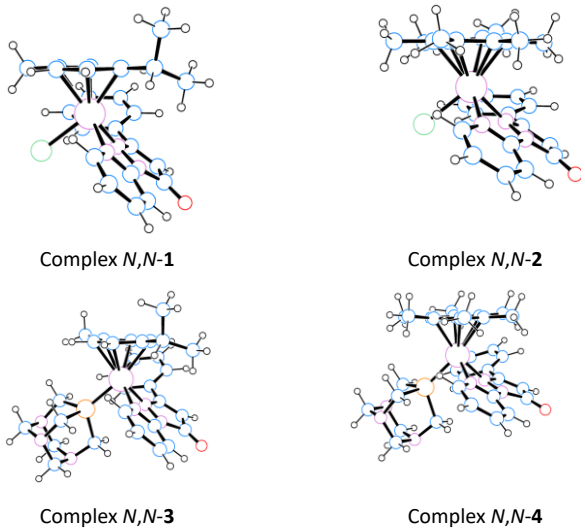

Figure 59. Optimized structures of N,N-isomers of complexes 1–4.

Table 5. Energies (Hartree) and relative ΔE and ΔG energies (kcal/mol) of complexes 1–4 and their N,N-isomers.

	1	***N,N*-isomer of 1**	**2**	***N,N*-isomer of 2**
E	-1722.617292900	-1722.626715480	-1801.251702930	-1801.252901320
Eo	-1722.184871000	-1722.194197000	-1800.763771000	-1800.764733000
Et	-1722.156913000	-1722.166200000	-1800.732125000	-1800.733109000
H	-1722.155969000	-1722.165256000	-1800.731180000	-1800.732165000
G	-1722.244938000	-1722.253101000	-1800.826761000	-1800.826221000
ΔE	0.0	-5.9	0.0	-0.8
ΔG	0.0	-5.1	0.0	0.3

	3	***N,N*-isomer of 3**	**4**	***N,N*-isomer of 4**
E	-2003.654991800	-2003.655069500	-2082.288046530	-2082.277708420
Eo	-2003.028853000	-2003.029079000	-2081.606406000	-2081.595429000
Et	-2002.993807000	-2002.993965000	-2081.567695000	-2081.556832000
H	-2002.992863000	-2002.993021000	-2081.566751000	-2081.555888000
G	-2003.096902000	-2003.095461000	-2081.677295000	-2081.664579000
ΔE	0.0	0.0	0.0	6.5
ΔG	0.0	0.9	0.0	8.0

This can be explained on the basis of a reinforcement of the Ru-X bonds in the *N,N* isomers that compensates for the steric pressure, which is observed in the calculated Mayer indexes for the Ru-X bonds. An increase in these indexes was observed for the *N,O* complexes compared to the *N,N* isomers (Table 5). On the basis of the similar relative energies shown in Table 5 for complexes **1** and **2** and their isomers, the *N,O* coordination is not clearly favored from a thermodynamic point of view. Hence, the formation of **1** and **2** is presumed to occur via a mechanism involving nucleophilic attack of the oxygen atom (Mulliken charge of -0.41) on the deprotonated $[L^{py,ph}]^-$ species toward the Ru center. Thus, the only possible bidentate coordination of the ligand involves the formation of the Ru-N

bond through the N_{py} atom. For comparison, complexes **5-8** were also analyzed by DFT calculations and similar three-legged piano-stool structures were observed in optimized molecules (Figure 60).

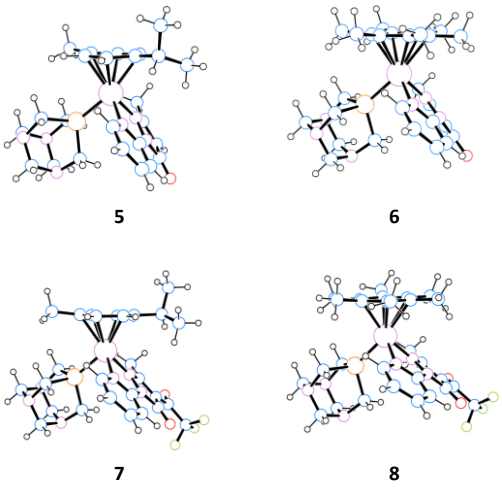

Figure 60. Optimized structures of the cations of complexes 5–8.

The C-O bond lengths (1.225 Å for **5** and **6** and 1.220 Å for **7** and **8**) are shorter than those observed for complexes **1-4** and, consequently, higher ν_{CO} frequencies were observed in agreement with the experimental IR spectra. These complexes are characterized by an HOMO constituted by a d_π ruthenium orbital that displays an antibonding combination with the π part of the L^{py} or $Q^{py,CF3}$ ligands (Figure 61). This situation is similar to that previously reported for the neutral counterparts, [Ru(arene)($L^{py,me}$)Cl] and [Ru(arene)($Q^{py,CF3}$)Cl].[84]

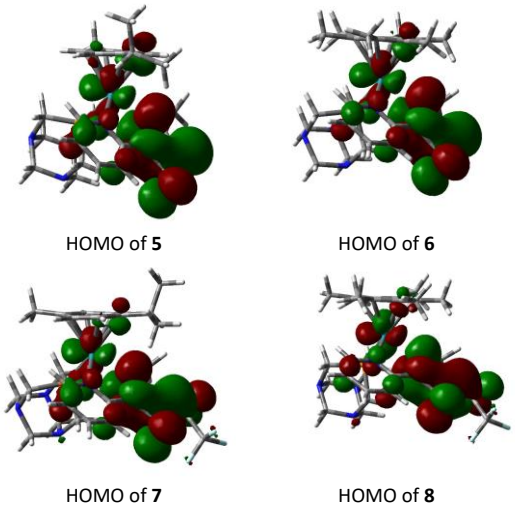

Figure 61. HOMOs of complexes 5–8

Cytotoxicity Studies

The cytotoxicity of the compounds was determined on the human ovarian carcinoma cell line (A2780) and its cisplatin resistant form (A780cis) as well as non-tumorigenic human embryonic kidney (HEK293T) cells over an incubation period of 72h using the MTT assay. The resulting IC_{50} values of the compounds are presented in Table 6 together with the values for cisplatin and Rapta-C used as positive and negative controls, respectively. The proligands are more potent than their corresponding complexes on the ovarian cell line A2780, most notably with $HL^{py,ph}$ with an IC_{50} =1.7 ± 0.5 µM which is ca. 5 - 15 fold lower than complexes **1** and **2**. In addition, cationic complexes **3** and **4**, resulting from the substitution of the chloride ligand in complexes **1** and **2** by PTA, are essentially inactive (IC_{50} >100 µM) on the three cell lines. A similar loss of cytotoxicity is observed with complexes **7** and **8** compared to their precursors [Ru(cym)($Q^{py,CF3}$)Cl] and [Ru(hmb)($Q^{py,CF3}$)Cl], respectively. In contrast, complexes **5** and **6** have a higher potency than [Ru(cym)($L^{py,me}$)Cl] and [Ru(hmb)($L^{py,me}$)Cl] with IC_{50} values of 36 ± 19 and 35 ± 7 µM , respectively. Interestingly, **5** displays one of the highest selectivity profiles, even compared to cisplatin, as it is inactive on the non-tumorigenic HEK293T cell line (IC_{50} >100 µM), while displaying an intermediate toxicity on the ovarian cancer cell line A2780.

Table 6. IC_{50} values (μM) of the compounds tested on human ovarian carcinoma (A2780), its cisplatin resistant form (A2780cis) and human embryonic kidney cells (HEK293t). Values are given as the mean obtained from 3 independent experiments ± standard deviation.

	A2780	A2780cis	HEK293T
$HL^{py,ph}$	1.7 ± 0.5	1.3 ± 0.4	8 ± 4.4
(1) [Ru(cym)($L^{py,ph}$)Cl]	30 ± 4	34 ± 6	26 ± 1
(2) [Ru(hmb)($L^{py,ph}$)Cl]	8.9 ± 1.8	7.4 ± 1.6	3.1 ± 1.8
(3) [Ru(cym)($L^{py,ph}$)PTA]BF_4	>100	>100	>100
(4) [Ru(hmb)($L^{py,ph}$)PTA]BF_4	>100	>100	>100
$HL^{py,me}$ [84]	9.1 ± 1.1	17.4 ± 1.7	14.9 ± 0.1
[Ru(cym)($L^{py,me}$)Cl] [84]	>100	>100	>100
[Ru(hmb)($L^{py,me}$)Cl] [84]	>100	>100	>100
(5) [Ru(cym)($L^{py,me}$)PTA]BF_4	36 ± 19	>100	>100
(6) [Ru(hmb)($L^{py,me}$)PTA]BF_4	35 ± 7	28 ± 3	33 ± 6
$HQ^{py,CF3}$ [84]	8.9 ± 0.5	10.4 ± 2.6	12.9 ± 0.3
[Ru(cym)($Q^{py,CF3}$)Cl] [84]	20.6 ± 2.1	25.2 ± 1.1	24.2 ± 6.6
[Ru(hmb)($Q^{py,CF3}$)Cl] [84]	14.8 ± 3.0	9.0 ± 3.0	6.9 ± 1.8
(7) [Ru(cym)($Q^{py,CF3}$)PTA]PF_6	>100	>100	>100
(8) [Ru(hmb)($Q^{py,CF3}$)PTA]PF_6	>100	>100	>100
Cisplatin	0.9 ± 0.2	6.7± 4	2.2 ± 0.8
Rapta-C	>200	>200	>200

Conclusion

In this study we have shown that in pyrazolone ligands containing a pyridine ring, the presence of a phenyl in position 3 of the pyrazole ring in $HL^{py,ph}$ in place of a methyl as in $HL^{py,me}$ induces electronic and structural changes that determine the preference for a bidentate N,O-coordination, instead of the N,N-coordination observed in ruthenium complexes with $HL^{py,me}$. The presence of an acyl moiety in the ligand $HQ^{py,CF3}$ also leads to a preference for an N,N-chelated coordination. For complexes 1 and 2 the N,O coordination is not clearly thermodynamically favored, according to DFT studies, and their formation maybe occurs via a mechanism involving nucleophilic attack of the oxygen atom in the deprotonated $[L^{py,ph}]^-$ ligand toward the Ru center. DFT results rationalize the isolation of $HL^{py,ph}$ as the most stable enol tautomer I in the form of rotamer I-r and

describes well the structures of Ru-complexes. These theoretical studies support the spectroscopic assignments (IR and NMR) and, based on the MO analyses of these ligands, provide explanation about their coordination to the Ru center. Anticancer studies performed against A2780, A2780cis, and nontumor HEK293T unexpectedly showed the proligands being more efficient than their corresponding ruthenium complexes. Introduction of a PTA ligand brings the formation of cationic complexes, which are however less active than neutral parents with chloride or completely inactive. In any case, the ligand $HL^{py,ph}$ is quite interesting, being more potent and selective than Cisplatin, and this result may open further developments by exploring the coordination chemistry of such ligand toward other metal acceptors.

References

(50) Abu-Surrah, A. S.; Kettunen, M. Platinum Group Antitumor Chemistry: Design and Development of New Anticancer Drugs Complementary to Cisplatin. *Current medicinal chemistry* **2006**, *13* (11), 1337–1357. DOI: 10.2174/092986706776872970

(51) Rabik, C. A.; Dolan, M. E. Molecular Mechanisms of Resistance and Toxicity Associated with Platinating Agents. *Cancer treatment reviews* **2007**, *33* (1), 9–23. DOI: 10.1016/j.ctrv.2006.09.006

(52) Boulikas, T.; Stathopoulos, G. P.; Volakakis, N.; Vougiouka, M. Systemic Lipoplatin Infusion Results in Preferential Tumor Uptake in Human Studies. *Anticancer Research* **2005**, *25* (4), 3031–3039. PMID: 16080562.

(53) Ott, I.; Gust, R. Non Platinum Metal Complexes as Anti-cancer Drugs. *Archiv der Pharmazie: An International Journal Pharmaceutical and Medicinal Chemistry* **2007**, *340* (3), 117–126. DOI: 10.1002/ardp.200600151

(54) Muhammad, N.; Guo, Z. Metal-Based Anticancer Chemotherapeutic Agents. *Current opinion in chemical biology* **2014**, *19*, 144–153. DOI: 10.1016/j.cbpa.2014.02.003.

(55) Meier-Menches, S. M.; Gerner, C.; Berger, W.; Hartinger, C. G.; Keppler, B. K. Structure–Activity Relationships for Ruthenium and Osmium Anticancer Agents – towards Clinical Development. *Chem. Soc. Rev.* **2018**, *47* (3), 909–928. DOI: 10.1039/C7CS00332C.

(56) Bergamo, A.; Sava, G. Ruthenium Complexes Can Target Determinants of Tumour Malignancy. *Dalton Transactions* **2007**, No. 13, 1267–1272. DOI: 10.1039/B617769G

(57) Hartinger, C. G.; Jakupec, M. A.; Zorbas-Seifried, S.; Groessl, M.; Egger, A.; Berger, W.; Zorbas, H.; Dyson, P. J.; Keppler, B. K. KP1019, a New Redox-active Anticancer Agent–Preclinical Development and Results of a Clinical Phase I Study in Tumor Patients. *Chemistry & biodiversity* **2008**, *5* (10), 2140–2155. DOI: 10.1002/cbdv.200890195

(58) Lentz, F.; Drescher, A.; Lindauer, A.; Henke, M.; Hilger, R. A.; Hartinger, C. G.; Scheulen, M. E.; Dittrich, C.; Keppler, B. K.; Jaehde, U. Pharmacokinetics of a Novel Anticancer Ruthenium Complex (KP1019, FFC14A) in a Phase I Dose-Escalation Study. *Anti-cancer drugs* **2009**, *20* (2), 97–103. DOI: 10.1097/CAD.0b013e328322fbc5

(59) Kapitza, S.; Pongratz, M.; Jakupec, M. A.; Heffeter, P.; Berger, W.; Lackinger, L.; Keppler, B. K.; Marian, B. Heterocyclic Complexes of Ruthenium (III) Induce Apoptosis in Colorectal Carcinoma Cells. *Journal of cancer research and clinical oncology* **2005**, *131*, 101–110. DOI: 10.1007/s00432-004-0617-0.

(60) Casini, A.; Temperini, C.; Gabbiani, C.; Supuran, C. T.; Messori, L. The X-ray Structure of the Adduct between NAMI-A and Carbonic Anhydrase Provides Insights into the Reactivity of This Metallodrug with Proteins. *ChemMedChem* **2010**, *5* (12), 1989–1994. DOI: 10.1002/cmdc.201000331.

(61) Sava, G.; Gagliardi, R.; Cocchietto, M.; Clerici, K.; Capozzi, I.; Marrella, M.; Alessio, E.; Mestroni, G.; Milanino, R. Comparison of the Effects of the Antimetastatic Compound ImH [Trans-RuCl 4 (DMSO) Im](NAMI-A) on the Arthritic Rat and on MCa Mammary Carcinoma in Mice. *Pathology & Oncology Research* **1998**, *4*, 30–36. DOI: 10.1007/BF02904692

(62) Rademaker-Lakhai, J. M.; Van Den Bongard, D.; Pluim, D.; Beijnen, J. H.; Schellens, J. H. A Phase I and Pharmacological Study with Imidazolium-Trans-DMSO-Imidazole-Tetrachlororuthenate, a Novel Ruthenium Anticancer Agent. *Clinical Cancer Research* **2004**, *10* (11), 3717–3727. DOI: 10.1158/1078-0432.CCR-03-0746.

(63) Leijen, S.; Burgers, S. A.; Baas, P.; Pluim, D.; Tibben, M.; van Werkhoven, E.; Alessio, E.; Sava, G.; Beijnen, J. H.; Schellens, J. H. Phase I/II Study with Ruthenium Compound NAMI-A and Gemcitabine in Patients with Non-Small Cell Lung Cancer after First Line Therapy. *Investigational new drugs* **2015**, *33*, 201–214. DOI: 10.1007/s10637-014-0179-1.

(64) Monti-Bragadin, C.; Ramani, L.; Samer, L.; Mestroni, G.; Zassinovich, G. Effects of Cis-Dichlorodiammineplatinum (II) and Related Transition Metal Complexes on Escherichia Coli. *Antimicrobial agents and chemotherapy* **1975**, *7* (6), 825–827. DOI: 10.1128/AAC.7.6.825.

(65) Alessio, E.; Mestroni, G.; Nardin, G.; Attia, W. M.; Calligaris, M.; Sava, G.; Zorzet, S. Cis-and Trans-Dihalotetrakis (Dimethyl Sulfoxide) Ruthenium (II) Complexes (RuX2 (DMSO) 4; X= Cl, Br): Synthesis, Structure, and Antitumor Activity. *Inorganic chemistry* **1988**, *27* (23), 4099–4106. DOI: 10.1021/ic00296a006.

(66) Murray, B. S.; Babak, M. V.; Hartinger, C. G.; Dyson, P. J. The Development of RAPTA Compounds for the Treatment of Tumors. *Coordination Chemistry Reviews* **2016**, *306*, 86–114. DOI: 10.1016/j.ccr.2015.06.014.

(67) Morris, R. E.; Aird, R. E.; Del Socorro Murdoch, P.; Chen, H.; Cummings, J.; Hughes, N. D.; Parsons, S.; Parkin, A.; Boyd, G.; Jodrell, D. I.; Sadler, P. J. Inhibition of Cancer Cell Growth by Ruthenium(II) Arene Complexes. *J. Med. Chem.* **2001**, *44* (22), 3616–3621. DOI: 10.1021/jm010051m.

(68) Yan, Y. K.; Melchart, M.; Habtemariam, A.; Sadler, P. J. Organometallic Chemistry, Biology and Medicine: Ruthenium Arene Anticancer Complexes. *Chemical communications* **2005**, No. 38, 4764–4776. DOI: 10.1039/b508531b.

(69) Allardyce, C. S.; Dyson, P. J. Ruthenium in Medicine: Current Clinical Uses and Future Prospects. *Platinum Metals Review* **2001**, *45* (2), 62–69.

(70) Phillips, A. D.; Gonsalvi, L.; Romerosa, A.; Vizza, F.; Peruzzini, M. Coordination Chemistry of 1, 3, 5-Triaza-7-Phosphaadamantane (PTA): Transition Metal Complexes and Related Catalytic, Medicinal and Photoluminescent Applications. *Coordination chemistry reviews* **2004**, *248* (11–12), 955–993. DOI: 10.1016/j.ccr.2004.03.010.

(71) Dorcier, A.; Ang, W. H.; Bolano, S.; Gonsalvi, L.; Juillerat-Jeannerat, L.; Laurenczy, G.; Peruzzini, M.; Phillips, A. D.; Zanobini, F.; Dyson, P. J. In Vitro Evaluation of Rhodium and Osmium RAPTA Analogues: The Case for Organometallic Anticancer Drugs Not Based on Ruthenium. *Organometallics* **2006**, *25* (17), 4090–4096. DOI: 10.1021/om060394o.

(72) Scolaro, C.; Hartinger, C. G.; Allardyce, C. S.; Keppler, B. K.; Dyson, P. J. Hydrolysis Study of the Bifunctional Antitumour Compound RAPTA-C,[Ru (H6-p-Cymene) Cl2 (Pta)]. *Journal of inorganic biochemistry* **2008**, *102* (9), 1743–1748. DOI: 10.1016/j.jinorgbio.2008.05.004.

(73) Gossens, C.; Dorcier, A.; Dyson, P. J.; Rothlisberger, U. P K a Estimation of Ruthenium (II)− Arene PTA Complexes and Their Hydrolysis Products via a DFT/Continuum Electrostatics Approach. *Organometallics* **2007**, *26* (16), 3969–3975. DOI: 10.1021/om700364s

(74) Scolaro, C.; Bergamo, A.; Brescacin, L.; Delfino, R.; Cocchietto, M.; Laurenczy, G.; Geldbach, T. J.; Sava, G.; Dyson, P. J. In Vitro and in Vivo Evaluation of Ruthenium(II)−Arene PTA Complexes. *J. Med. Chem.* **2005**, *48* (12), 4161–4171. DOI: 10.1021/jm050015d.

(75) Bergamo, A.; Masi, A.; Dyson, P. J.; Sava, G. Modulation of the Metastatic Progression of Breast Cancer with an Organometallic Ruthenium Compound. *Int J Oncol* **2008**. DOI: 10.3892/ijo_00000119.

(76) Faria, J. V.; Vegi, P. F.; Miguita, A. G. C.; Santos, M. S. dos; Boechat, N.; Bernardino, A. M. R. Recently Reported Biological Activities of

Pyrazole Compounds. *Bioorganic & Medicinal Chemistry* **2017**, *25* (21), 5891–5903. DOI: 10.1016/j.bmc.2017.09.035.

(77) Liu, S.; Bao, X.; Wang, B. Pyrazolone: A Powerful Synthon for Asymmetric Diverse Derivatizations. *Chem. Commun.* **2018**, *54* (82), 11515–11529. DOI: 10.1039/C8CC06196C.

(78) Marchetti, F.; Pettinari, C.; Nicola, C. D.; Tombesi, A.; Pettinari, R. Coordination Chemistry of Pyrazolone-Based Ligands and Applications of Their Metal Complexes. *Coordination Chemistry Reviews* **2019**, *401*, 213069. DOI: 10.1016/j.ccr.2019.213069.

(79) Bhandari, R.; Kuhad, A.; Kuhad, A. Edaravone: A New Hope for Deadly Amyotrophic Lateral Sclerosis. *Drugs of today (Barcelona, Spain : 1998)* **2018**, *54* (6), 349—360. DOI: 10.1358/dot.2018.54.6.2828189.

(80) Cruz, M. P. Edaravone (Radicava): A Novel Neuroprotective Agent for the Treatment of Amyotrophic Lateral Sclerosis. **2018** Jan; 43 (1), 25-28. PMID: 29290672; PMCID: PMC5737249.

(81) Jaiswal, M. K. Riluzole and Edaravone: A Tale of Two Amyotrophic Lateral Sclerosis Drugs. *Medicinal Research Reviews* **2019**, *39* (2), 733–748. DOI: 10.1002/med.21528.

(82) Pettinari, R.; Marchetti, F.; Di Nicola, C.; Pettinari, C. Half-Sandwich Metal Complexes with β-Diketone-Like Ligands and Their Anticancer Activity. *Eur J Inorg Chem* **2018**, *2018* (31), 3521–3536. DOI: 10.1002/ejic.201800400.

(83) Cingolani, A.; Effendy; Marchetti, F.; Pettinari, C.; Pettinari, R.; Skelton, B. W.; White, A. H. Silver Coordination Chemistry of a New Versatile "Janus"-Type N_2,O_2-Bichelating Donor, Formation of an Unprecedented Supramolecular Network of Binuclear Silver Building Blocks Containing a Five-Coordinate β-Diketonate, and Isolation of Unexpected Silver−Tin−Silver Heterotrimetallic Complexes from Silver Metathesis Reactions. *Inorg. Chem.* **2004**, *43* (14), 4387–4399. DOI: 10.1021/ic0497376.

(84) Pettinari, R.; Marchetti, F.; Tombesi, A.; Di Nicola, C.; Pettinari, C.; Guo, C.; Zhang, Z.; Galindo, A.; Fadaei-Tirani, F.; Hadiji, M. Arene-Ruthenium (II) Complexes with Pyrazole-Based Ligands Bearing a

Pyridine Moiety: Synthesis, Structure, DFT Calculations, and Cytotoxicity. *Inorg. Chim. Acta* **2021**, *528*, 120610. DOI: 10.1016/j.ica.2021.120610

(85) Basaif, S. A.; Hassan, M. A.; Gobouri, A. A. AlCl3-Catalyzed Diazocoupling of 1-(Aryl/Hetaryl)-3-Phenyl-1H-Pyrazol-2-in-5-Ones in Aqueous Medium. Synthesis of Hetaryl-Azopyrazolones and Their Application as Disperse Dyes. *Dyes and Pigments* **2007**, *72* (3), 387–391. DOI: 10.1016/j.dyepig.2005.09.025.

(86) Huang, Y.-Y.; Lin, H.-C.; Cheng, K.-M.; Su, W.-N.; Sung, K.-C.; Lin, T.-P.; Huang, J.-J.; Lin, S.-K.; Wong, F. F. Efficient Di-Bromination of 5-Pyrazolones and 5-Hydroxypyrazoles by N-Bromobenzamide. *Tetrahedron* **2009**, *65* (46), 9592–9597. DOI: 10.1016/j.tet.2009.09.055.

(87) Cho, J.; Sadu, V. S.; Han, Y.; Bae, Y.; Lee, H.; Lee, K.-I. Structural Requirements of 1-(2-Pyridinyl)-5-Pyrazolones for Disproportionation of Boronic Acids. *Molecules* **2021**, *26* (22). DOI: 10.3390/molecules26226814.

(88) McFerrin, C. A.; Hammer, R. P.; Fronczek, F. R.; Watkins, S. F. 3-Phenyl-1-(2-Pyrid\-Yl)-1ıt H-Pyrazol-5-Ol. *Acta Crystallographica Section E* **2006**, *62* (6), o2518–o2519. DOI: 10.1107/S1600536806019027.

(89) Steel, T. R.; Hartinger, C. G. Metalloproteomics for Molecular Target Identification of Protein-Binding Anticancer Metallodrugs. *Metallomics* **2020**, *12* (11), 1627–1636. DOI: 10.1039/d0mt00196a.

(90) CrysAlisPro Software System; Rigaku Oxford Difraction. **2021**.

(91) Sheldrick, G. M. It SHELXT – Integrated Space-Group and Crystal-Structure Determination. *Acta Crystallographica Section A* **2015**, *71* (1), 3–8. DOI: 10.1107/S2053273314026370.

(92) Sheldrick, G. M. Crystal Structure Refinement with It SHELXL. *Acta Crystallographica Section C* **2015**, *71* (1), 3–8. DOI: 10.1107/S2053229614024218.

(93) Dolomanov, O. V.; Bourhis, L. J.; Gildea, R. J.; Howard, J. A. K.; Puschmann, H. It OLEX2: A Complete Structure Solution, Refinement and Analysis Program. *Journal of Applied*

Crystallography **2009**, *42* (2), 339–341. DOI: 10.1107/S0021889808042726.

(94) Becke, A. D. Density-functional Thermochemistry. I. The Effect of the Exchange-only Gradient Correction. *The Journal of Chemical Physics* **1992**, *96* (3), 2155–2160. DOI: 10.1063/1.462066.

(95) Lee, C.; Yang, W.; Parr, R. G. Development of the Colle-Salvetti Correlation-Energy Formula into a Functional of the Electron Density. *Phys. Rev. B* **1988**, *37* (2), 785–789. DOI: 10.1103/PhysRevB.37.785.

(96) Hay, P. J.; Wadt, W. R. Ab Initio Effective Core Potentials for Molecular Calculations. Potentials for K to Au Including the Outermost Core Orbitals. *The Journal of Chemical Physics* **1985**, *82* (1), 299–310. DOI: 10.1063/1.448975.

(97) Wong, M. W. Vibrational Frequency Prediction Using Density Functional Theory. *Chemical Physics Letters* **1996**, *256* (4), 391–399. DOI: 10.1016/0009-2614(96)00483-6.

(98) Scott, A. P.; Radom, L. Harmonic Vibrational Frequencies: An Evaluation of Hartree−Fock, Møller−Plesset, Quadratic Configuration Interaction, Density Functional Theory, and Semiempirical Scale Factors. *J. Phys. Chem.* **1996**, *100* (41), 16502–16513. DOI: 10.1021/jp960976r.

(99) Frisch, M. J.; Trucks, G. W.; Schlegel, H. B.; Scuseria, G. E.; Robb, M. A.; Cheeseman, J. R.; Scalmani, G.; Barone, V.; Petersson, G.; Nakatsuji, H. Gaussian, Inc., Wallingford CT, 2016. *Gaussian09, Revision D* **2016**, *1*.

(100) Geary, W. J. The Use of Conductivity Measurements in Organic Solvents for the Characterisation of Coordination Compounds. *Coordination Chemistry Reviews* **1971**, *7* (1), 81–122. DOI: 10.1016/S0010-8545(00)80009-0.

(101) Palmucci, J.; Marchetti, F.; Pettinari, R.; Pettinari, C.; Scopelliti, R.; Riedel, T.; Therrien, B.; Galindo, A.; Dyson, P. J. Synthesis, Structure, and Anticancer Activity of Arene–Ruthenium(II) Complexes with Acylpyrazolones Bearing Aliphatic Groups in the Acyl Moiety. *Inorg. Chem.* **2016**, *55* (22), 11770–11781. DOI: 10.1021/acs.inorgchem.6b01861.

(102)Marchetti, F.; Pettinari, R.; Di Nicola, C.; Pettinari, C.; Palmucci, J.; Scopelliti, R.; Riedel, T.; Therrien, B.; Galindo, A.; Dyson, P. J. Synthesis, Characterization and Cytotoxicity of Arene–Ruthenium(II) Complexes with Acylpyrazolones Functionalized with Aromatic Groups in the Acyl Moiety. *Dalton Trans.* **2018**, *47* (3), 868–878. DOI: 10.1039/C7DT04249C.

(103)Meier-Menches, S. M.; Gerner, C.; Berger, W.; Hartinger, C. G.; Keppler, B. K. Structure–Activity Relationships for Ruthenium and Osmium Anticancer Agents–towards Clinical Development. *Chemical Society Reviews* **2018**, *47* (3), 909–928. DOI: 10.1039/C7CS00332C

(104)Pettinari, R.; Pettinari, C.; Marchetti, F.; Skelton, B. W.; White, A. H.; Bonfili, L.; Cuccioloni, M.; Mozzicafreddo, M.; Cecarini, V.; Angeletti, M.; Nabissi, M.; Eleuteri, A. M. Arene–Ruthenium(II) Acylpyrazolonato Complexes: Apoptosis-Promoting Effects on Human Cancer Cells. *J. Med. Chem.* **2014**, *57* (11), 4532–4542. DOI: 10.1021/jm500458c.

(105)Rosenthal, M. R. The Myth of the Non-Coordinating Anion. *Journal of Chemical Education* **1973**, *50* (5), 331. DOI: 10.1021/ed050p331

(106)Bennett, M.; Matheson, T. W.; Robertson, G. B.; Smith, A. K.; Tucker, P. A. Highly Fluxional Arene Cyclooctatetraene Complexes of Zerovalent Iron, Ruthenium, and Osmium. Single-Crystal x-Ray Study of (Cyclooctatetraene)(Hexamethylbenzene) Ruthenium (0), Ru (. Eta. 6HMB)(1-4-. Eta.-COT). *Inorganic Chemistry* **1980**, *19* (4), 1014–1021. DOI: 10.1021/ic50206a045

(107)Pietracci, L.; Pettinari, R.; Tombesi, A.; Marchetti, F.; Pettinari, C.; Galindo, A.; Fadaei-Tirani, F.; Hadiji, M.; Dyson, P. J. Steric and Electronic Effects Responsible for *N* , *O* - or *N* , *N* -Chelating Coordination of Pyrazolones Containing a Pyridine Ring in Ruthenium Arene Systems. *Organometallics* **2023**, *42* (13), 1495–1504. DOI: 10.1021/acs.organomet.3c00121.

(108)Collong, W.; Kruck, T. Mitteilungen Über Metalltrifluorphosphan-Komplexe, 51. Hexakis (Trifluorphosphan) Vanadium (0)-Synthese,

Eigenschaften Und Reaktionen. *Chemische Berichte* **1990**, *123* (8), 1655–1656.

(109)Kruck, T. Trifluorophosphine Complexes of Transition Metals. *Angewandte Chemie International Edition in English* **1967**, *6* (1), 53–67. DOI: 10.1016/S0898-8838(08)60249-4

(110)Cordero, B.; Gómez, V.; Platero-Prats, A. E.; Revés, M.; Echeverría, J.; Cremades, E.; Barragán, F.; Alvarez, S. Covalent Radii Revisited. *Dalton Transactions* **2008**, No. 21, 2832–2838. DOI: 10.1039/B801115J

Silver (I) Coordination Polymers as Chemoresistant sensors

Introduction

Chemoresistant sensors based on Ag(I) coordination polymers were prepared using a polyvinylidenefluoride support, with the addition of the ionic liquid 1-ethyl-3-methylimidazolium tetrafluoroborate to promote the passage of electricity, and deposited on plastic slides containing silver electrodes. The final goal of this investigation is the application of these sensors to the determination of volatile products of fruits fermentation, in particular ethylene. Their resistance was tested in the presence of different VOCs in different concentration in ppm, and in presence of fruit during their maturation period. The gases tested were ethylene, acetaldehyde, ethyl acetate, methanol, ethanol and final, the influence of relative humidity was measured. Results of Response % were obtained at 25ºC and as reference was utilized air. The final results consist in different behavior of Ag(I) sensors in presence of alcohols, with which the electrical resistance goes down, while with other gases it enhances. It is possible to explain it, considering the reducing and oxidizing nature of gases, and the structures of Ag(I) coordination polymers (Figure 62), which present aromatic systems with inter- and intra-molecular π-π interactions, that favor also the alignment of metal centers. These characteristics make Ag(I) CPs good conductors.

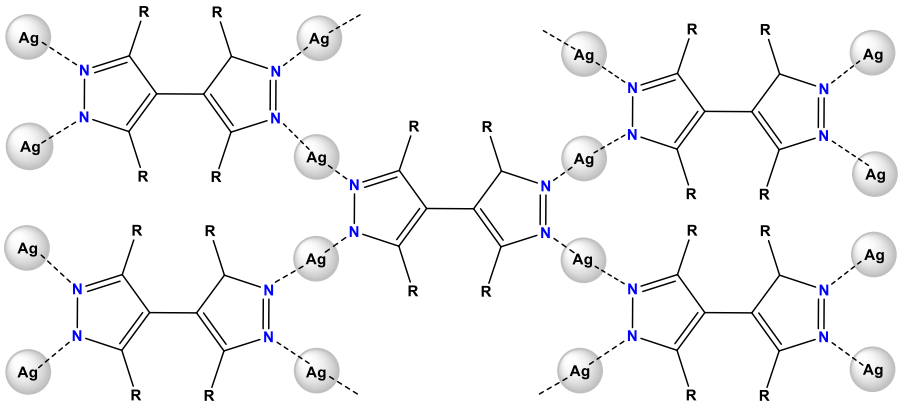

Figure 62. Ag CPs general structure with bispyrazolato-based ligands.

Ag (I) Coordination Polymers

In recent studies, silver (I)-based coordination polymers objects of this work have been tested as anti-microbial agents with good results, but their varied characteristics make them interesting for other applications as well. They are indicated as Ag_2BPZ, Ag_2Me_4BPZ, Ag_2Et_4BPZ, Ag_2Me_2BPZ (that is a MOF) and Ag_2Me_2PhBPZ (Figure 63 a, b, c, d and e).

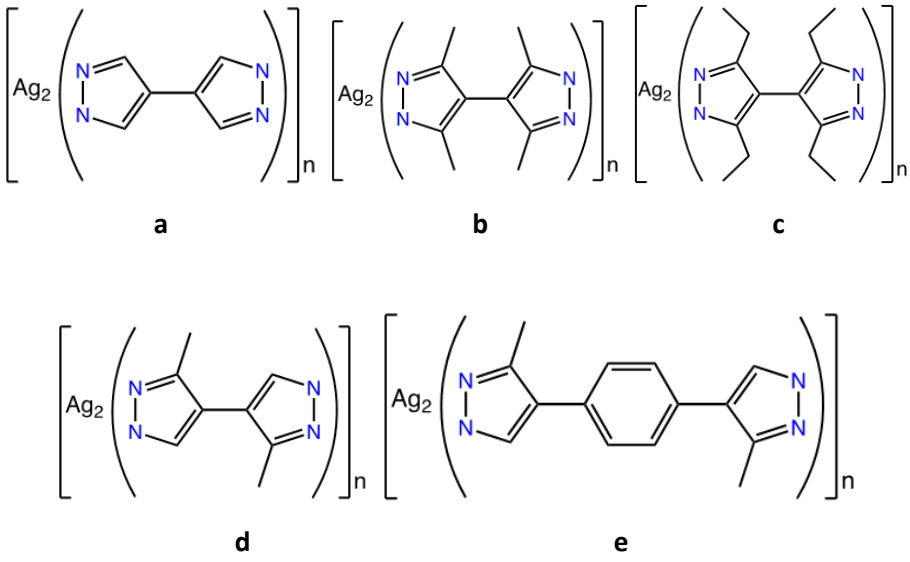

Figure 63. Ag(I) CPs of this work: a) Ag_2BPZ b) Ag_2Me_4BPZ c) Ag_2Et_4BPZ d) Ag_2Me_2BPZ e) Ag_2Me_2PhBPZ

In fact, they are fascinating not only for their structural diversity but above all for their chemical and physical characteristics. Usually, silver (I) CPs have applications such as conducting materials, therapeutic agents, luminescent materials, absorption, supramolecular chirality and many others.[111] Generally, the coordination polymers of silver (I) in fact exhibit luminescent capabilities, given that in many cases Ag···Ag interactions exist thanks to strong or weak bonds that are shorter than the sum of the Van der Waals radii of the two atoms of Ag. Ag···Ag interactions often contribute to the luminescence of Ag^+ CPs. On the other part, the coordination of the Ag^+ ion is able to modify the wavelength of organic molecules, in this way the choice of organic binders can lead to the construction of photo- or electroluminescent materials. In general, CPs of Ag(I) can show an emission band with n→π, π→π* intraligand transitions or ligand-to-metal charge transfer (LMCT) transitions.[112–114]

In a work of 2012, it was reported that the CP indicated as Ag_2BPZ as important photoluminescence. Its excitation occurs at 330 nm, with a green-yellow emission light at 520-522 nm.[115] In a work of 2007, Jie-Peng Zhang et al. reported the ability of Ag_2Me_4BPZ to adsorb small molecules such as CO_2 and also very large molecules such as benzene and toluene, thanks to the MOF pore flexibility.[116] This is an important feature in using these materials as sensors.

Silver(I) CPs with electrical conductivity have attracted much interest in recent years. Coordination polymers with the following characteristics can have electrical conductivity:

1. Ag···Ag interactions imparting temperature-dependent or independent electrical conductivity to CPs;[117–120]
2. Presence of polyenes and π-conjugated polycyclic aromatic hydrocarbons.

In Figure 64 Ag_2BPZ X-Ray structure is shown. It is possible to see in Fig. 64b the alignment of Ag(I) metal center (pink ball).

CPs with either of these characteristics exhibit electrical conductivity due to the delocalized π bonds that provide a gateway for the transfer of electrons between two metal centers along these bridging ligands. For this

reason, stacking of aromatic molecules with strong intra- and intermolecular π-π interactions provide high conductivity.[121,122]

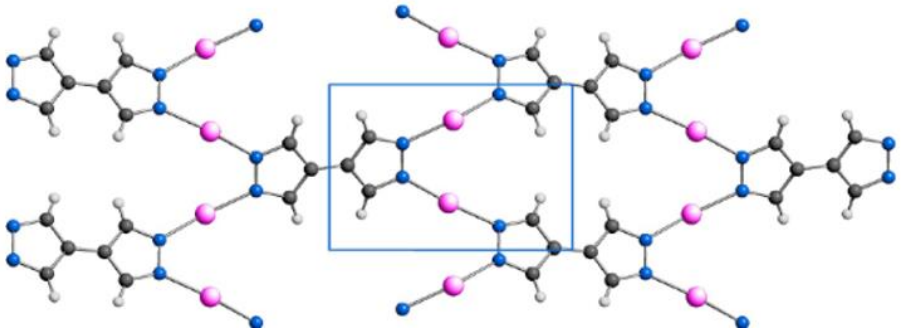

a

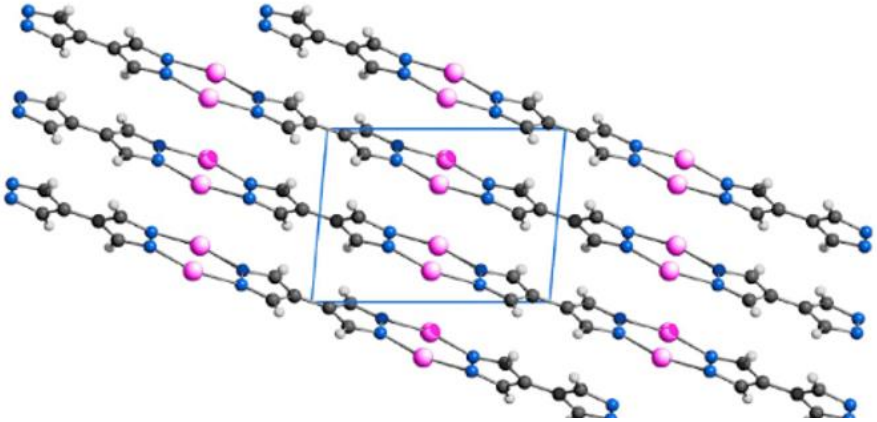

b

Figure 64. X-Ray Structure of Ag_2BPZ a) 2D horizontal section; b) 2D vertical section.

Chemical Sensors

In this work we will investigate the application of these silver (I)-based coordination polymers with bipyrazole ligands as sensors for the revelation of VOC produced by maturation of fruits and vegetables, such as ethylene, ethanol, acetaldehyde and ethyl acetate.

Sensors are systems capable of interacting with substances that are present in the surrounding environment, thus detecting their presence by sending a signal that can be optical, electrical, spectroscopical, etc. There are therefore various types of sensors, which are classified according to the

type of response they give when they interact with the analytes to be detected. Luminescent sensors are materials that change their luminescence when binding to target analytes. Chemoresistant sensors change the electrical resistance as they interact with VOCs. Colorimetric sensors change optical properties upon interaction with VOCs, and finally electrochemiluminescent sensors are chemiluminescent systems which are triggered by electrochemical processes. Surface-Enhanced- Raman-Scattering (SERS) sensors are based on the use of Raman spectroscopy, a technology using inelastic light scattering, which can provide the molecular "fingerprint-like" spectrum of the measured analyte according to its features in terms of vibrational frequency and intensity.[123]

The goal of this work is to evaluate the ability of silver(I)-based polymeric materials to be used as chemoresistant sensors. The gas sensing property of the sensors widely depends on the surface structure of the sensing material and the synthesis method. The electrical conductivity, and therefore the resistance of a material, depends on its chemical-physical characteristics, such as the chemical composition, the structure, the crystallographic form and the size of the crystallites, the dispersion and diffusion of the particles of the Ag(I) polymer, as well as the presence of surface defects.[124–126]

Moreover, redox reactions that occur on the surface, or in the pores, of the materials, can deeply influence the electrical conductivity. Another important parameter is the sensitivity of sensors, which is calculated as Ra/Rg for reducing gases, and as Rg/Ra for oxidant gases, respectively, when Ra > Rg and when Rg > Ra. Ra is the resistance of sensors in air and Rg is its resistance in presence of VOC target.[125,127]

It has been proved that MOFs and CPs can be used as a support for graphene in the fabrication of chemoresistant sensors to detect gaseous products of human exhalations, in order to determine the health status of people. These gases are essentially short chain alcohols, N_2, CO_2, CO, acetone, isoprene, NH_3, toluene, H_2O.[128]

Chemoresistant sensors are generally very cheap, easy to prepare and with excellent sensitivity and selectivity for various VOCs. The CPs object of this work have good electrical conductivity with the presence of a

supporting polymer, the polyvinylidene fluoride (PVDF), and an ionic liquid such as 1-ethyl-3-methylimidazolium tetrafluoroborate to favor the conductivity.

Experimental

Synthesis and characterization of Ag(I) CPs

Materials and methods

All reagents and chemicals used in the syntheses were purchased from commercial suppliers and used without further purification. FT-IR spectra were obtained from 4000 to 400 cm-1 or from 4000 to 700 cm^{-1} with the PerkinElmer Spectrum One System instrument. The elementary analyses (C, H, N) were carried out with a Fisons Instruments 1108 CHNS-O analyser. The thermogravimetric analyses were carried out in N_2 with a 10 min C heating ramp on a PerkinElmer Thermal Analyzer (STA) 6000.

[Ag_2(BPZ)] ***(1)***

Synthesis procedure[129] is as follows: to a solution of Ag_2O (0.4 mmols, 91.92 mg) in aqueous ammonia (28 %), 20 ml of MeOH and 1 ml of mesitylene is added slowly to a solution of H_2BPZ (0.4 mmols, 53.62 mg) dissolved in 20 ml of MeOH, the reaction mixture is left to stir for 1 day. The precipitate formed is filtered and washed 6 to 8 times with 10 ml MeOH so that all mesitylene is removed. Air dry the mixture for 3-4 h. 87.40 mg were obtained, with a yield corresponding to 63 %. Compound 1 is insoluble in dimethyl sulfoxide (DMSO), alcohols, acetone, acetonitrile (CH_3CN), chlorinated solvents and water. Elemental analysis for $Ag_2[C_6H_4N_4]$: H, 1.16; C, 20.72; N, 16.11. Found: H, 1.17; C, 20.94; N, 16.43. FT-IR (cm^{-1}): 3109 (m) ν(C−$H_{aromatic}$), 1678 (wbr), 1510 (m) ν(C=C + C=N), 1375 (s), 1312 (w), 1272 (s), 1161 (s), 1147 (m), 1041 (s), 1001 (w), 917 (m), 844 (s), 832 (s), 637 (s). TGA (heating from 30 ºC to 650 ºC, heating rate 10 ºC/min in nitrogen flow 30 ml/min): thermal

stability up to 340 ºC and progressive degradation with 68 % grey-black residue.

[Ag_2(Me_2BPZ)] ***(2)***

Synthesis was performed in a similar way to the synthesis of compound 1, using 0.4 mmols of H_2Me_2BPZ (64.84 mg), 0.4 mmols of Ag_2O (91.92 mg), 1 ml of mesitylene, 40+30 ml of MeOH and 4 ml of NH_3 at 28 %. 116.00 mg were obtained, with a yield of 64 %. Compound 2 is insoluble in dimethyl sulfoxide (DMSO), alcohols, acetone, acetonitrile (CH_3CN), chlorinated solvents and water. Elemental analysis for $Ag_2[C_8H_8N_4]$: H, 2.15; C, 25.56; N, 14.90. Found: H, 2.09; C, 25.87; N, 14.98. FT-IR (cm^{-1}): 2945 (wbr) ν(C−$H_{aromatic}$), 2903 (wbr) ν(C−$H_{aromatic}$), 1629 (wbr), 1500 (m) ν(C=C + C=N), 1439 (mbr), 1422 (mbr), 1376 (w), 1343 (s), 1300 (w), 1280 (m), 1190 (w), 1113 (s), 1048 (w), 996 (m), 971 (m), 810 (s), 667 (w), 641 (m), 416 (m). TGA (heating from 30 ºC to 650 ºC, heating rate 10 ºC/min in nitrogen flux 30 ml/min): thermal stability up to 340 ºC and progressive degradation with 65 % grey-black residue.

[Ag_2(Et_4BPZ)] ***(3)***

The synthesis was followed in a similar way to the synthesis of compound 1, using 0.4 mmols of H_2Et_4BPZ (98.47 mg), 0.4 mmols of Ag_2O (91.92 mg), 1 ml of mesitylene, 40+30 ml of MeOH and 4 ml of 28 % NH_3. 103.00 mg were obtained, with a yield of 56 %. Compound 3 is insoluble in dimethyl sulfoxide (DMSO), alcohols, acetone, acetonitrile (CH_3CN), chlorinated solvents and water. Elemental analysis $Ag_2[C_{14}H_{20}N_4]$: H, 5.72; C, 41.84; N, 10.94. Found: H, 5.07; C, 42.70; N, 11.04. FT-IR (cm^{-1}): 3013 (wbr), 2965 (wbr) ν(C−$H_{aromatic}$), 1607 (w), 1481 (wbr) ν(C=C + C=N), 1463 (wbr), 1429 (wbr), 1369 (wbr), 1356 (wbr), 1309 (w), 1246 (w), 1155 (w), 1607 (w), 1054 (m), 970 (wbr), 930 (w), 870 (w), 827 (w), 782 (w). TGA (heating from 30 ºC to 650 ºC, heating rate 10 ºC/min in nitrogen flux 30 ml/min): initial loss of 2 solvent molecules (11.08 %),

stability up to approximately 340 ºC and progressive degradation with a 40 % grey-black stain residue.

[$Ag_2(Me_4BPZ)$] ***(4)***

The synthesis was followed in a similar way to the synthesis of compound 1, using 0.4 mmols H_2Me_4BPZ (76.04 mg), 0.4 mmol of Ag_2O (91.92 mg), 1 ml of mesitylene, 40+30 ml of MeOH and 4 ml of 28 % NH_3. 83.30 mg were obtained, with a corresponding yield 52 %. Compound 4 is insoluble in dimethyl sulfoxide (DMSO), alcohols, acetone, acetonitrile (CH_3CN) chlorinated solvents and water. FT-IR (cm^{-1}): 2939 (wbr) ν($C-H_{aromatic}$), 2911 (wbr), 2852 (wbr) ν($C-H_{aromatic}$), 1604 (w), 1503 (wbr) ν(C=C + C=N), 1476 (wbr), 1439 (wbr) ν(C=C + C=N), 1335 (w) 1157 (w), 1048 (s), 826 (w), 792 (w), 681 (w). TGA (heating from 30 ºC to 650 ºC, heating rate 10 ºC/min in nitrogen flow 30 ml/min): stability up to 380 ºC and progressive degradation with a 50 % grey-black residue.

[$Ag_2(Me_2BDP)$] ***(5)***

A solution of Ag_2O (0.4 mmols, 91.92 mg) in aqueous ammonia (28 %), 20 ml of MeOH and 1 ml of mesitylene is added slowly to a solution of H_2Me_2BDP (0.4 mmol, 95.00 mg) dissolved in 20 ml of MeOH with 0.8 mmols of NaOH, stirred for about 1 day. The precipitate formed is filtered and washed 6 to 8 times with 10 ml MeOH so that all mesitylene is removed. Air dry the mixture for 3-4 h. 160.90 mg were obtained, with a yield corresponding to 89%. Compound 5 is insoluble in dimethyl sulfoxide (DMSO), alcohols, acetone, acetonitrile (CH_3CN), chlorinated solvents and water. Elemental analysis for $Ag_2[C_{14}H_{12}N_4]$: H, 2.68; C, 37.20; N, 12.40. Found: H, 2.65; C, 37.44; N, 12.47. FT-IR (cm-1): 3026 (wbr), 2907 (wbr) ν($C-H_{aromatic}$), 1920 (wbr), 1650 (wbr), 1568 (s) ν(C=C + C=N), 1481 (m) ν(C=C + C=N), 1468 (w), 1435 (wbr), 1409 (wbr), 1381 (wbr), 1361 (w), 1337 (s), 1300 (w), 1246 (wbr), 1184 (w), 1110 (s), 1047 (w), 1003 (w), 973 (w), 848 (w), 819 (s), 681 (w), 650 (w), 555 (m), 640 (m), 520 (m), 477 (w), 448 (w), 412 (wbr). TGA (heating from 30 ºC to

700 ºC, heating rate 10 ºC/min in nitrogen flow 30 ml/min): stability up to approximately 370 ºC and progressive degradation with a residual of 65 % grey-black color.

Sensors preparation and experiments procedure

Materials

Plastic-type Mylar slides with two silver electrodes printed, Ag(I) CPs, polyvinyldenfluoride, 1-ethyl-3-methylimidazolium tetrafluoroborate and DMA were utilized to prepare sensors (Figure 65). Methanol, absolute ethanol, acetaldehyde and ethyl acetate were utilized to prepare aqueous solutions at the following percentages: 2% for CH_3OH, 5% for CH_3CH_2OH, 5% for CH_3CHO and 10% for $CH_3COOCH_2CH_3$. Ethylene at 200 ppm bullet and CO_2 at 5000 ppm bullet was utilized as the gas sources.

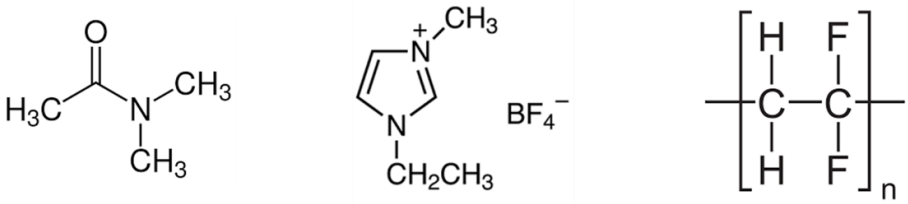

Dimethylacetamide (DMA)

1-ethyl-3-methylimidazolium tetrafluoroborate

Polyvinylidene fluoride (PVDF)

Figure 65. Materials used for the preparation of sensors

Instrumentation

A homemade plastic climate chamber (5 cm high, 7 cm wide and 14 cm long) was used to perform the experiments, where the sensors were introduced and connected to the electrometer (Keithley 2100 digital from Keithley Instrument Gmbh, Ohio, USA). The gas or vapor input and electrical connections are located on the side. Ethylene was injected in different concentration in ppm by taking variable amounts of the

corresponding gas bullet and diluting it in synthetic air, controlling the gas flows which entered a mixing chamber using a computer-controlled mass flow controller (Air Liquid Espana S.A., Madrid, Spain) operating at a total pressure of 760 Torr and a flow rate between 1 and 25 g/h. A Controlled Evaporator Mixer system (CEM) was used to produce different vapor concentrations (starting from 0 ppm to 250 ppm) from analytes water solutions (methanol 2%, ethanol 5%, Acetaldehyde 5%, Ethyl acetate 10%) and to obtain humidity condition from 0% to 100% of R.H. CEM consists of a mass flow controller for the control and measurement of the carrier gas flow (air) and a mass flow meter for liquids (MiniCorifow) with a range of 0.4–20 g/h of liquid. The liquid flow and liquid mixing with the carrier gas flow are controlled by a 3-way EMC mixing valve and an evaporator. In addition, it contains a temperature-controlled heat exchanger to heat the mixture and completely evaporate the liquid (100°C for water; 77.1°C for ethyl acetate; 78°C for ethanol; 65°C for methanol; 20,4°C for acetaldehyde).

Samples preparation

The resistive gas sensor was prepared on a clean Mylar plastic-type slide (2.5 × 2.5 cm) by screen printing on it two 10 mm × 2 mm silver electrodes with a separation of 1.5 mm. The silver coordination polymers were mortared and sieved to a grain size of 150 µm. A solution of 40.0 mg of the PVDF polymer was prepared in 1 ml of DMA and 1 mg of Ag(I) CPs powder and 1 µL of ionic liquid (1-ethyl-3-methylimidazolium tetrafluoroborate) was added. After that, 25 µL of this cocktail were cast onto the silver electrodes in a Mylar support using a spin coating technique at 80 rpm for 1 min.

Experimental procedure

The clamps are applied on one side of the sensor, in contact with the two silver electrodes, where the silver(I) coordination polymer to be tested has

not been applied. The ohmmeter which detects the electrical resistance of the sensor is connected to these terminals. The clamp-sensor system is positioned in the climatic chamber where the gas to be tested circulates, at room temperature. The first measurements are carried out in the absence of VOCs, and the air values are considered as reference; after which the gas to be detected is blown into the box at a certain flow rate and after a minute the value of the electrical resistance is recorded. Subsequently, the inlet gas flows are modified and the electrical resistance values are recorded, which vary as the concentration of gas in the environment varies. Once all the values have been obtained, the percentage response is calculated according to the following formulas (Equation 2 and 3):

$$R\% = \frac{Rg - Ra}{Ra} * 100$$

Equation 2

$$R\% = \frac{Ra - Rg}{Rg} * 100$$

Equation 3

where R% is the response % of the gas tested, Rg is the sensor resistance measured in presence of VOC at a given concentration in ppm and Ra is the resistance of sensor measured on air. Equation 2 and equation 3 were utilized respectively when Rg increases (Ethylene, Acetaldehyde, Ethyl Acetate and Humidity) and when Rg decreases (Ethanol).

Results and Discussion

Synthesis and Characterization of Ag(I) CPs

The reactions scheme of compounds 1, 2, 3, 4 and 5 are shown in Figure 66 and 67:

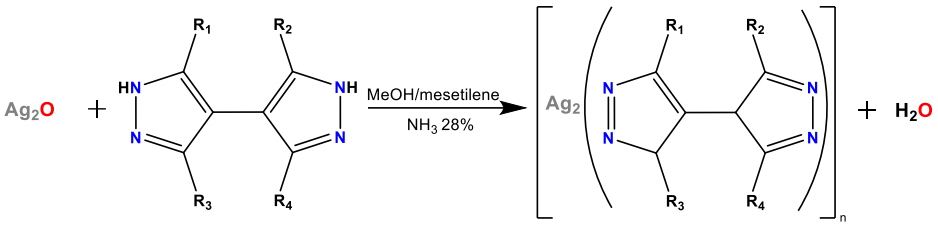

Compound 1: R1= R2= R3= R4= H
Compound 2: R1=R4= Me; R2= R3= H
Compound 3: R1= R2= R3= R4= Et
Compound 4: R1= R2= R3= R4= Me

Figure 66. Reaction scheme for compounds 1, 2, 3, 4.

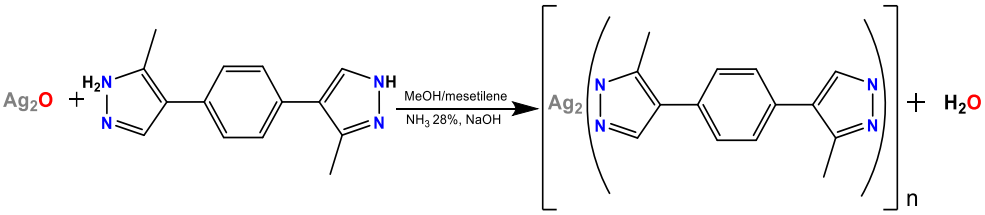

Figure 67. Reaction scheme for compound 5.

For the successful synthesis of these compounds, it is necessary to repair the reaction mixture from direct light, since silver and its compounds are photosensitive and risk degradation with exposure to light radiation. With radiation the Ag^{+} ion photoreduces to Ag^{0} showing a greyish/silvery color typical of the metal. For this reason, during the synthesis phase it is important to cover the reaction flask with aluminum paper in order to protect the silver ion from light.

Coordination has also been confirmed by comparing the FT-IR spectra of the free ligand and of the Ag(I) compounds, as shown in Figure 68a and b:

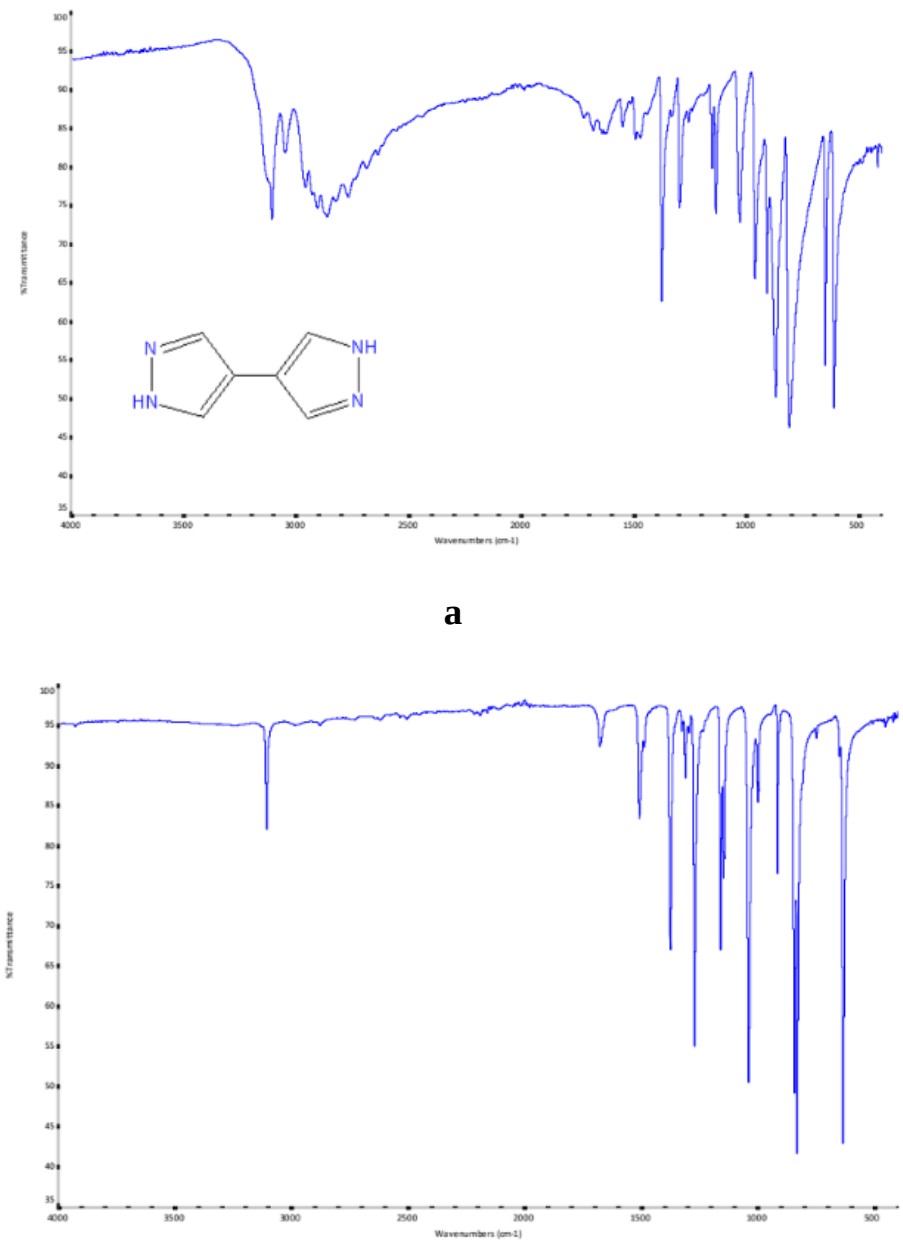

a

b

Figure 68. Comparison of IR spectra of (a) the free bipyrazole ligand and (b) the compound 1 [Ag_2(BPZ)].

The comparison between the spectra of the ligand and the compound 1 shows the coordination as the spectrum of the compound is more defined with the peaks shifted with respect to the spectrum of the corresponding binder. In the spectrum of the H_2BPZ ligand (Figure 68a) we can see the wide signal related to the stretching of the N-H bond from 3000 to 2600 cm^{-1} that in the spectrum of the corresponding compound 1 (Figure 68b) is not present since the atoms of N are deprotonated and coordinated at the

metal center. The peak at 3109 cm^{-1} is referred to the stretching of C-H bonds of aromatic systems. At 1510 cm^{-1} is distinguishable the peak of the stretching of the bonds C=C and C=N of the pyrazole ring.
From 1500 cm^{-1} to the end of the spectrum is the fingerprint, characteristic for each structure, where the peaks are due to the vibrations of the entire reticular skeleton.

Thermal Analysis

All compounds were subjected to thermogravimetric analysis coupled with differential thermal analysis (TGA/DTA) in a temperature range of 30-650ºC with a heating rate of 10ºC/min in nitrogen flow. Compounds 1-5 exhibit very similar thermal behavior, they are stable up to 340-350°C, as shown in the case of compound 5 (Figure 69). The thermogram of compound 3 (Figure 70) shows the loss of solvent before 300ºC corresponding to 2 MeOH molecules. Methanol usually has a boiling temperature of 64.7ºC, but it can be seen from Figure 70 that the loss of the solvent occurs in the range of 150-300°C, this is due to the fact that solvent molecules can be trapped during the formation of the structure of the coordination polymer by not allowing it to move away at lower temperatures.

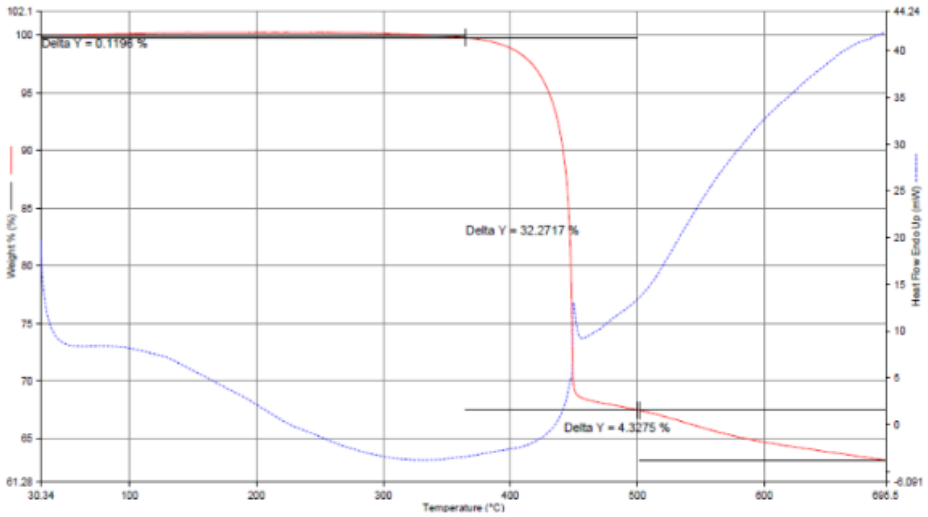

Figure 69. TGA/DTA of compound 5.

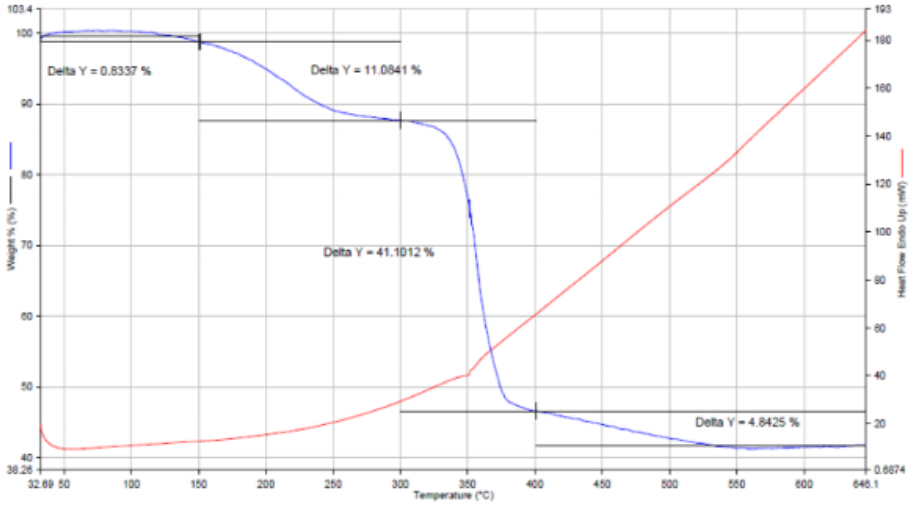

Figure 70. TGA/DTA of compound 3.

From these analyses a similar thermal behavior can be observed between the compounds. The high degradation temperature confirms the high thermal stability of the compounds obtained.

X-ray diffraction crystallography on powders

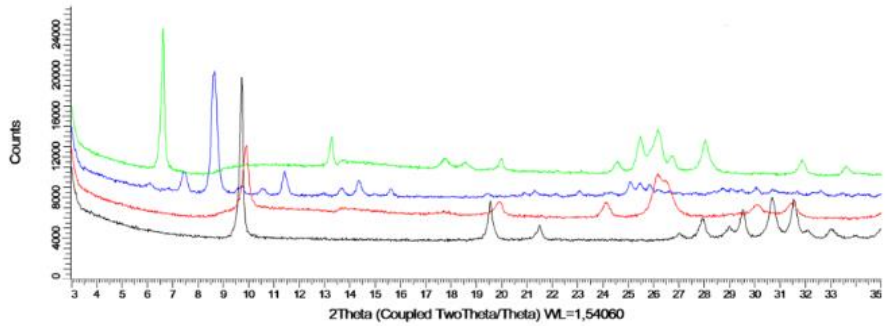

Figure 71. XRD analysis of Compound 1(black), Compound 2 (red), Compound 3 (blue), Compound 5 (green).

A first crystallographic X-ray diffraction screening on the dust of compounds 1, 2, 3 and 5 shows sharp and defined signals (Figure 71). Further studies are being carried out to determine the crystallographic structure.

Ag(I) CPs as chemoresistant sensors

The Ag(I) CPs used in this study are not soluble in any solvent. Hence, to build the sensors, a very fine suspension of Ag(I) CPs powder in a mixture of DMA and the ionic liquid 1-ethyl-3-methylimidazolium tetrafluoroborate has been prepared to favor as much as possible the homogeneity of the obtained heterogeneous mixture. The linear range of application of each sensor was: until 50 ppm for ethylene, 200 ppm for acetaldehyde at 5%, 250 ppm for ethyl acetate at 10%, 180 ppm for methanol at 2% and 240 ppm for ethanol 5%. For each tested VOC a linear increase of Response % was found for all Ag(I) CPs, except for Ag_2Et_4BPZ tested with ethanol, that shows a stability in the resistance value (Figure 76). In the presence of humidity, all Ag(I) CPs give similar response % at different relative humidity (RH) (Figure 77). Hence, humidity doesn't influence the sensitivity of sensors. When the sensor is in air, oxygen is the atmospheric component that can interact with the sensor, according to this possible mechanism (Eq. 4):[124]

$$O_{2\ (gas)} + n\ e^- \leftrightarrow O_x^{n-}{}_{(ads)} + hole^{n+}$$

Equation 4

After the adsorption of oxygen on the surface of the material, gaps are formed left by the electrons which reduce the oxygen molecule, and the material conductivity essentially depends on the mobility of the electric current through these holes. Therefore, the conductivity of the material changes according to the oxidizing or reducing nature of the gases present in the environment.

In contact with air, the sensor interacts with the oxygen molecules and the electrons that are extracted from the conduction band of the surface lead to the creation of negatively charged oxygen ions. Thus, a potential barrier is formed which limits the path of electrons and thus lowers the conductivity while increasing the electrical resistance.[126] When the gas comes into contact with the surface, the barrier decreases, lowering the electrical resistance, or rises, increasing the resistance, depending on the

nature of the gas which can be oxidizing or reducing. Thus, it is possible to determine the presence and concentration of gaseous species. Therefore, to obtain a very sensitive gas sensor, the type of interaction or reaction of the gases with the material surface must be evaluated.[125]

From Figure 72 to Figure 77 the final results of experiments to the misures of chemoresistant sensors are shown.

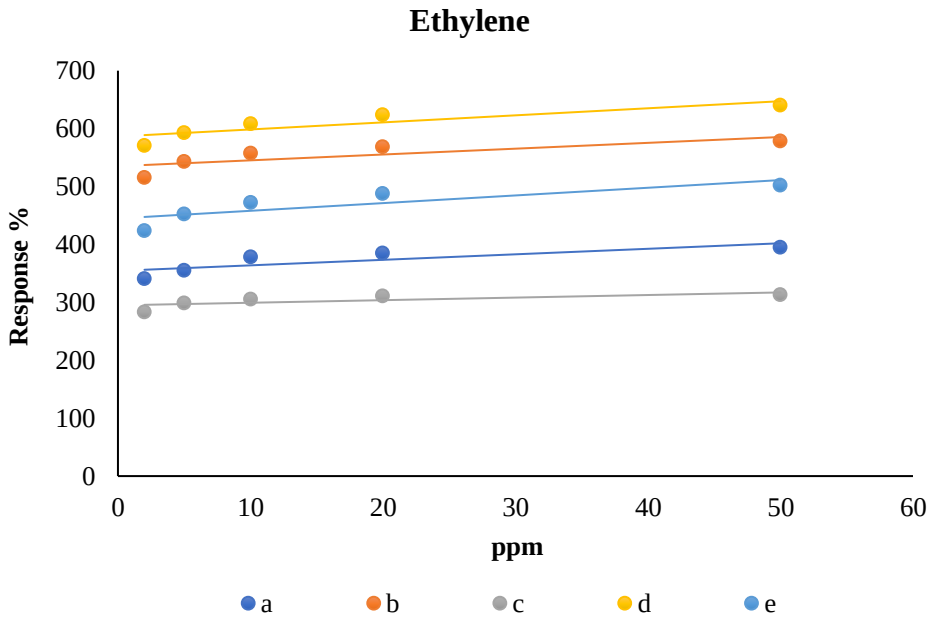

Figure 72. Response % in presence of ethylene of a) Ag_2BPZ, b) Ag_2Me_4BPZ, c) Ag_2Et_4BPZ, d) Ag_2Me_2BPZ, e) Ag_2Me_2BDZ.

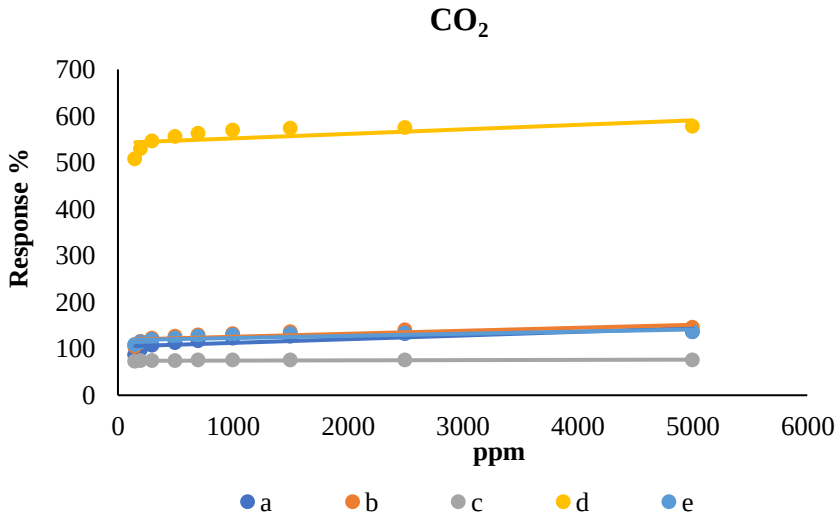

Figure 73. Response % in presence of CO_2 of a) Ag_2BPZ, b) Ag_2Me_4BPZ, c) Ag_2Et_4BPZ, d) Ag_2Me_2BPZ, e) Ag_2Me_2BDZ.

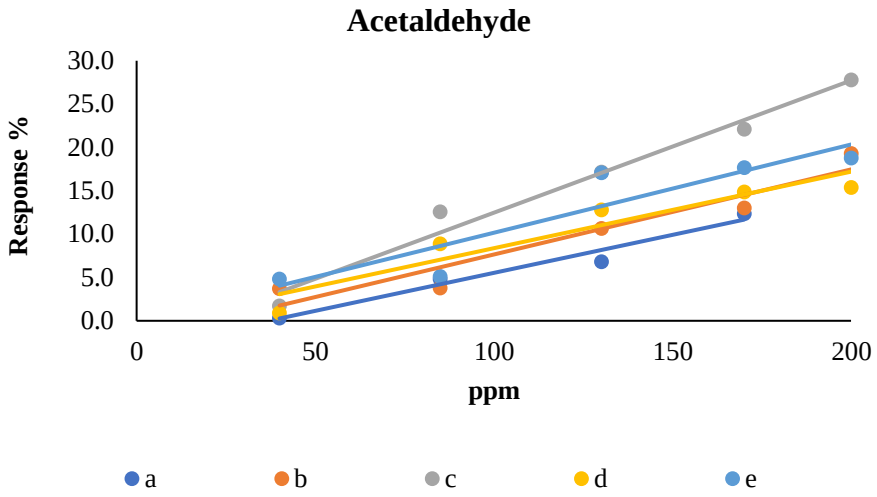

Figure 74. Response % in presence of acetaldehyde of a) Ag_2BPZ b) Ag_2Me_4BPZ c) Ag_2Et_4BPZ d) Ag_2Me_2BPZ e) Ag_2Me_2BDZ.

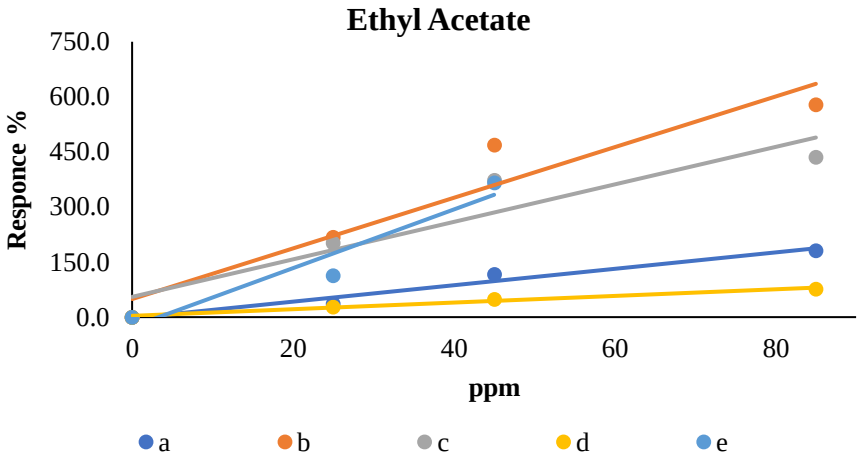

Figure 75. Response % in presence of ethyl acetate of a) Ag_2BPZ b) Ag_2Me_4BPZ c) Ag_2Et_4BPZ d) Ag_2Me_2BPZ e) Ag_2Me_2BDZ.

In the work of Zhao et al.[127] it can be seen that the resistivity of TiO_2 sample decreases exponentially after ethanol injection, and returns to its initial state after exposure on air, in agreement with the behavior of a typical n-type semiconductor. From the results obtained, it can be seen that the Ag(I) sensors have the same behavior found with TiO_2 materials in the study of Zhao. Therefore, we propose that also in our experiments we are dealing with n-type semiconductor materials in presence of alcohols. In

Figure 74 the Response % of our Ag(I) CPs in the presence of ethanol calculated with Equation 2 is shown.

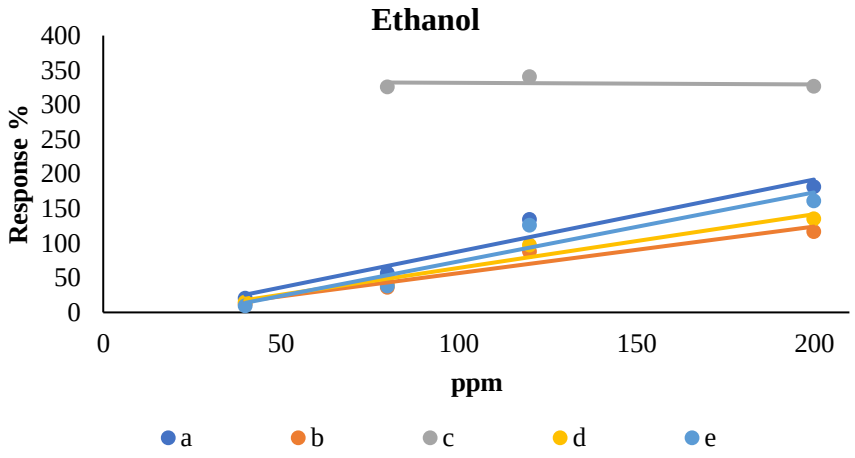

Figure 76. Response % in presence of ethanol of a) Ag_2BPZ b) Ag_2Me_4BPZ c) Ag_2Et_4BPZ d) Ag_2Me_2BPZ e) Ag_2Me_2PhBPZ.

The following are the interactions occurring on the surface of the sensors and leading to oxidation of ethanol (From Equation 5 to 8):

$$O_{2\,(gas)} \leftrightarrow O_{2\,(ads)}$$

Equation 5

$$O_{2\,(ads)} + e^- \rightarrow O_2^-{}_{(ads)}$$

Equation 6

$$CH_3CH_2OH_{\,(gas)} \leftrightarrow CH_3CH_2OH_{\,(ads)}$$

Equation 7

$$CH_3CH_2OH_{\,(ads)} + 3O_2^-{}_{(ads)} \leftrightarrow 2CO_{2\,(gas)} + 3H_2O_{\,(gas)} + 6e^-$$

Equation 8

The released electrons will decrease the potential barrier, resulting in a decrease in sensor resistance.[127]

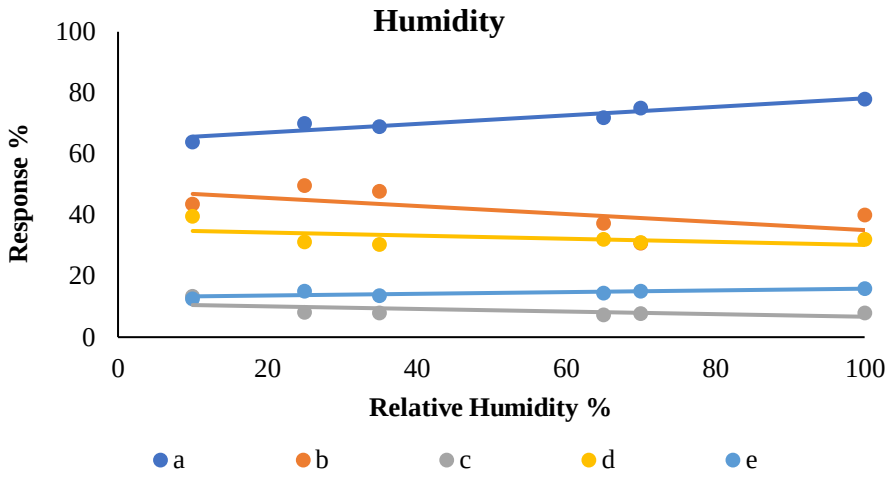

Figure 77. Response % in presence of humidity of a) Ag_2BPZ b) Ag_2Me_4BPZ c) Ag_2Et_4BPZ d) Ag_2Me_2BPZ e) Ag2Me2PhBPZ.

Ag(I) CPs electrical resistance in presence of fruit

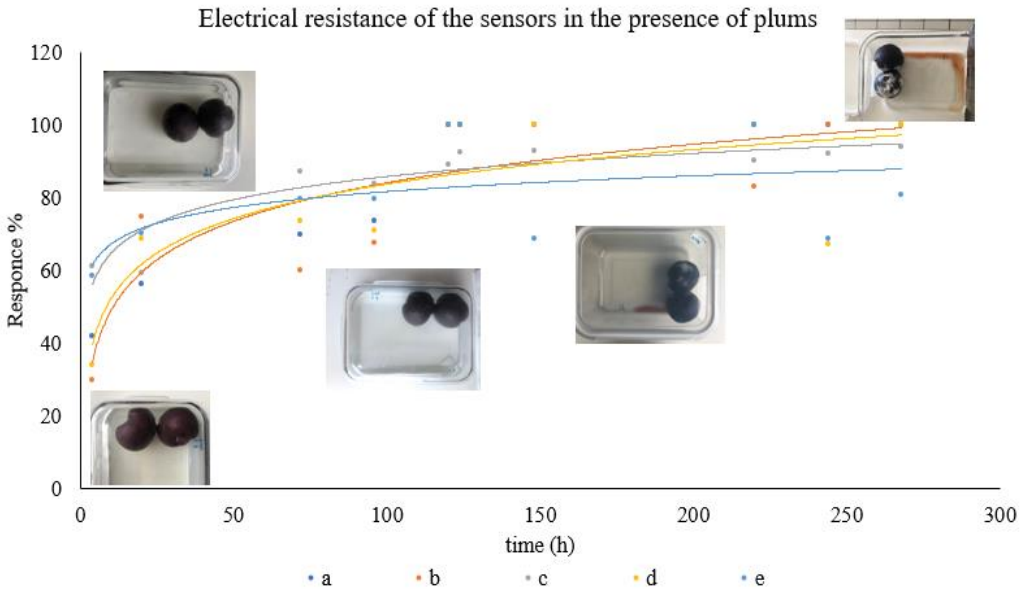

Figure 78. Representation of the variation of electrical resistance of sensors in presence of plums. a) Ag_2BPZ b) Ag_2Me_4BPZ c) Ag_2Et_4BPZ c) Ag_2Me_2BPZ d) Ag_2Me_2BDZ.

The objective was to measure the electrical resistance and then calculate the percentage response, until stability over time (Figure 78). In total, the experiment lasted 268 hours. The electrical resistance, measured with the

Ag(I) sensors inside the insulated box, decreases by increasing the level of saturation of the environment with volatile substances produced by the fruit during maturation. As time passes, it is clear from Figure 78 how the appearance of the plums also changes, which even end up breaking, spilling juice and producing mold, indicating an advanced state of ripeness.

Conclusion

Tests carried out on the electrical conductivity of the sensors obtained by Ag(I) CPs show that the use of these particular coordination polymers is promising to identify the presence of VOCs produced by the fermentation of fruit. The test carried out in the presence of plums shows how the electrical resistance of these chemoresistant sensors stabilizes gradually going towards the saturation of the environment of gases produced by ripening plums. Further studies of chemoresistivity and characterization of silver coordination complexes are being carried out in collaboration with the inorganic chemistry group and the analytical chemistry group of the University of Granada.

References

(111) Frontmatter. In *Design and Construction of Coordination Polymers*; Hong, M., Chen, L., Eds.; Wiley, 2009. DOI: 10.1002/9780470467336.fmatter.

(112) Dong, Y.-B.; Zhao, X.; Huang, R.-Q.; Smith, M. D.; Zur Loye, H.-C. New Ag(I)-Containing Coordination Polymers Generated from Multidentate Schiff-Base Ligands. *Inorg. Chem.* **2004**, *43* (18), 5603–5612. DOI: 10.1021/ic049787a.

(113) Nomiya, K.; Yokoyama, H. Syntheses, Crystal Structures and Antimicrobial Activities of Polymeric Silver(i) Complexes with Three Amino-Acids [Aspartic Acid (H2asp), Glycine (Hgly) and Asparagine (Hasn)]Note: For Ease of Reference during Discussion of Their Anions, H2asp, Hgly and Hasn Have Been Used as the

Abbreviations for the Neutral Amino-Acids, Rather than the Conventional Asp, Gly and Asn, Respectively. *J. Chem. Soc., Dalton Trans.* **2002**, No. 12, 2483–2490. DOI: 10.1039/b200684g.

(114) Seward, C.; Jia, W.-L.; Wang, R.-Y.; Enright, G. D.; Wang, S. Luminescent 2D Macrocyclic Networks Based on Starburst Molecules:[{Ag(CF3SO3)}1.5(Tdapb)] and[{Ag(NO3)}3(Tdapb)]. *Angew. Chem. Int. Ed.* **2004**, *43* (22), 2933–2936. DOI: 10.1002/anie.200353126.

(115) Tăbăcaru, A.; Pettinari, C.; Marchetti, F.; Di Nicola, C.; Domasevitch, K. V.; Galli, S.; Masciocchi, N.; Scuri, S.; Grappasonni, I.; Cocchioni, M. Antibacterial Action of 4,4′-Bipyrazolyl-Based Silver(I) Coordination Polymers Embedded in PE Disks. *Inorg. Chem.* **2012**, *51* (18), 9775–9788. DOI: 10.1021/ic3011635.

(116) Zhang, J.-P.; Horike, S.; Kitagawa, S. A Flexible Porous Coordination Polymer Functionalized by Unsaturated Metal Clusters. *Angew. Chem. Int. Ed.* **2007**, *46* (6), 889–892. DOI: 10.1002/anie.200603270.

(117) Fu, R.; Xia, S.; Xiang, S.; Hu, S.; Wu, X. Syntheses, Characterization and Electrical Property of a New Silver Diphosphonate with Zeolite-like Framework and Three-Dimensional Silver Interactions: [$Ag_4(O_3PCH_2CH_2PO_3)$]. *Journal of Solid State Chemistry* **2004**, *177* (12), 4626–4631. DOI: 10.1016/j.jssc.2004.10.008

(118) Su, W.; Hong, M.; Weng, J.; Liang, Y.; Zhao, Y.; Cao, R.; Zhou, Z.; Chan, A. S. C. Tunable Polymerization of Silver Complexes with Organosulfur Ligand: Counterions Effect, Solvent- and Temperature-Dependence in the Formation of Silver(I)-Thiolate(and/or Thione) Complexes. *Inorganica Chimica Acta* **2002**, *331* (1), 8–15. DOI: 10.1016/S0020-1693(01)00745-9.

(119) Lin, P.; Henderson, R. A.; Harrington, R. W.; Clegg, W.; Wu, C.-D.; Wu, X.-T. New 1- and 2-Dimensional Polymeric Structures of Cyanopyridine Complexes of Ag^{I} and Cu^{I}. *Inorg. Chem.* **2004**, *43* (1), 181–188. DOI: 10.1021/ic030254w.

(120) Rao, C. N. R.; Ranganathan, A.; Pedireddi, V. R.; Raju, A. R. A Novel Hybrid Layer Compound Containing Silver Sheets and an Organic Spacer. *Chemical Communications* **2000**, No. 1, 39–40. DOI: 10.1039/A908171B

(121) Liu, S. Q.; Kuroda-Sowa, T.; Konaka, H.; Suenaga, Y.; Maekawa, M.; Mizutani, T.; Ning, G. L.; Munakata, M. Silver(I) Coordination Polymers of Fluorescent Oligo(Phenylenevinylene) with Π−π Stackings: Luminescence and Conductivity. *Inorg. Chem.* **2005**, *44* (4), 1031–1036. DOI: 10.1021/ic0400585.

(122) Munakata, M.; Ning, G. L.; Suenaga, Y.; Kuroda-Sowa, T.; Maekawa, M.; Ohta, T. A One-Dimensional Metallocyclophane with Columnar Aromatic Stacking: The Silver (i) η2-Coordination Complex of 1, 2-Benztriphenylene. *Angewandte Chemie* **2000**, *112* (24),4729–4731. DOI: 10.1002/1521-3773 (20001215) 39:24<4555: :AID-ANIE4555>3.0.CO;2-T

(123) Cheng, W.; Tang, X.; Zhang, Y.; Wu, D.; Yang, W. Applications of Metal-Organic Framework (MOF)-Based Sensors for Food Safety: Enhancing Mechanisms and Recent Advances. *Trends in Food Science & Technology* **2021**, *112*, 268–282. DOI: 10.1016/j.tifs.2021.04.004.

(124) Fernández-Ramos, M. D.; Capitán-Vallvey, L. F.; Pastrana-Martínez, L. M.; Morales-Torres, S.; Maldonado-Hódar, F. J. Chemoresistive NH3 Gas Sensor at Room Temperature Based on the Carbon Gel-TiO2 Nanocomposites. *Sensors and Actuators B: Chemical* **2022**, *368*, 132103. DOI: 10.1016/j.snb.2022.132103.

(125) Naz, S.; Javid, I.; Konwar, S.; Singh, P. K.; Sahni, M.; Bhattacharya, B. Solid State Gas Sensor. *Materials Today: Proceedings* **2022**, *49*, 3245–3249. DOI: 10.1016/j.matpr.2020.11.1031.

(126) Williams, D. E. Semiconducting Oxides as Gas-Sensitive Resistors. *Sensors and Actuators B: Chemical* **1999**, *57* (1–3), 1–16. DOI: 10.1016/S0925-4005(99)00133-1.

(127) Zhao, P. X.; Tang, Y.; Mao, J.; Chen, Y. X.; Song, H.; Wang, J. W.; Song, Y.; Liang, Y. Q.; Zhang, X. M. One-Dimensional MoS2-Decorated TiO2 Nanotube Gas Sensors for Efficient Alcohol

Sensing. *Journal of Alloys and Compounds* **2016**, *674*, 252–258. DOI: 10.1016/j.jallcom.2016.03.029.

(128) Tung, T. T.; Tran, M. T.; Feller, J.-F.; Castro, M.; Van Ngo, T.; Hassan, K.; Nine, M. J.; Losic, D. Graphene and Metal Organic Frameworks (MOFs) Hybridization for Tunable Chemoresistive Sensors for Detection of Volatile Organic Compounds (VOCs) Biomarkers. *Carbon* **2020**, *159*, 333–344. DOI: 10.1016/j.carbon.2019.12.010.

(129) Zhang, J.-P.; Kitagawa, S. Supramolecular Isomerism, Framework Flexibility, Unsaturated Metal Center, and Porous Property of Ag(I)/Cu(I) 3,3‘,5,5‘-Tetrametyl-4,4‘-Bipyrazolate. *J. Am. Chem. Soc.* **2008**, *130* (3), 907–917. DOI: 10.1021/ja075408b.